ELECTRON-BEAM GUN SYSTEM

FOR

ELECTRON-CAPTURE

RATE-COEFFICIENT MEASUREMENT

By

© MARC OLIVIER, B.Sc.

A Thesis

Submitted to the School of Graduate Studies

in Partial Fulfilment of the Requirements

for the Degree

Master of Sciences

McMaster University

(September) 1980

ELECTRON-CAPTURE

RATE COEFFICIENT MEASUREMENT

MASTER OF SCIENCE (1980) McMASTER UNIVERSITY
(Physics) Hamilton, Ontario

TITLE: Electron-Beam Gun System for Electron-Capture Rate-Coefficient Measurement

AUTHOR: Marc Olivier, B.Sc. (Montreal University)

SUPERVISOR: Dr. E.A. Ballik

NUMBER OF PAGES: xii, 123

ABSTRACT

A simple, pulsed, relativistic electron-beam gun has been built to measure electron attachment rates. The high voltage pulse (~100KV) is provided by a spiral generator initially charged to ~10KV. The electron-beam is formed by a lead (Pb) cathode vacuum-diode. The resulting electron-beam pulse has an energy of ~90KeV per electron, a peak current density at the anode center of ~175 A/cm^2, and a duration of ~12 ns (FWHM).

The electron-beam is injected through a 26-μm thick aluminum foil into a gas mixture located in an electric field. By placing suitable screens in front of the beam, the injected electron-beam current-density is reduced to ~1-2 A/cm^2. This results in an electron density in the plasma (produced by the primary electrons injected in an atmospheric-pressure gas mixture) which is typically ~$10^{13} cm^{-3}$. The electric field applied across the plasma is maintained constant (within ~0.2%) by means of a storage capacitor (~1μF). Rate coefficients of electron-capture reactions are determined by observing the temporal evolution of the induced discharge current pulse.

The system was used to measure the electron dissociative-attachment rate coefficient for HCl as a function of the reduced field E/N, in both Ar-HCl and Ar-N_2-HCl mixtures. These coefficients are $6.45 \pm 0.95 \times 10^{-11}$ $cm^3 s^{-1}$ in Ar-HCl

(99:1) and 2.59±.25 x 10^{-10} $cm^3 s^{-1}$ in Ar-N_2-HCl (35:64:1), for E/N ~ 10^{-20} $V \cdot m^2$. From these measurements, and from the use of a numerical solution of the Boltzmann equation for electrons, we have calibrated the relative electron dissociative-attachment cross-section measured by Abouaf and Teillet-Billy. The peak values that give the best fit to our data are ~9.4 x 10^{-19} cm^2 for Ar-HCl and 18.0 x 10^{-19} cm^2 for Ar-N_2-HCl.

ACKNOWLEDGEMENTS

I wish to express my appreciation to my thesis supervisor, Dr. E.A. Ballik, for his guidance and support in this work. The financial support from McMaster University is also acknowledged.

I am grateful for the excellent work done by my fiancée, Liette Baervoets, in reproducing the original figures, and by Miss Lucy Felicissimo in typing this manuscript.

GLOSSARY

CONSTANTS	SYMBOLS
Bohr radius	$a_o = 0.529177 \times 10^{-10}$ m
Boltzmann's constant	$k_B = 1.3807 \times 10^{-23}$ J·K^{-1}
electron charge	$e = 1.60219 \times 10^{-19}$ coulomb
electron-volt	$eV = 1.60219 \times 10^{-19}$ J
Vacuum permeability	$\mu_o = 4\pi \times 10^{-7}$ (A·s)$^{-2}$ · kg · m
Vacuum permittivity	$\varepsilon_o = 8.8542 \times 10^{-12}$ (A·s^2)^2/kg·m^3
Velocity of light in vacuum	$c = 2.997925 \times 10^{8}$ m · s^{-1}

UNITS	SYMBOLS
Ampere	A
Farad	F
Henry	H
Joule	J
Kelvin	^{o}K
Meter	m
ohm	Ω
Pascal	Pa
Second	s
Volt	V

MULTIPLICATION FACTOR	SYMBOL
Giga - 10^9	G
Mega - 10^6	M
Kilo - 10^3	K
Milli - 10^{-3}	m

MULTIPLICATION FACTOR (continued)	SYMBOLS
Micro - 10^{-6}	μ
Nano - 10^{-9}	n
pico - 10^{-12}	p

TERM	ABBREVIATION
Capacitor	C
Electron-Beam	e - Beam
Full Width at Half Maximum	FWHM
Inductor	L
Resistor	R
Silicon Controlled Rectifier	SCR

TABLE OF CONTENTS

LIST OF FIGURES

CHAPTER 1

INTRODUCTION

In recent years, high-current, pulsed, relativistic electron-beams have become commonly employed in many areas of applied physics; these include, radiation damage studies, laser excitation, and fusion initiation studies.

The present work was oriented toward the construction, characterization, and application of a small, pulsed, relativistic electron-beam gun suitable for investigating the reaction kinetics of ionized gases.

Briefly, the electron-beam is created by a cold-cathode vacuum-diode. It is then injected through a metal foil into a gas mixture, located between a pair of electrodes connected to a capacitor bank, which applies an electric field in the gas. The fast electrons ionize the gas, forming a glow discharge. Information about the reaction kinetics under investigation is obtained by observing the temporal evolution of the discharge current pulse.

The present set up has been applied to the measurement of the rate-coefficient of the reaction dissociative attachment of electron to HCl.

1.1 Outline of the contents of the thesis

A large portion of the research effort has been spent in the construction and characterization of the experimental setup described in Chapter 2. The first part of that chapter is devoted to the electron-beam forming system. There, the principle of operation is given, the characteristics of the electron-beam current pulse are reported, and comments are made concerning the technical problems encountered with the system. The second part of the chapter describes in detail the characteristics of both the discharge chamber and the discharge circuit.

Chapter 3 deals with modeling the discharge current pulse. There, the electron-beam secondary-electron production rate is calculated. In addition, a program written to calculate the secondary-electron steady-state energy-distribution is described, and the limits of applicability are discussed. A simple model is presented for predicting the temporal evolution of the discharge current pulse for the case of an attachment-dominated plasma. Finally, suggestions are made concerning proposed modifications to the present system which should provide substantial improvements in, and increased application of the electron-beam gun system.

In the fourth chapter a review is presented of the work done on dissociative-attachment of electrons to HCl. The compromises made between different experimental parameters

are discussed. Finally, the experimentally-determined rate-coefficients for dissociative-attachment of electrons to HCl are presented and discussed.

Chapter 5 summarizes the overall research.

CHAPTER 2

EXPERIMENTAL SET UP

A simple, pulsed, electron-beam gun system has been built based on the original work of Brau et al [1]. The aim of the first part of this chapter is to add to their work by giving additional explanations of the working principles of the system, to describe our improvement to the system, and to report the measured characteristics of the present device.

Briefly, the electron-beam gun consists of a pulsed high-voltage power supply (≈100 KV) and a vacuum diode to produce the electron beam.

2.1.1 High Voltage Generator

The spiral generator used in the present device, schematically shown in Fig. 2-1, is similar to the one used by Brau et al [1]. The basic operating principle has been described by Howell and Fitch [2]. A spiral generator is made by winding a stripline (a pair of broad conductors separated with a dielectric) into a coil, with insulation between turns. The inner insulation between turns is made identical to that of the dielectric in the original stripline, to produce twin spiral lines with common conductors. When the spark gap conducts, a wave is initiated only in the

Fig. 2-1 Schematic diagram showing the spiral generator primary spark gap and triggering circuit. The components are R_1 = 10 kΩ, R_2 = 1.5 MΩ, R_3 = 4.5 KΩ, R_4 = 100Ω, R_5 = 100 M , R_6 = 5.2 MΩ, C_1 = 4 μF, C_2 = 10 nF, C_3 = 2 nF, and an SCR Model 2N3528.

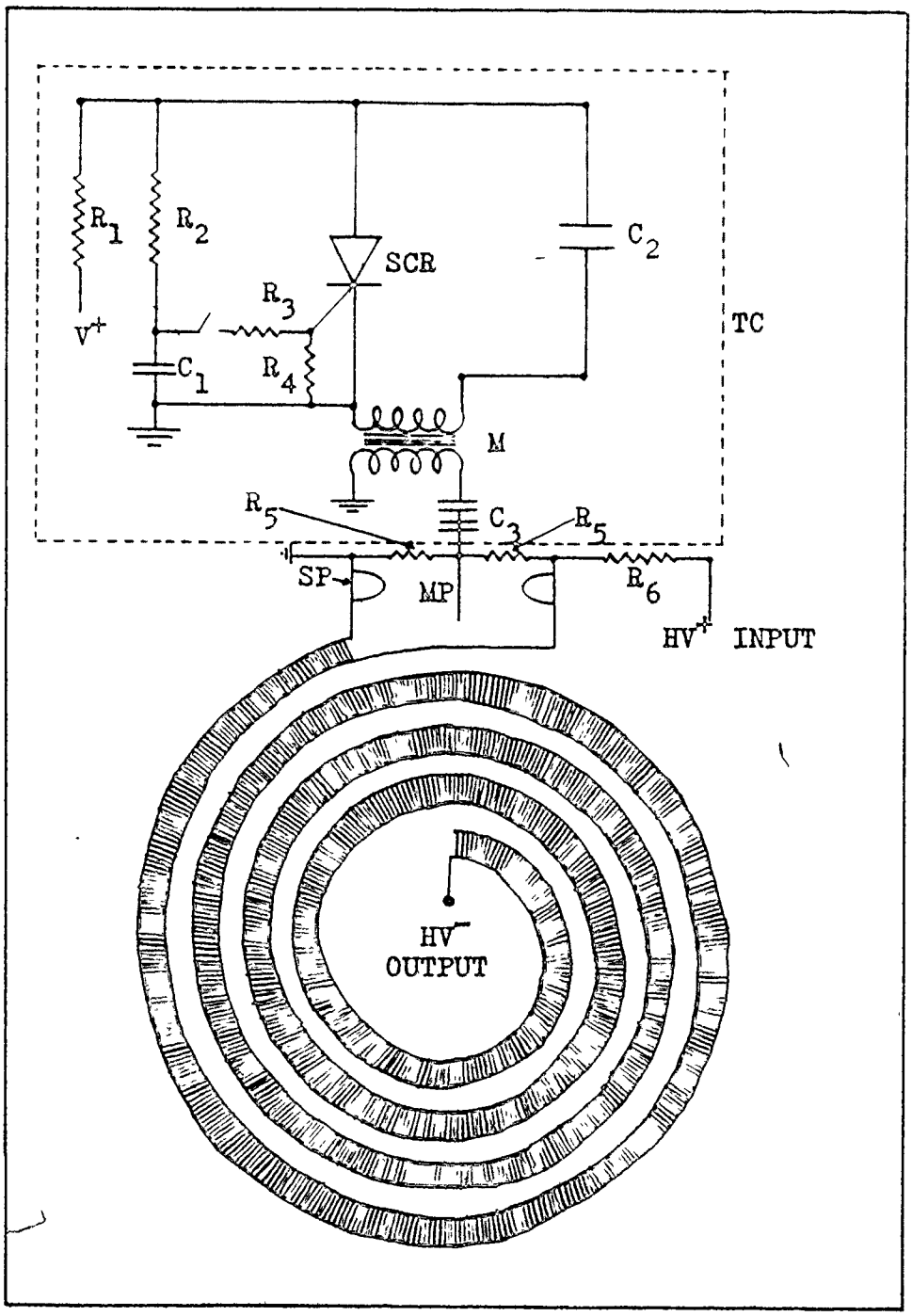
R1
R2
SCR
C2
R3
V+
TC
C1
R4
M
R5
C3
R5
SP
MP
R6
HV+ INPUT
HV-
OUTPUT

active line (shade in Fig. 2-1), leaving the electric field vectors in the passive line unopposed. The wave travels both directions in the line, then reflects off the open circuit at the inner end (HV output) and at the shorted end (spark gap), which results in a reversal of the line polarity relative to its initial charge. The generator is fully erected after a time

$$\tau = 2\pi nD/v \quad , \qquad (2.1\text{-}1)$$

where D is the average diameter of the generator, $v = (\varepsilon\mu)^{-\frac{1}{2}}$ is the velocity of light in the dielectric, and n is the number of double layers in the spiral. The voltage across each double layers is ideally $-2V_o$ (V_o is the initial charging voltage). Consequently, the voltage drop between the inner and outer conductors is

$$V = 2nV_o \quad . \qquad (2.1\text{-}2)$$

The wave then starts to de-erect the generator, which returns to its initial state after an elapsed time 2τ. The actual performance of the spiral generator is limited by several loss mechanisms [2], and falls short of the ideal model described above. Brau et al [1] explain in detail the reasons for the trade-off made between the various physical parameters n, D, t, w (t and w are the thickness and ~~width~~ of the conductor, respectively) in order to get the best performance for a given output voltage and capacitance. Following their

approach, a 25-turn spiral generator was made from a sandwich of 1 cm wide by 130 μm thick aluminum pressure sensitive tape, insulated by 2 layers of 7.5 cm wide PVC tape, each of thickness ≈ 180 μm. This coil was wound on a 14-cm diameter plexiglass tube, as shown in Fig. 2-2.

The capacitance of the generator, measured at the spark gap, is C_{in} = 73.± 5 nF. The output capacitance (at the diode) is

$$C_{out} = \frac{1}{(2n)^2} C_{in} \approx 29 \text{ pF} \quad . \qquad (2.1\text{-}3)$$

This gives a dielectric constant for PVC of ≈ 4.5 ε_o (Brau et al measured 3.8 ε_o [1]), which represents an upper bound. The value of ε may be a little lower because the tape was stretched during installation, and the line capacitance is slightly greater than calculated because of edge effects. The stripline impedance is

$$Z_o = u^{\frac{1}{2}} t/(\varepsilon w)^{\frac{1}{2}} \approx 2.6\Omega \quad . \qquad (2.1\text{-}4)$$

In order to minimize the losses due to the primary switch (spark gap) inductance (L_s), the switch rise-time must be kept small in comparison to the generator rise-time. This requirement can be written as:

$$L_s/Z_o\tau \ll 1 \quad . \qquad (2.1\text{-}5)$$

In the present case (switch inductance <50 nH) the loss is

Fig. 2.2 Cross sectional view of the electron beam gun system showing the spiral generator (SG), vacuum diode (VD), primary spark gap (PSG), series spark gap (SSG), foil electron beam window (EW), Rogowski coil (RL), and rf electromagnetic field shield (RFS).

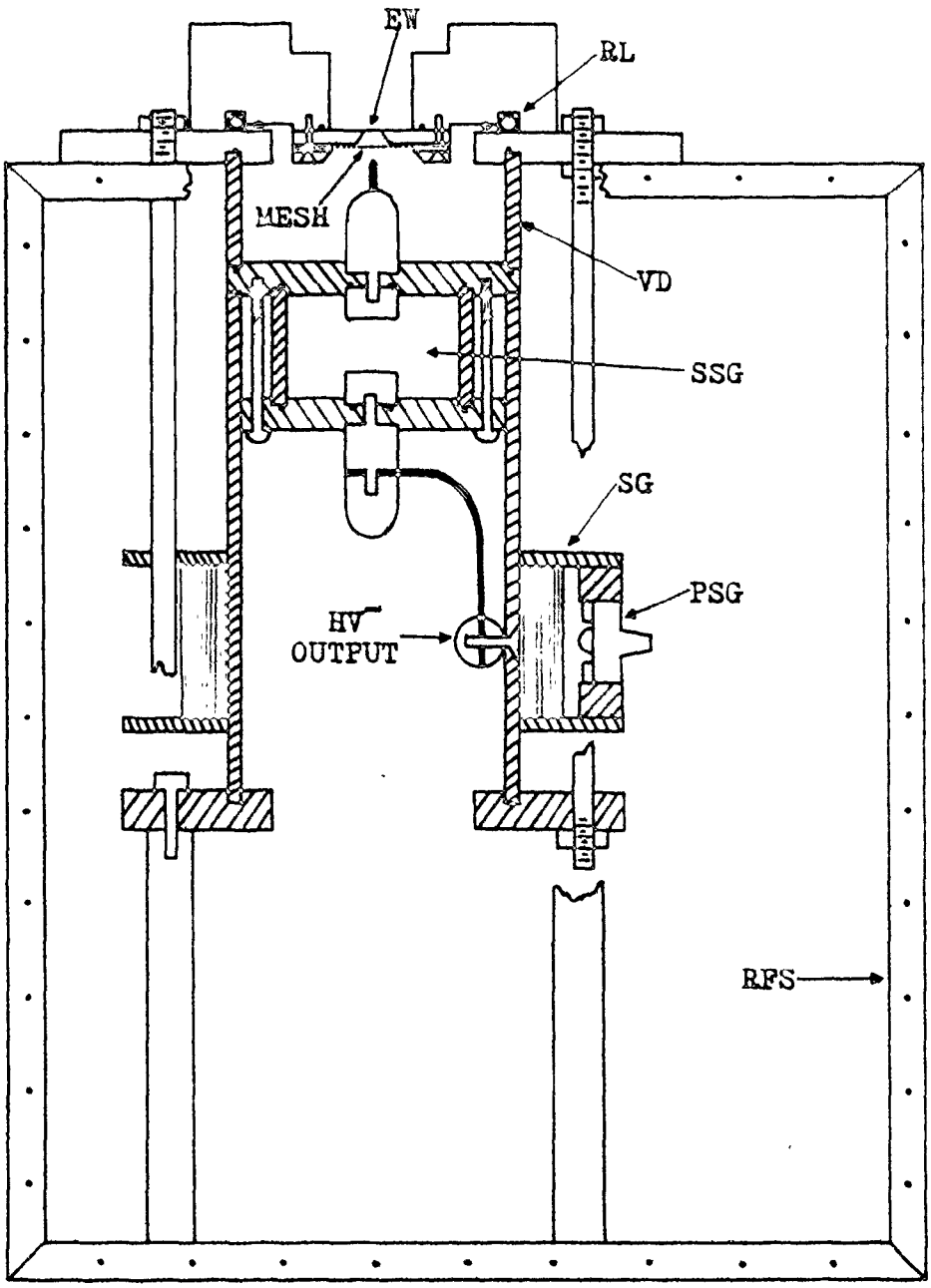
EW
RL
MESH
VD
SSG
SG
PSG
HV
OUTPUT
RFS

expected to be less than 10% [2]. The spark gap and triggering circuit used to achieve <50 nH inductance are shown schematically in Fig. 2-1. The electrodes were made from a 1-cm diameter copper rod, and the mid-plane electrode was brass. The inter electrode separation was approximately 0.5 cm, corresponding to a breakdown voltage of about 12 KV in air. Spark gap triggering was by means of a 10-15 KV positive pulse produced by a car ignition coil, coupled through a 1 nF capacitor.

A typical voltage pulse measured by means of a 1 pF capacitive voltage divider is shown in Fig. 2-3a. This pulse, which has a rise time τ = 120 ns (65% of the calculated value of 185 ns), was obtained by positively charging the generator (the high voltage was connected as shown in Fig. 2-1) (configuration I). The first peak is, as expected, negative relative to ground. The second peak, which is due to coupling between turns, is positive and approximately 50% higher than the first. The polarity of the output pulse can be reversed by interchanging the high voltage (together with R_6) and ground at the spark gap (configuration II).

Figure 2-3b shows the peak value of the measured output voltage pulses for the first and second peak, at voltages well below normal operating voltages. Our high voltage probe was limited to 40 KV peak. Therefore, the maximum input voltage could not exceed ~3.5 KV. Reliable switching was achieved when the spark gap was adjusted to hold-off ~ 4-5 KV.

Fig. 2-3 a) Typical output pulse from the 25-turn spiral generator described in the text into a 1-pF load. The generator was initially charged to 3 KV, and the primary spark gap adjusted to hold off 4-5 KV (in air). b) Peak output voltage from the 25-turn spiral generator into a 1-pF load, as a function of the charging voltage. The lower curve corresponds to the first voltage peak (Fig. 2-3a) and the upper curve corresponds to the second voltage peak.

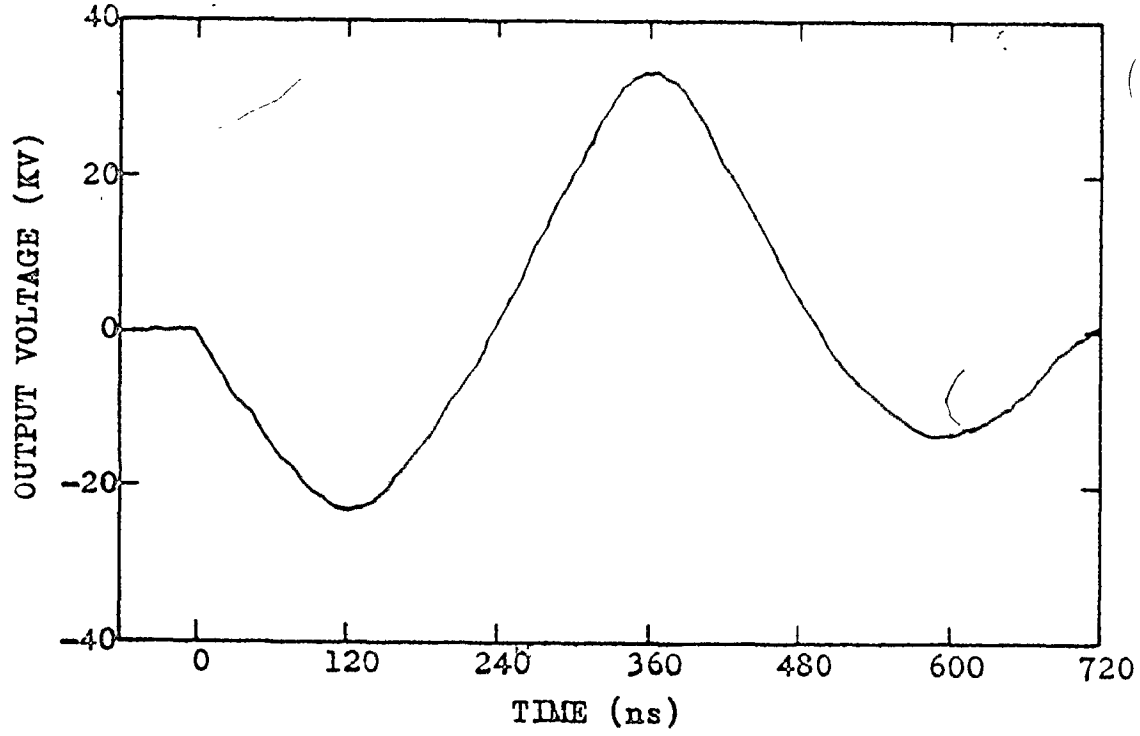
40
20
0
-20
-40
OUTPUT VOLTAGE (KV)
0
120
240
360
480
600
720
TIME (ns)

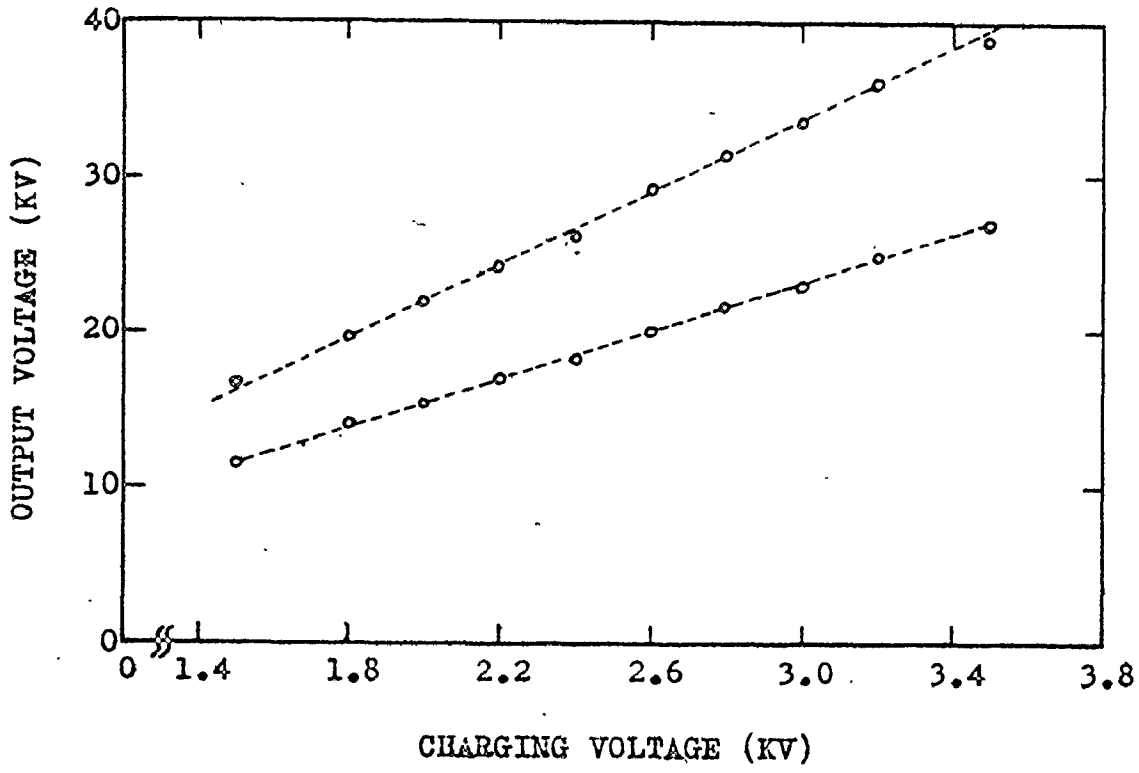
40
30
20
10
0
OUTPUT VOLTAGE (KV)
0
1.4
1.8
2.2
2.6
3.0
3.4
3.8
CHARGING VOLTAGE (KV)

The small spacing at this hold-off voltage results in a lower than normal switch inductance, and correspondingly lower losses. There is a resulting voltage "increase" which should, however, be somewhat equalized by loading of the probe capacitance. This loading reduced the voltage by ≈ 3%. The results of Brau et al [1] indicate a breakdown of linearity at high charging voltage. For example, at 12 KV the output voltage can be as much as 30% less than estimated by direct extrapolation.

In most of our experiments, we connected the inner conductor of the spiral to the ground plate (opposite polarity to that shown in Fig. 2-1). The electron gun was therefore operated on the second (negative) peak of the voltage pulse. This permitted us to obtain a suitably high output voltage of ~ 100 KV by charging the line at about 10 KV, which was well below insulation breakdown (estimated to occur at ~ 15 KV).

During the pulse, discharges could start on the inner conducting layer, propagate along the surface of the tube,an and finally jump to the grounded support rods. That problem was solved by covering the surface of the dielectric tape with silicon vacuum grease.

2.1.2 Vacuum diode

The electron beam in the present device is produced

by a cold-cathode vacuum diode. A brief summary of the large amount of work done on the latter is given below. However it may be noted that the behavior of cold cathodes is not yet fully understood.

When the gas pressure in a discharge is reduced to such a low value that the mean free path of the electrons and positive ions is large in comparison to the discharge gap, the mechanism of breakdown depends solely on electrode processes. Fowler and Nordeim [3] have shown that when a very large positive electric field ($\simeq$ GV·m^{-1}) is applied on a metal surface, the electrons have an appreciable probability of tunneling through the solid potential barrier. This phenomenon is called field emission. At a given value of the electrical field the experimentally observed current density is ually higher than predicted by the Fowler-Nordeim theory. The apparent discrepancy has been resolved by extended studies, which show that the initial electron flow must be field emitted from the tip of microscopic whisker-like projections (typically 1 μm height, 0.1 μm base) appearing at the surface of the cathode, over which the field is locally enhanced by factor as large as two orders of magnitude [4]. In the second phase (leading to breakdown), Fursci et al [5] have shown that the microscopic field at the tip must exceed some critical value in order for the cathode field emission to evolve beyond the stable mode. Under that condition the current density gets large enough for the tip temperature to

increase above the point where the cathode material is evaporated. This evaporation, in regions close to the whiskers, increases the probability of gas ionization. The resultant ions contribute to reduce the electron space charge, which maintains a large voltage gradient in the vicinity of the cathode [6]. There is then a rapid increase in the emitted current, with subsequent resistive heating of the whiskers. The projection finally explodes, causing the onset of cathode flares [7].

Bugaev et al [7] have shown that following the explosion of the projections, the cathode flare current increases at a flow rate determined by space charge limited emission from the surface of the plasma. At the same time, the plasma sheath radially expands at a velocity of 2-3 cm/μs. Parker et al [6] have derived an expression giving the correct dependance for the time interval t_i required for a projection to reach the critical temperature point T_c (where the vapor pressure of the material is $\approx 10^{-2}$ Pa). The relationship is

$$t_i \propto \frac{\rho d}{\eta} T_c F^{-3} \qquad (2.1\text{-}6)$$

where ρ is the density of the tip material, d its specific heat, η its resistivity at T_c, and F the microscopic electric field. Bugaev et al [7] have also measured the breakdown delay time t_d (the elapsed time between the application of a

voltage gradient and the time when the resultant current achieves ~ its space charge limited value) as a function of the macroscopic field strength E_m. Parker et al [6] have shown experimentally that both t_i and t_d have the same F^{-3} dependence. Furthermore, they have pointed out that before the results of Bugaev et al [7] can be used, it is necessary to know the ratio of the field enhancement factor observed in their experiment (Bugaev et al) to the field enhancement factor pertinent to the configuration under investigation.

In order for a cold cathode to transform efficiently the electromagnetic pulse energy into electron kinetic energy, the build-up time of the cathode plasma (qualitatively defined as the time required for the plasma to form a uniform emission surface) must be kept as small as possible. The electric field dependence of the build-up time is similar to that for whisker breakdown time t_i. In addition it depends on the concentration of thermally unstable cathode projections.

Another factor is the effect of the anode composition on the electrical properties of the electron beam diodes. Kelly et al [8] have observed that low molecular weight impurities in the anode may cross the gap at velocities of ~ 10 cm/μs. The most likely impurity candidate is the hydrogen molecule because of its small mass. The presence of impurities may lead to an early closure of the diode, which limits the maximum duration of the electron beam current pulse.

The vacuum-diode chamber shown in Fig. 2-2, is made of plexiglass and aluminum. It has a total volume of ~ 0.56 ℓ, a total surface area of ≈ 430 cm^2 and a plexiglass surface area of ≈ 304 cm^2. After extensive pumping (> 48 h) the "leak rate" of the chamber was found to be approximately 1.2 Pa/min. After careful examination of the chamber by means of an He mass spectrometer leak detector, the relatively large "leak rate" was attributed to the poor outgassing property of plexiglass. This is further supported from comparison of the measured rate with the value of leak rate > 0.6 Pa/min calculated using Eq. (2.2-1) and a pumping time of 48 h. The discrepancy is not serious since Eq. (2.2-1) is derived for the best available experimental condition for plexiglass, as reported by Dayton [9].

Two pumping system configurations were used in the present case. The first configuration is obtained by replacing the diffusion/mechanical pump arrangement, shown in Fig. 2-4, with a mechanical pump connected in series with a liquid-nitrogen cold trap. This is connected to the vacuum chamber by means of a low conductivity (~ 0.0022ℓ/s) system of tubing and valves. The ultimate vacuum attainable was estimated at ~ 5.6 Pa and measured at ~ 4-5.5 Pa.

The diode operation was found to be erratic with the above pumping configuration. We first believed that the problem was caused by vacuum flashoever (see, e.g., Okhi et al [10], or Bergeron [11]) because a gas discharge could

Fig. 2-4 Schematic diagram of the vacuum system. A diffusion pump (DP) connected to a mechanical pump (MP) was used to evacuate the vacuum diode (VD); A mechanical pump connected in series with a liquid nitrogen cold trap (LNCT) was used to pump the experimental cell (EC) and the series spark gap.

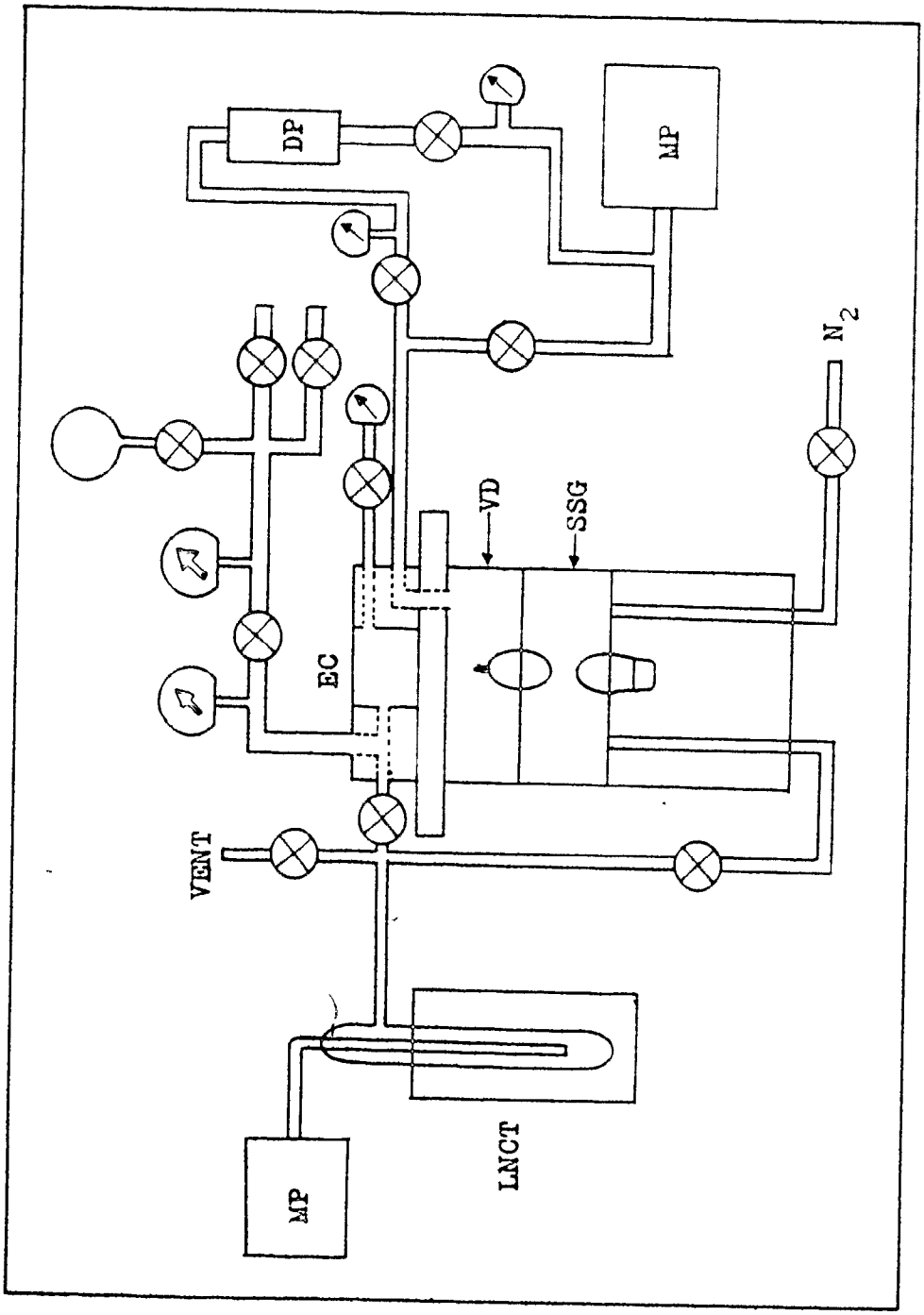
DP
MP
N_2
VD
SSG
EC
VENT
LNCT
MP

not be visually observed, and because dark spots were found on the plexiglass at the insulator-cathode and insulator-ground plate junctions. The surface of both the conductor and insulator were then polished (except for the active cathode area). An alternative solution would have been to let the insulator and the conductor meet at an angle, as done by Brau et al [1], and explained by Bergeron [11]. This would have the same effect as surface polishing. Polishing did not solve the problem, and therefore we investigated more carefully the possibility of gas breakdown. When the pressure was increased to ≈ 7-10 Pa, the electron gun ceased operation, and a faint violet-colored gas discharge could be perceived to take place over the longest possible discharge path. In the present configuration this path was between the insulator to cathode and insulator to ground plate junctions. Figure 2-5a shows Paschen breakdown curve in air, for low values of pd (pressure x interelectrode distance), as measured by Pokrovskaia-Soboleva et al [12] under uniform field conditions. We could not quantitatively use the data in Fig. 2-5a because the electric field was non-uniform in our case. Qualitatively, since the applied voltage was extremely large, and since the gas breakdown phenomenon didn't occur at every shot at a pressure of 4-5.5 Pa, we deduced that we were operating in the rapidly varying region of the appropriate "Paschen curve". Consequently a relatively small increase in the vacuum (factors of >2)

Fig. 2-5a) Paschen breakdown curve at low pressure and uniform field (for air), [ref: Pokrovskaia-Soboleva A.S., Klarfeld B.N. Sov. Phys. JETP, 5, No. 7, 812-18 (1957)]. b) Schematic diagram of the Rogowski coil. Primary current (total diode current) (I_p); secondary current (I_s); shunt impedance (Z) (50-Ω co-axial cable). c) Schematic diagram of the Faraday cup with resistive shunt (emerging electron beam current).

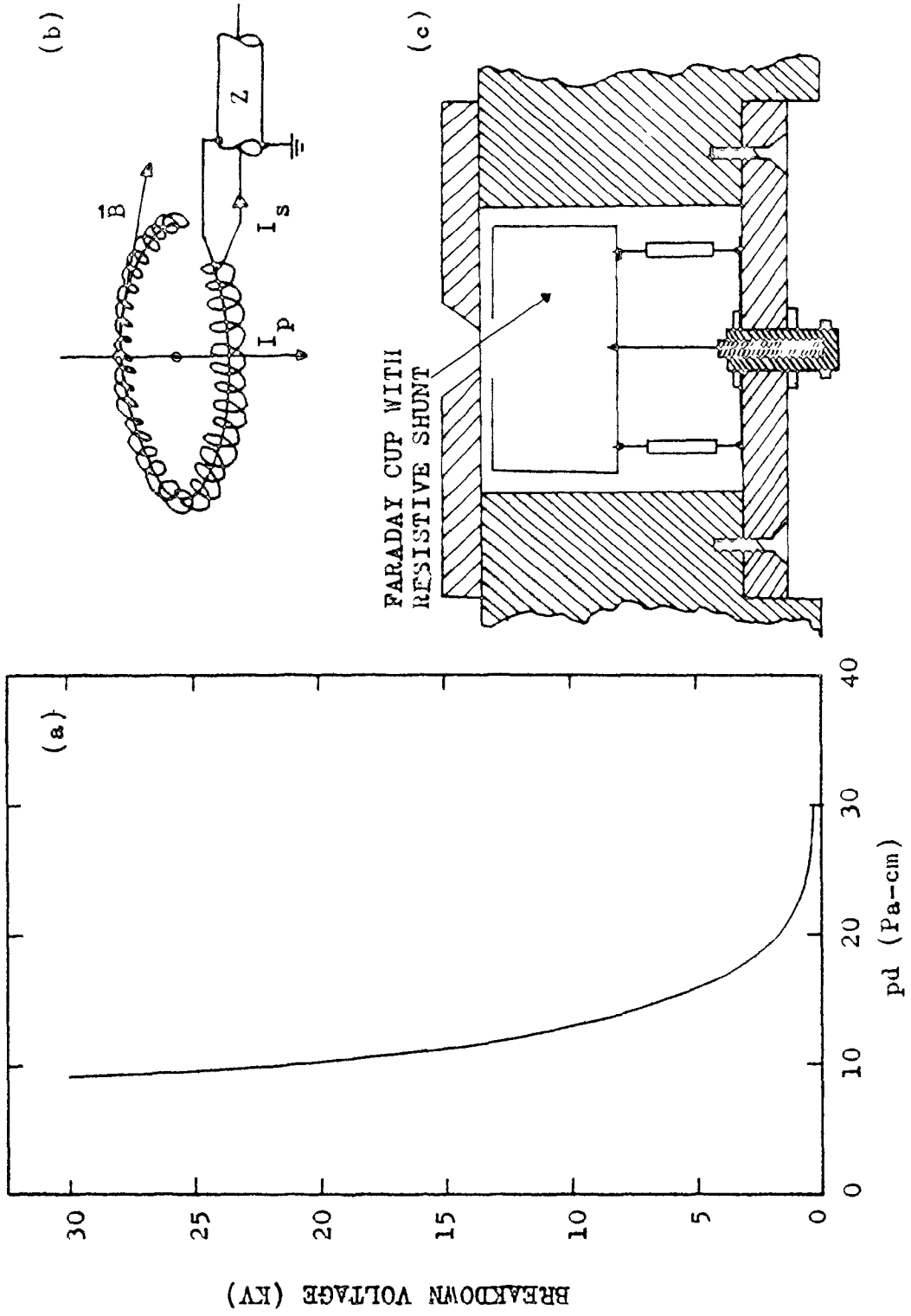
(a)
BREAKDOWN VOLTAGE (KV)
0
5
10
15
20
25
30
0
10
20
30
40
pd (Pa-cm)
(b)
B
Z
I_s
I_p
(c)
FARADAY CUP WITH
RESISTIVE SHUNT

should be sufficient to solve the problem.

The second pumping configuration is shown in Fig. 2-4. The conductivity of the tubing and valves was estimated to be ≈ 0.05 ℓ/s. The estimated ultimate vacuum was 0.2 Pa, compared to a measured value of ≈ 0.65 Pa (the measurement was limited by the gauge). The maximum operational pressure range was found to be ≈ 2.5-3.0 Pa. This indicated that with a sufficiently high system conductivity a good mechanical pump (limit ≈ 1.3 Pa) would be adequate.

Carbon and lead have been used as cathode materials in the present experiment because both materials have short cathode plasma build-up time. Bugaev et al [7] have reported that carbon and lead have delay times of 6 and 12 ns, respectively, at a macroscopic field strength of 600 KV/cm. The active end of the carbon cathodes had a spherical surface. Assuming the field to be nearly spherical around the end, the macroscopic field is approximately given by V/r. With r ≈ 1.6 mm, as used here, we get a field amplitude of 600 KV/cm for an applied voltage of 100 KV. The end surface of the lead cathode was made slightly "ellipsoidal" with the major axis oriented along the length of the rod. The macroscopic field strength was consequently larger than in the case of the carbon cathode, and the difference in the delay time was reduced. However, the active area was reduced with a corresponding reduction in electron beam current and area. As mentioned earlier in this section, the build-up time varies inversely with the density

of whiskers. In order to increase the effective area (i.e. whisker density) of the active end, the cathodes were not polished.

The anode was made of stainless steel mesh having a transparency of ≈ 37%. The mesh was cleaned with acetone before insertion in the chamber to prevent early closure of the gap (by removing oils, which are hydrogen rich). An aluminum foil "window" separates the vacuum diode from the experimental cell.

2.1.3 Performance

In the present section we report the measured characteristics of the total current beam (incident on the diode anode) and emerging electron beam (from the aluminum foil), as observed under various experimental conditions.

The diagnostics employed a Rogowsky loop to measure the total current, and a Faraday cup to collect and measure the electron beam current. A theory of the Rogowsky loop, viewed as a delay line, has been developed by Nassisi et al [13]. They found that when $z << R_o$ (z is the shunt impedance Fig. 2-5b, and R_o the characteristic impedance of the line) the probe behaves as a self integrating circuit with a calculated sensitivity N/Z (N is the number of turns). This result is identical to that obtained by considering the loop as a simple LR circuit when $\omega L >> R$, (see, e.g., Klein [14]).

In the present case the Rogowsky loop consisted of ≈ 430 turns of # 28 magnet wire wound on a 6-mm diameter polyethelene tube core ($\mu_r \approx 1$). A core of higher magnetic permeability would increase the line inductance per unit length and consequently improve its self integrating characteristics. However, this would introduce undesirable saturation effects at high frequencies (> 100 MHz). The spurious signals caused by the helical nature of the winding were eliminated by passing the return ground conductor inside the plastic core, as shown in Fig. 2-5b. The Rogowsky loop was shunted by an impedance-matched 50-Ω coaxial cable. The loop inductance was L ≈ 23 μH and its characteristic impedance ≈ 1500 Ω. Both the calibrated sensitivity, 8.6 A/V, and the decay time, 460 ns, are in good agreement with the values given by N/Z and L/Z.

An ideal collector of incident electron would behave as a black body, and furthermore, would accept all electrons emerging from the foil into solid angle 2π. A real system has to be a compromise. In a recent publication, Turner et al [15] have demonstrated the major importance of optimizing the solid angle subtended by the aperture at the bottom of the cup (escape angle). Their work, performed with 100 KeV electrons incident on carbon and aluminum Faraday cups, has shown that for escape solid angle larger than ~ 0.1 π for carbon and ~ 0.08 π for aluminum most of the backscattered electrons escape from the cup. For escape solid angles less than 0.05 π

(carbon) and 0.03 π (aluminum) most of the electrons were collected.

The Faraday cup schematically shown in Fig. 2-5 c) was assembled from brass sheets, of thickness 75 μm for the walls and top, and 100 μm for the bottom. The base thickness corresponds to approximately 6.25 times the extrapolated range for 100 KeV electrons incident on brass [16]. This prevents the loss of electrons by transmission through the surfaces of the Faraday cup. Because of the small size of the experimental cell in Fig. 2-2, the Faraday cup configuration used represented a practical compromise between the input and escape angles. The solid angle subtended at the centre of the foil by the aperture is 1.6 π, and the escape solid angle is 0.2 π, which is somewhat greater than the optimum value. The latter can be seen by extrapolating the results of Turner et al [16] to brass (which has a larger backscatter coefficient than aluminum). The fraction of electron lost is $<30\%$ at 100 KeV incident energy. Since brass is typically composed of 65% Cu, 34.5% Zn, 0.5% Pb, the backscatter coefficient observed in copper [30] for 100 KeV electrons [15] is a good approximation to the actual case. We expect the measured electron-beam current to be less than the true current. However, the correction factor (<1.4) is not known. Therefore only the raw uncorrected data are given in this section.

The output signal appears across a low-inductance 0.625Ω resistor formed from an array of sixteen 10Ω carbon resistors in parallel. The cup was operated in vacuum of ~ 2Pa, in order to prevent plasma return currents from shorting the shunt resistance.

Two methods were used to investigate the electron-beam uniformity. The first method consisted of placing a glass plate covered with phosphorescent paint in the electron-beam path. That simple method presented two major drawbacks. The beam was "visible" only for a short period of time (~ 1 sec). It was also difficult to spread the paint evenly over the glass plate, which made it hard to determine if the observed variations in the phosphorescense were caused by phosphor or electron-beam non-uniformity. The second method consisted of replacing the glass plate by photographic paper. Although the exposure time could not be adjusted, reasonable image contrast was obtained by the use of dilute developers. Still, only qualitative informations about the absolute beam uniformity could be obtained in this way. However, the method permitted us to distinguish between definitely non-uniform and apparently uniform cases. A qualitative method has been used by Parker et al. [6], but couldn't be applied in the present case because the necessary equipment was not available.

The remainder of this section is concerned with the measured electrical characteristics of the electron-beam system.

Typical total current pulses are shown in Fig. 2-6. The first oscillogram was obtained after application of the voltage pulse, to a carbon cathode. This voltage pulse was produced by a positively charged spiral generator connected as shown in Fig. 2-1 (configuration I). The remaining oscillograms were obtained after reversal of the charging cables (configuration II) (in some cases, also using different cathode material and gap spacing). The generator configuration used in the first case (configuration I) has the advantage of an effective output capacitance given by Eq. (2.1-3), which is larger than can be obtained with the generator connected in configuration II. However, there are disadvantages. These are lower available peak voltage, departure from the normal diode operation mode of the vacuum diode, and non-uniformity of the electron-beam. The first disadvantage has already been described in Section 2.1.1. The second is illustrated, in part, by Fig. 2-6a. After the first negative pulse, the current flow reverses direction, and reaches its peak after an elapsed time of $2\tau \simeq 240$ ns (not shown in Fig. 2-6a), and finally returns back to zero without further oscillation. The oscillograms shown in Fig. 2-6 a and b have been obtained under the same experimental conditions except for the voltage pulse polarity. Figure 2-6 b has proper vacuum-diode behavior. The third oscillogram (c), which was obtained with a lead cathode, is similar to Fig. 2-6b. A reduced spacing results in oscillogram (d). In this

Fig. 2-6 Oscilloscope records showing typical total-diode-current pulses. a) The generator was connected as shown in Fig. 2-1 (configuration I) and was initially charged to 12 KV. The series spark gap pressure was $\sim$ 191 KPa. The electron beam was produced by a carbon cathode with a 3.5 mm gap. b) The generator high voltage was connected in configuration II (second voltage peak negative), and was initially 10 KV. The series spark gap pressure was $\sim$ 191 KPa. A carbon cathode with a 3.5 mm gap was used. c) The generator high voltage was connected as in configuration II and was initially 9.5 KV. The series spark gap pressure was $\sim$ 253 KPa. A lead cathode with a 2.7 mm gap was used. d) Every parameters were identical to those used in c) except for the gap spacing which was 1.5 mm.

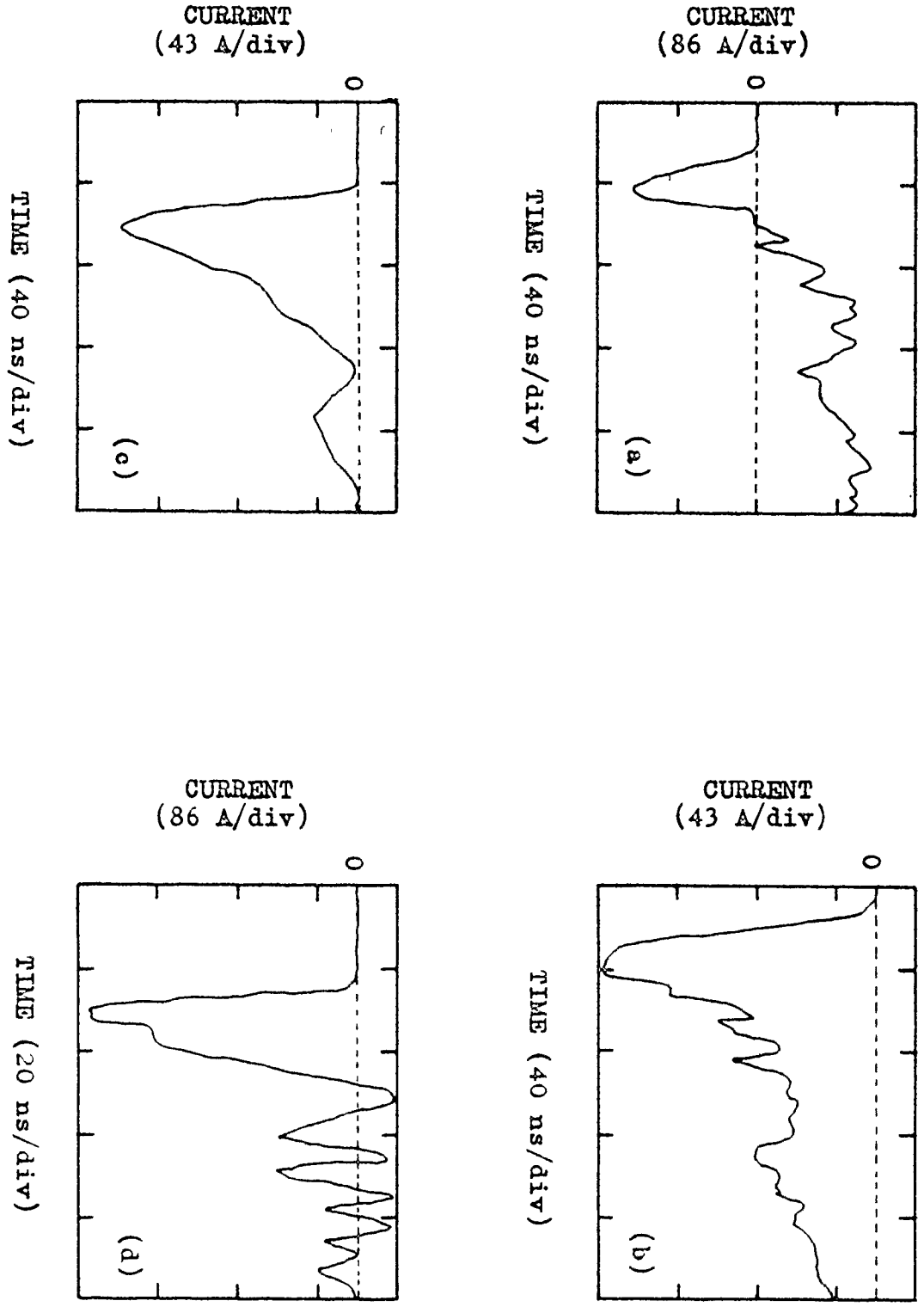
CURRENT
(86 A/div)
0
TIME (40 ns/div)
(a)
CURRENT
(43 A/div)
0
TIME (40 ns/div)
(b)
CURRENT
(43 A/div)
0
TIME (40 ns/div)
(c)
CURRENT
(86 A/div)
0
TIME (20 ns/div)
(d)

case the current rises to a peak value of 340 ± 80 A in approximately 5 ns (with a charging voltage of 9.5 KV and an N_2 pressure of 250 KPa), to give a pulse width of ~ 20 ns FWHM. However, an electron-beam current has not been observed in this configuration, for reasons which are not fully apparent. The most likely explanation is that the discharge starts from the cathode and propagated toward the side of the anode, thereby preventing an incident electron-beam on the foil.

For each cathode material and gap spacing investigated we have found that an increment in the charging voltage resulted in a corresponding increment of the total current, as shown in Fig. 2-7 a. There were no systematic changes in the peak current when the spark-gap pressure was made the running variable and the charging voltage was kept constant, as shown in Fig. 2-7b.

As mentioned in Section 2.1.2, Bugaev et al. [7] have shown that the cathode plasma expands radially at a typical velocity of 2-3 cm/μs. They also show that the electrons are emitted from the surface of that plasma, and that the current is space charge limited. The expected diode closure time is therefore 85-125 ns for a 2.5 mm gap. If it is assumed that the generator produces a "step type" voltage pulse, then the apparent closure time is ~ 15 ns for all gaps investigated in the range 2.3-4.0 mm. The stainless -

Fig. 2-7 a) Total diode peak current, as a function of the spiral generator charging voltage. b) Total diode peak current, as a function of the series spark gap nitrogen pressure. The "error bars" (standard deviation from the average) show the typical scatter between various shots.

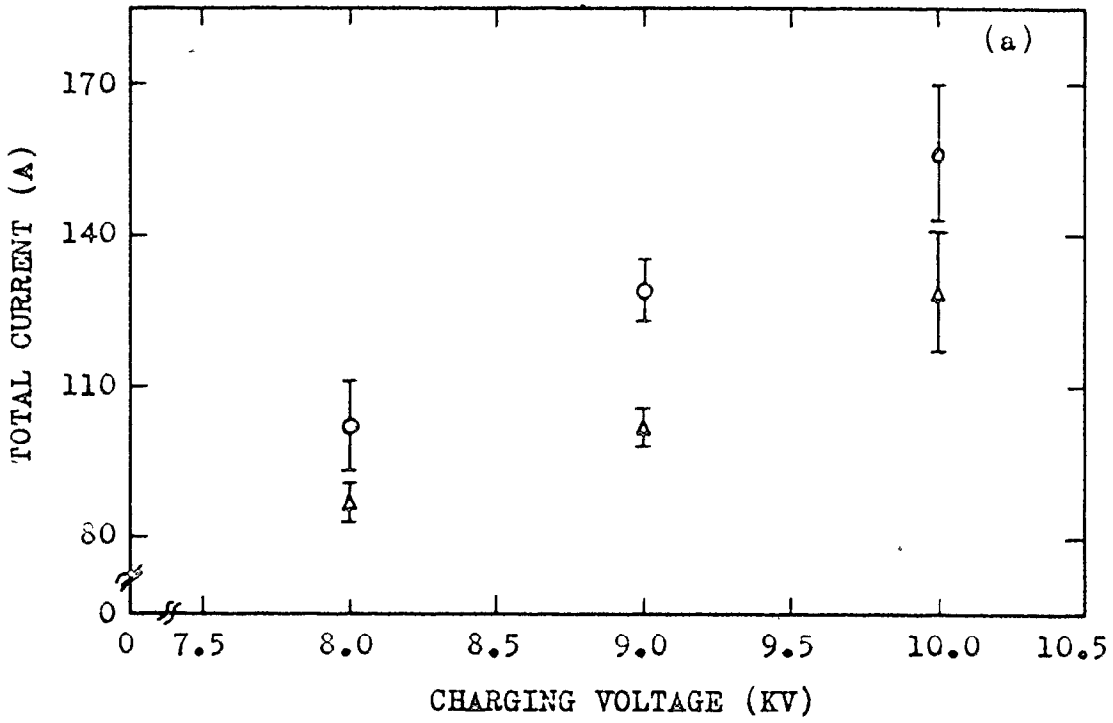
(a)
TOTAL CURRENT (A)
170
140
110
80
0
0
7.5
8.0
8.5
9.0
9.5
10.0
10.5
CHARGING VOLTAGE (KV)

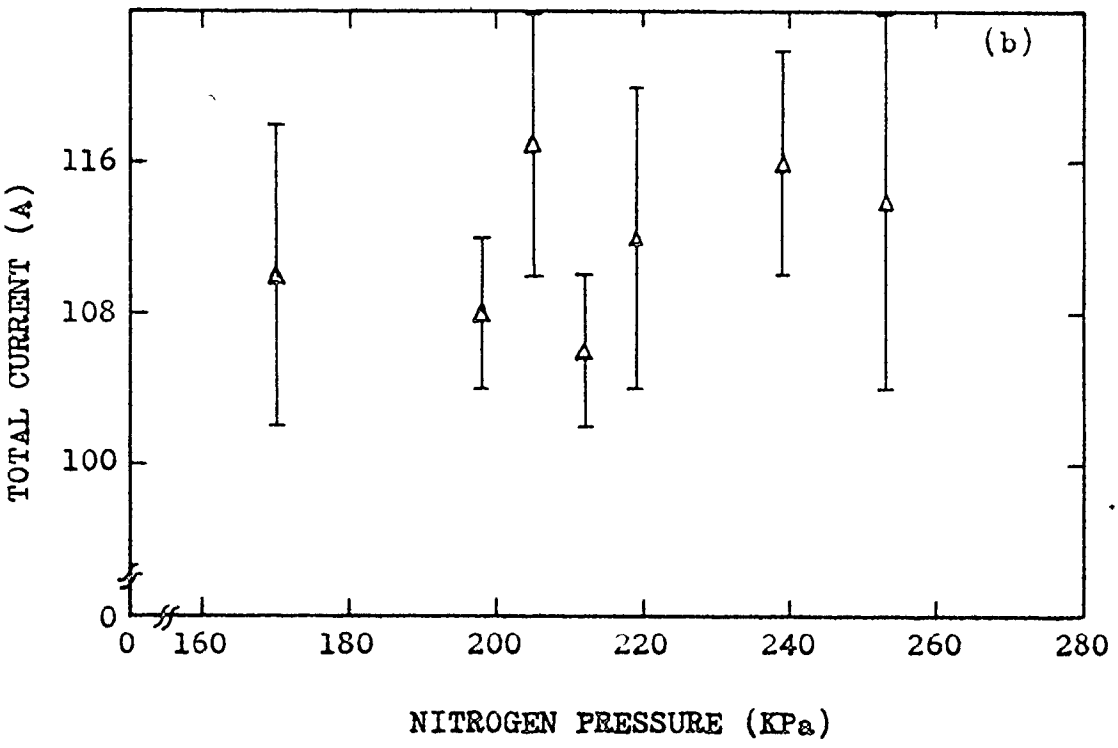
(b)
TOTAL CURRENT (A)
116
108
100
0
0
160
180
200
220
240
260
280
NITROGEN PRESSURE (KPa)

steel mesh anode was carefully cleaned. Therefore the discrepancy in closure time cannot be explained by the presence of low molecular weight impurities deposited on the anode, which would give a closure time of $\lesssim$ 25 ns. A reasonable explanation is that the actual voltage pulse is not a step function. The experimental diode closure time can be determined by simultaneous measurement of the voltage and current pulse in the gap. We were not able to do this because our high voltage probe had an upper limit of 40 KV.

In order to verify that the current peak was space-charge limited, we have compared the measured current pulse with that calculated by means of a simple space-charge-limited current flow model.

In our model we assume that the tip of the cathode is initially uniformly covered by the electron emitting plasma. The cathode plasma then start to expand radially at a velocity $v_{Bug} \sim 2\text{-}3$ cm/μs. The effective tip radius r and gap distance d, shown in Fig. 2-8 a, vary in time according to the equations.

$$r(t) = r_o + v_{Bug}t \quad , \qquad (2.1 - 7\ a)$$

$$d(t) = d_o - v_{Bug}t \quad . \qquad (2.1 - 7\ b)$$

The tip is now divided into infinitisimal steps, to each of which is applied the one dimensional Child-Langmuir law [17] which gives the space-charge-limited current-density.

Fig. 2-8 Space charge limited current flow model. a) The cathode plasma sheath. The "effective radius" of the active end of the cathode is r and the effective gap spacing is d. b) Step model of the cathode plasma sheath. c) Typical total diode current pulses obtained with lead cathodes. The gap spacings were 2.7 mm (left side) and 1.5 mm (right side). The full curves correspond to the measured total diode current pulses, and the dashed curves correspond to the calculated values.

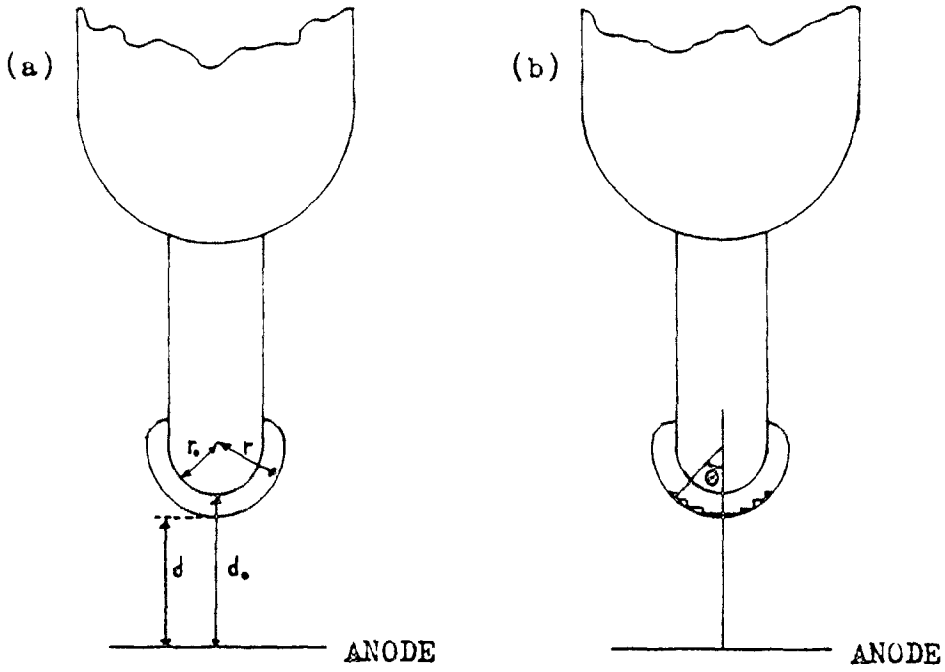
(a)
(b)
r
r
d
d
ANODE
ANODE

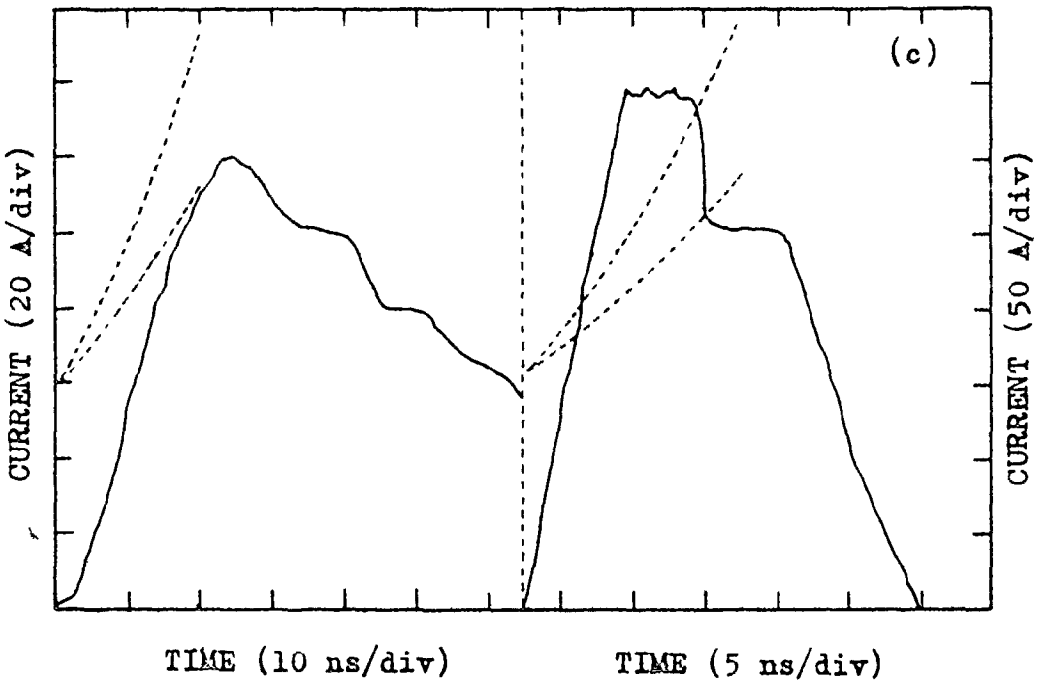
(c)
CURRENT (20 A/div)
CURRENT (50 A/div)
TIME (10 ns/div)
TIME (5 ns/div)

Such a representation is obviously inexact, but it should provide results of sufficient accuracy for the present comparison. The current density emitted by a step located at angle θ (as defined in Fig. 2-8b) is

$$I(\theta,t) = \frac{2.3 \times 10^{-6} V^{3/2}(t)}{[d(t) + r(t)(1 - \cos\theta)]^2}, \qquad (2.1\text{-}8)$$

and the total current is

$$I_{tot}(t) = 1.45 \times 10^{-5} V^{3/2}(t) \times \left[\ln\left(\frac{d(t)}{d(t) + r(t)}\right) + \frac{r(t)}{d(t)}\right]. \qquad (2.1\text{-}9)$$

Figure 2-8c compares the measured current pulses obtained with gap spacings of 2.7 and 1.5 mm to the corresponding space-charge-limited current given by Eq. (2.1-9). A constant gap voltage of approximately 100 KV was used in the calculation.

Figure 2-9 shows four current pulses measured by means of the Faraday cup. All these oscillograms were recorded using a stainless steel mesh anode of transparency ~ 37%. The beam was further attenuated by a nickel mesh of 55% transparency in the first three cases, and in the fourth case by the nickel mesh and an additional stainless steel mesh of ~ 37% transparency. The overall transparency, calculated by taking the product of the individual transparency factors, is ~ 20% for (a), (b) and (c), and 7.5% for (d).

The oscillogram of Fig. 2-9a has been obtained by operating the vacuum diode with the first voltage peak negative

Fig. 2-9 Oscilloscope records showing typical emerging electron beam current pulses. a) The generator high voltage was connected as in configuration I (see Fig. 2-1) and the initial charging voltage was 11.4 KV. The series spark gap nitrogen pressure was ~ 182 KPa. The cathode material was carbon and the gap spacing 3.5 mm. b) The generator was initially charged to 10 KV, and the high voltage was connected as in configuration II (reversed polarity). The series spark gap N_2 pressure was ~ 191 KPa. The cathode material and gap spacing are identical to that of a). An 18-μm thick aluminum foil have been used in both cases a) and b). c) The charging voltage was 9.5 KV, (configuration II). The series spark gap pressure was 205 KPa. The cathode material was lead and the gap spacing was ~ 2.7 mm. d) The charging voltage was 10 KV. The series spark gap N_2 pressure was 225.5 KPa. The cathode material was lead and the gap spacing 2.5 mm. A 26-μm aluminum foil window was used for both c) and d).

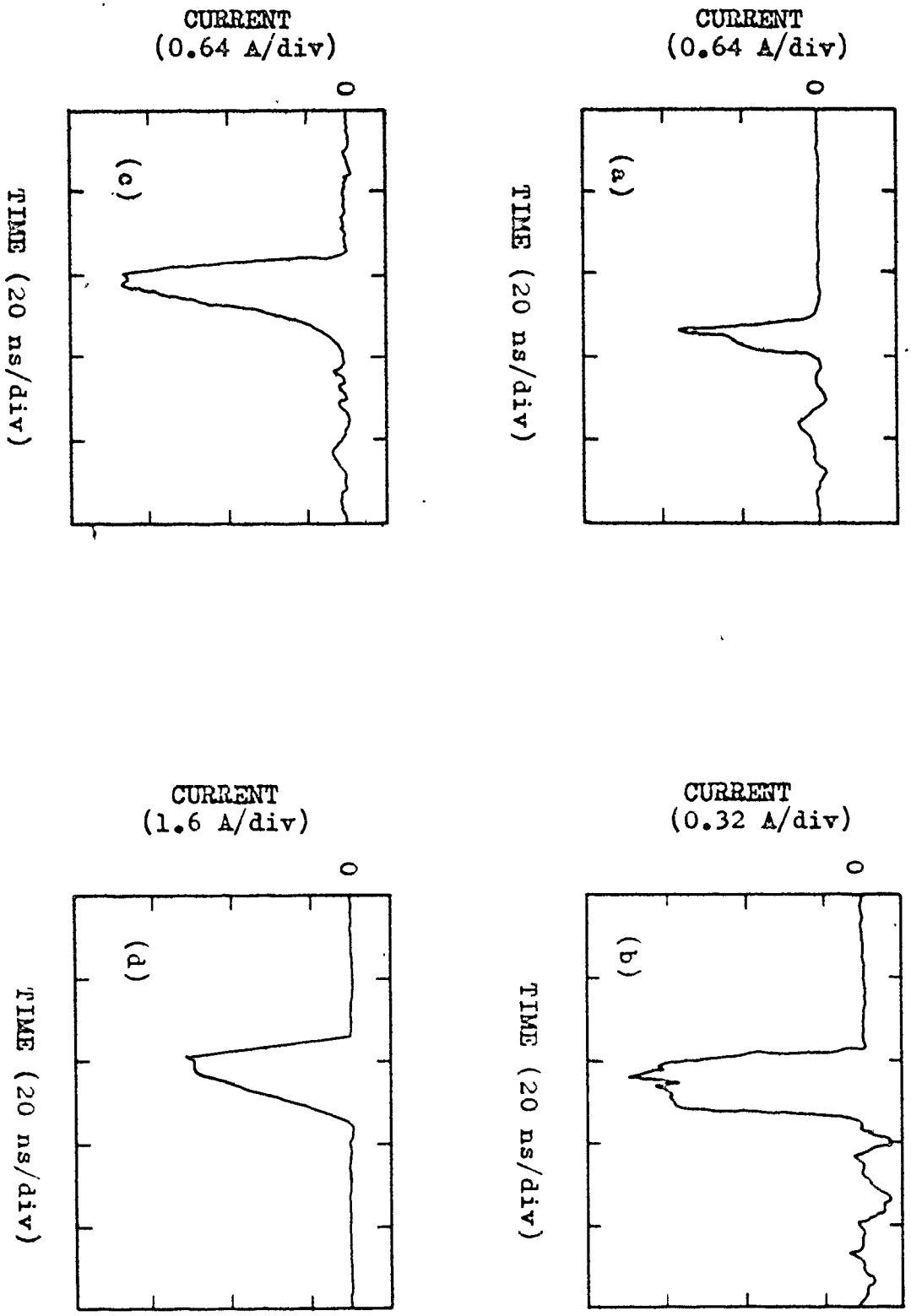
CURRENT
(0.64 A/div)
0
(a)
TIME (20 ns/div)
CURRENT
(0.64 A/div)
0
(c)
TIME (20 ns/div)
CURRENT
(0.32 A/div)
0
(b)
TIME (20 ns/div)
CURRENT
(1.6 A/div)
0
(d)
TIME (20 ns/div)

(configuration I). In this configuration the electron-beam always appears at the side of the output window, and is therefore highly non-uniform. After adjustment of the series spark-gap pressure to ~ 253 KPa (best conditions), we obtained average current pulse widths of 12 ns FWHM, and peak current values of 2.2 ± 0.9 A (through a 26-μm thick aluminum foil). The observed large scatter between shots (40%) is explained by the combined effect of voltage pulse fluctuations and beam non-uniformity. The second oscillogram was obtained after reversal of the positions of the charging cables (configuration II for the spiral generator). Qualitatively the overall beam uniformity was reasonably good, with the exception that abrupt changes in the current density, caused by the nickel and stainless steel meshs, occurred over lenghts of ~ 200μm. In addition the electron-beam pulse shape was found to vary considerably between shots. Typical scatters in the value of the peak current were found to be 25% and 30% for the 4.8 mm and 3.5 mm gaps, respectively, over the whole range of pressure (160-230 kPa) and charging voltage (8-11 kv) employed. The oscillograms of Fig. 2-9 c and d have been obtained by replacing the carbon cathode with a lead cathode. The pulse shape was found to be reproducible from shot to shot (but not the amplitude). Under the best conditions (series spark-gap N_2 pressure ~ 253 KPa) the average pulse width in Fig. 2-9c was ~13 ns FWHM, and the pulse peak-current was 2.6 ± 0.45 A

through a 26-μm thick aluminum foil (and a total mesh transparency of 20%).

The effect of varying the charging voltage is shown in Fig. 2-10. Figure 2-11 shows the strong dependence of the electron-beam peak current on the spark gap nitrogen pressure. As the N_2 pressure increases, the voltage pulse is switched to the cathode at a higher voltage (i.e. closer to the peak). Consequently, higher energy electrons are created, which are more efficiently transmitted through the foil.

In the present case, when the spark-gap nitrogen pressure increased above 255 KPa, the electron-gun ceased to work properly. Above that pressure breakdown occurred between the high voltage terminal and metallic components of the system.

"Synchronized" total and electron-beam current pulses are shown in Fig. 2-12. The oscilloscope was triggered by the Rogowsky loop signal. Since the pulses have not been measured simultaneously, a direct one-to-one correspondence is not possible. However, typical scatters in the electron-beam peak and the total peak current positions are ± 2ns. Therefore, the electron beam peak position relative to the total current peak is accurate to ~ ± 3ns. Oscillograms (a) and (b) (in Fig. 2-12) show that the electron beam current reaches its peak during the rise of the total current. This is caused by the effects of temporal changes in electron energies over the rise time of the current pulse, and at later times by the

Fig. 2-10 Peak emerging electron beam current as a function of the charging voltage. The "error bars" (standard deviation) show the typical scatter between various shots.

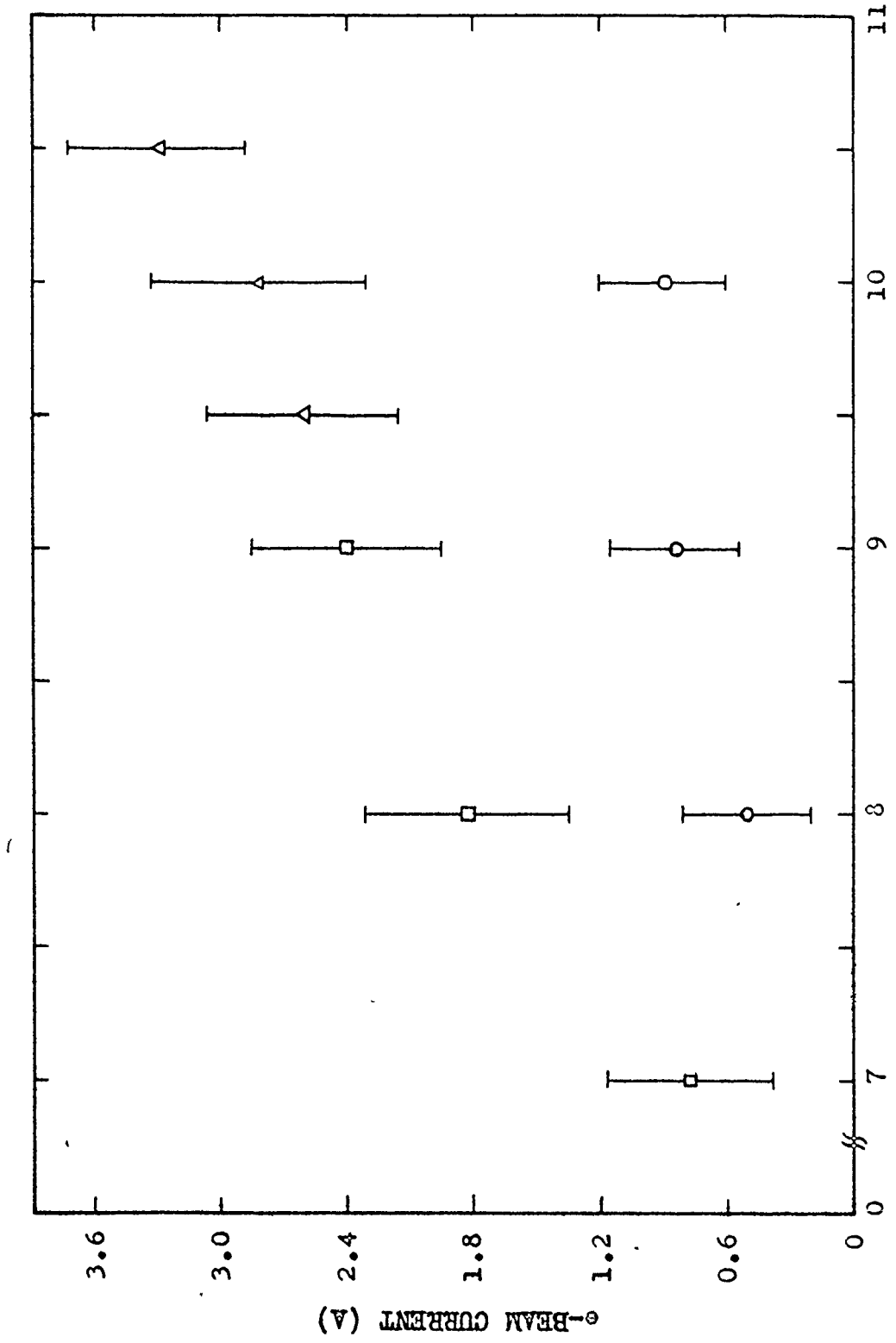
e-BEAM CURRENT (A)
3.6
3.0
2.4
1.8
1.2
0.6
0
7
8
9
10
11
CHARGING VOLTAGE (KV)

Fig. 2-11 Peak emerging electron-beam current as a function of the series spark gap nitrogen pressure. The "error bars" (standard deviation) show the typical scatter between various shots.

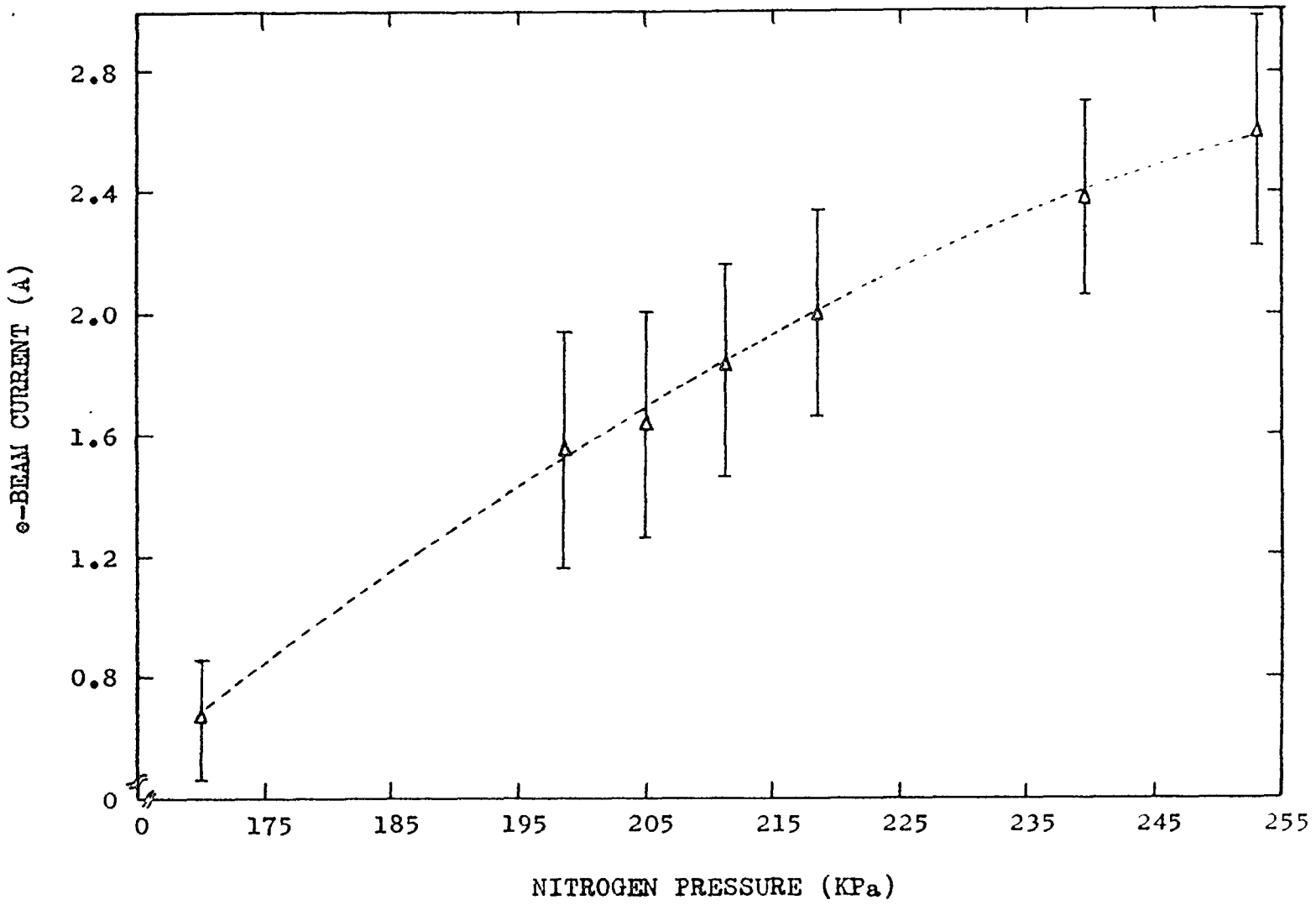
e-BEAM CURRENT (A)
2.8
2.4
2.0
1.6
1.2
0.8
0
0
175
185
195
205
215
225
235
245
255
NITROGEN PRESSURE (KPa)

Fig. 2-12 Oscilloscope records showing "synchronized" total diode current pulses (upper traces) and emerging electron beam current pulses (lower traces). a, b) The charging voltage was 9.5 KV. The series spark gap pressure was ∿ 198 KPa. The aluminum foil thickness was ∿ 26 μm; and the anode transparency ∿ 20%. c),d) The charging voltage was 10 KV. The series spark gap pressure was ∿ 225 KPa. Aluminum foil was not used, and the anode transparency was ∿ 7%. In each case, the cathode material was lead, the gap spacing ∿ 2.5 mm, and the generator high voltage connected as in configuration II (second voltage peak negative).

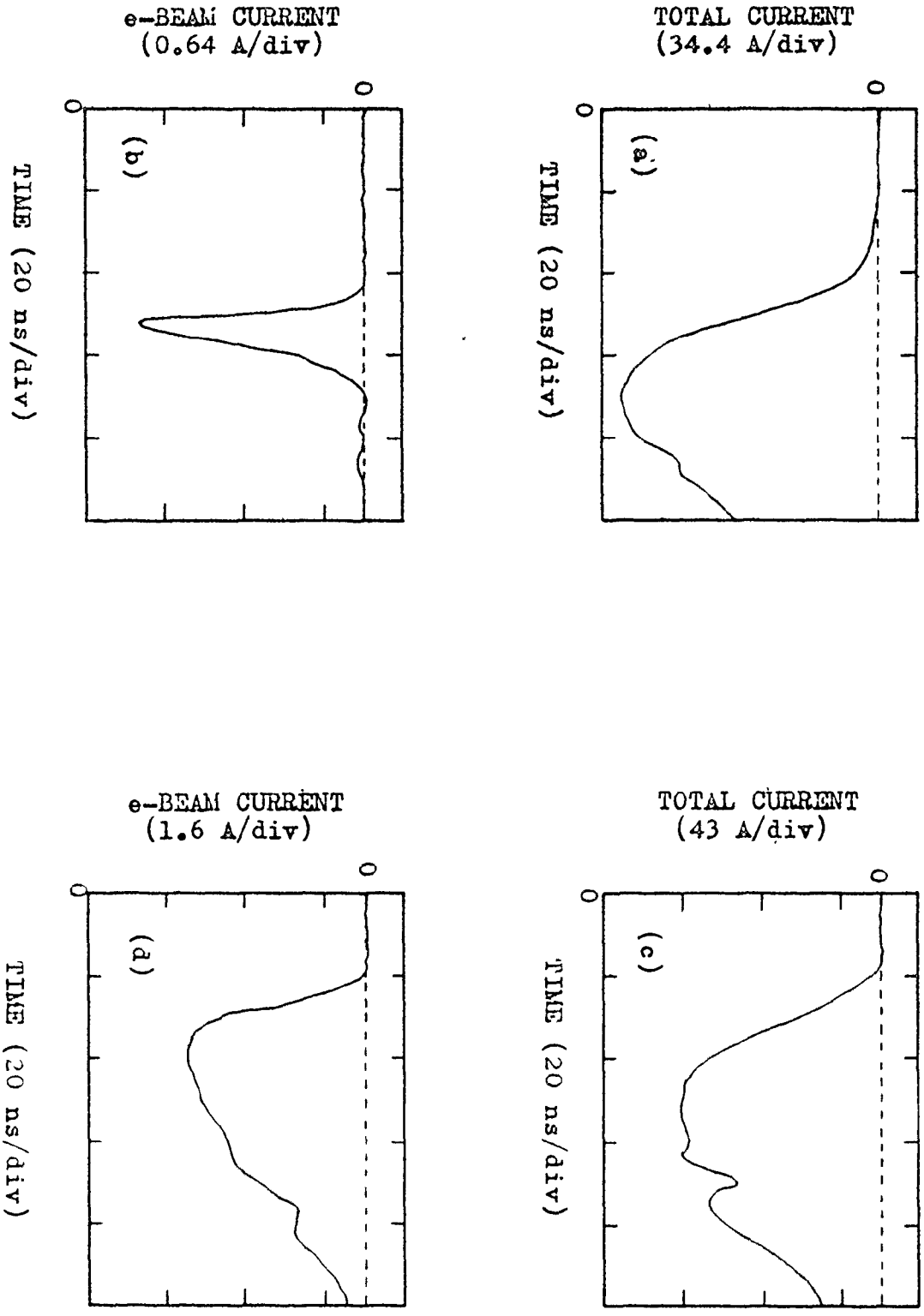
TOTAL CURRENT
(34.4 A/div)
0
0
(a)
TIME (20 ns/div)
e-BEAM CURRENT
(0.64 A/div)
0
0
(b)
TIME (20 ns/div)
TOTAL CURRENT
(43 A/div)
0
0
(c)
TIME (20 ns/div)
e-BEAM CURRENT
(1.6 A/div)
0
0
(d)
TIME (20 ns/div)

significant contribution of the heavy ions released at the anode to the conductivity of the diode. Figures 2-12 c and d were obtained after removal of the aluminum foil. The electron-beam peak position is still shifted relatively to the total current peak, and decays more rapidly than the total current. Both of these effects can be explained by the heavy-ions current.

If we assume that the electron energy distribution is narrowly peaked about its average at any time, then the "average-energy" time-dependence can be determined by carefull measurements of the aluminum foil transmission coefficient [16]. Unfortunately, the actual time resolution of ± 3ns is not sufficient for this purpose. However, it is still possible to find a lower bound for the electron energy at the current peak. The ratio of the e-beam peak current measured with and without the foil, can be taken as the transmission coefficient of the foil. This transmission coefficient is found to depend solely upon the series spark-gap pressure. The estimated electron energies are, 74-75 KeV and 80-81 KeV, at 225 KPa and 239 KPa, respectively [16]. These values are lower than the expected peak voltage of 90 and 100 KV produced by the generator at a charging voltage of 9 and 11 KV, respectively.

It should be noted that the transmission coefficient of the foil is less than 5% and 1% for electron energies smaller than 65 and 63 KeV, respectively [16]. Since the electron-beam current becomes negligible (<1% of its peak) by the time

the total current arrives at its peak (see Figs. 2-12a and b), we deduce that the gap voltage at that time is less than 63 KV.

To complete the characterization of the present electron-beam gun, we need to determine the effect of scattering in the foil on the output electron-beam angular spread.

When an electron-beam is incident on a solid slab the electrons penetrate into the solid and suffer collisions with the nuclei. The resultant scattering causes an increase in the angular spread of the beam. If the slab is thick enough for the electrons to make several collisions, then multiple-electron-scattering theories have to be considered. The problem has been a topic of interest for the last half-century. A few of the theoretical works on the subject are given in the references [18-24]. Jacob [18] has recently shown that the transport equation for electrons through a slab is solvable when the energy loss is neglected. He has further developed a method for treating the problem of penetration and energy deposition of electrons in thick targets [19]. In spite of the fact that his methods are expected to give the best results, they have been neglected in favor of simpler theories which never require us to write complicated computer codes. The theory used is that due to Goudsmit and Saunderson [20], as connected to Molières's [21] by Bethe [22]. The Goudsmit-Saunderson theory has two major drawbacks. It assumes

that all electrons "see" the same target thickness and it never includes the boundary conditions. The numerical approach of Jabob [18] eliminates these difficulties.

In the present case we assume that all electrons travel through the slab over a path length equal to the foil thickness. It has been shown by Jacob [18] that even at large angle the error due to this assumption should not be more than a factor of 2, which is adequate for the present purpose.

After traversing a thickness t in the foil, the number of electrons in the angular interval θ, $\theta+d\theta$ is given by

$$f_{GS}(\theta,t) \quad \sin\theta \; d\theta, \tag{2.1-10a}$$

or $$f_{M}(\theta,t) \quad \theta \quad d\theta, \tag{2.1-10b}$$

where $f_{GS}(\theta,t)$ is the Goudsmit-Saunderson distribution function, and $f_{M}(\theta,t)$ is the Molière distribution function (where $\sin\theta$ is replaced by θ for small angles).

The simplicity of Molière's theory lies in the fact that the angular distribution depends only on the ratio of the "unit probability angle" χ_c, which describe the foil thickness, to the screening angle χ_a', which describes the scattering atoms. The "unit probability angle" is given by the equation

$$\chi_c^2 = 4\pi \; Ntr_o^2 \; Z(Z+1) \; (1-\beta^2)^{0.5}/\beta^4, \tag{2.1-11}$$

where $r_o = 2.83 \times 10^{-15}$m is the "classical electron radius", Z is the atomic number of the scattering atom, t is the length of the electron path, N is the scattering atom number density, $\beta = v/c$ (the ratio of the electron velocity to the velocity of light). The physical meaning of χ_c is that the total probability of single scattering through an angle greater than χ_c is exactly one. The Dalitz screening angle [18] is used in the present case instead of the expression derived by Molière [21]. Nigam et al. [25] have pointed out calculation errors in the latter expression. The screening angle is therefore given by:

$$\chi_a'^2 = 1.167\chi_o^2[1 + 4\alpha\chi_o\,(\frac{1-\beta^2}{\beta}\ln\chi_o + \frac{0.231}{\beta} + 1.448\beta)], \qquad (2.1\text{-}12)$$

where $\chi_o = h\mu Z^{1/3}/(0.885\, a_o p)$, and where $\mu = 1.12$ (for the Thomas-Fermi atom), a_o is the Bohr radius, $\alpha = Z/137$, and p is the momentum of the electron.

Bethe [22] has shown that

$$\theta f_M(\theta)d\theta = \frac{\theta d\theta}{\chi_c^2}\int_0^\infty y\,dy\, J_o\,(\frac{\theta y}{\chi_c})\,\exp[\tfrac{1}{4}y^2(-b+\ln\tfrac{1}{4}y^2)], \qquad (2.1\text{-}13)$$

where $b = 2\ln(\chi_c/\chi_a')$. After writing $B-\ln B = b, \psi = \theta/(\chi_c B^{0.5})$, and expanding f_M in power of B^{-1}, Bethe [22] finally obtained

$$f_M(\theta)\,\theta\,d\theta = \psi\,d\psi\,[f^{(o)}(\psi) + B^{-1}f^{(1)}(\psi) + + B^{-2}f^{(2)}(\psi) + \ldots], \qquad (2.1\text{-}14)$$

where $f^{(n)}(\psi) = (n!)^{-1}\int_o^\infty \mu d\mu\, J_o(\psi\mu)\, \exp(-\frac{1}{4}\mu^2)[\frac{1}{4}\mu^2 \ln(\frac{1}{4}\mu^2)]^n$.

Bethe [22] has tabulated values of $f^{(o)}$, $f^{(1)}$ and $f^{(2)}$ over a wide range of ψ. He had pointed out that over the whole range of $\theta[0,\pi]$ only $f^{(o)}$ to $f^{(2)}$ are necessary to get a good estimate of $f_M(\theta)$ (to ~ 1%) [22]. It is of interest to note that $f^{(o)}(\theta)$ is given by the Guassian

$$f^{(o)}(\theta) = 2\exp-(\theta^2/\chi_c^2 B) \qquad (2.1\text{-}15)$$

Bethe gives the formal connection between the Molière and the Goudsmit-Saunderson theories, which yields the approximate expression

$$f_{GS}(\theta) = (\frac{\theta}{\sin\theta})^{1/2}\exp(\frac{1}{16}\chi_c^2 B) f_M(\theta) + \frac{1}{24}. \qquad (2.1\text{-}16)$$

In the present case we consider the foil thickness to be 26 μm and the electron energy ~ 90 KeV. We therefore get $\beta = 0.5263$, $\chi_c^2 = 0.3143$, $\chi_a'^2 = 1.435 \times 10^{-3}$, and (after successive trials) $B = 7.3892$. Figure 2-13 shows the Molière distribution function, the Goudsmit-Saunderson distribution function, and the terms $f^{(o)}(\theta)$ and $f^{(o)'}(\theta)$, which are the Gaussians given by Eq. (2.1-15). On the

Fig. 2-13 Intensity of scattered electrons emerging from an aluminum slab per unit angle in the direction "θ". Incident electrons energy ∿ 90 KeV; foil thickness ∿ 26 μm; f_{GS} is the Goudsmith-Saunderson distribution function; f_M is Moliere's; $f^{(0)}$ and $f^{(0)'}$ are Gaussian distribution functions(1/e width; $\chi_c B^{\frac{1}{2}}$ and $\chi_c (B-1.2)^{\frac{1}{2}}$ respectively).

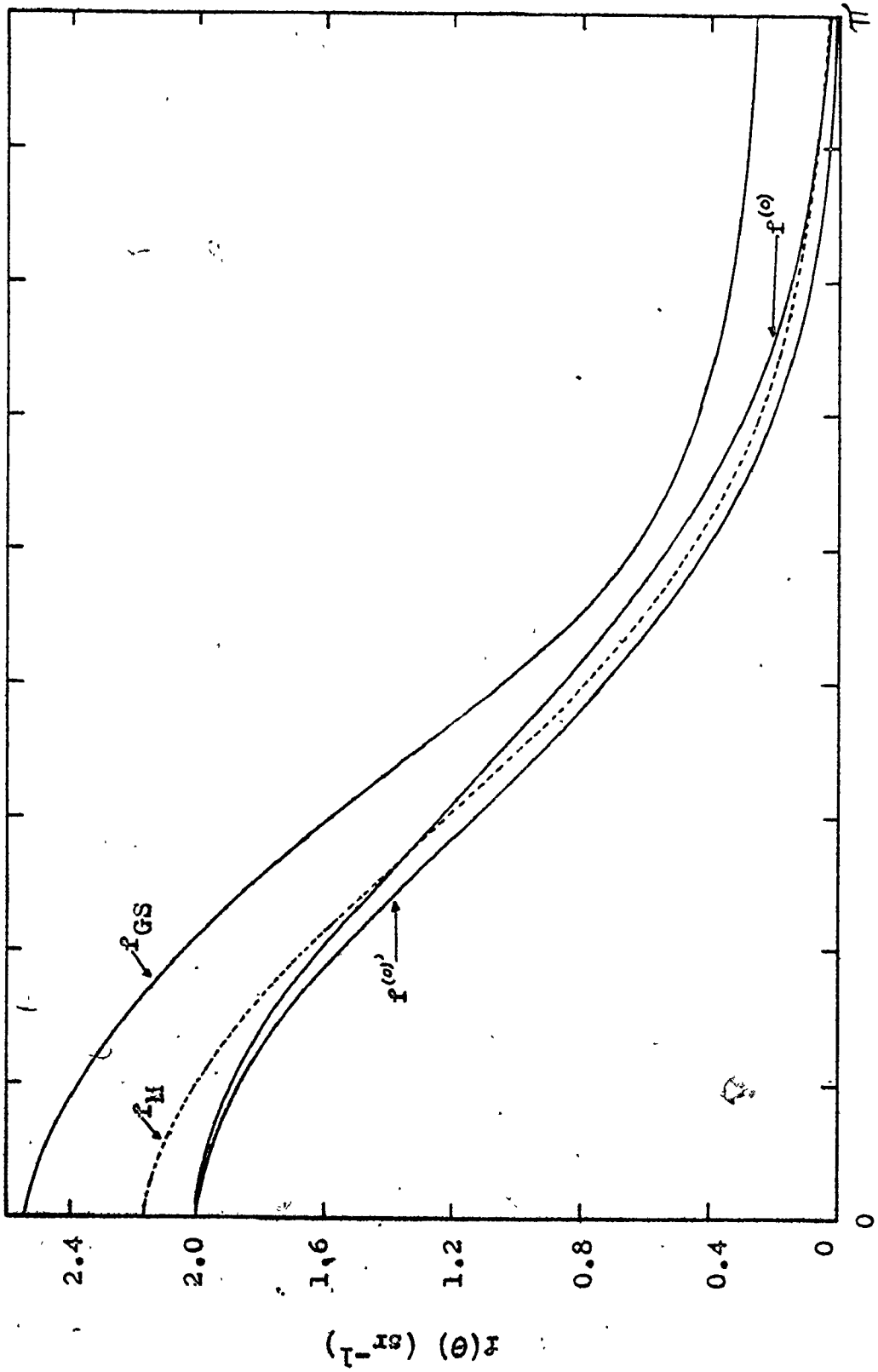
f_{GS}
f_{HT}
$f^{(o)'}$
$f^{(o)}$
$r(\theta)$ (sr^{-1})
2.4
2.0
1.6
1.2
0.8
0.4
0
0
π
θ (radians)

latter the 1/e width $\chi_c B^{1/2}$ is replaced by $\chi_c (B-1.2)^{1/2}$, as suggested by Hanson et al. [26]. They have pointed out that a better small angle approximation for $f_M(\theta)$ is obtained by using a Gaussian of slightly smaller width than $f^{(o)}(\theta)$.

Another drawback of the present theory is that it considers the electron energy loss to be negligible while traversing the foil. This is not exact because the stopping power of aluminum for 90 KeV electrons is ~ 9.4 MeV/cm, which means that the electrons lose ~ 24.5 KeV by passing through a 26-μm thickness in Al. This effect, which contributes to increase the spread of the electron angular distribution, has been considered by Jacob [19] and Spencer [27].

2.2 Conductivity Cell

The present arrangement, which will be described in detail in the following Sections, is based on the original design of Schneider and Brau [28]. The experimental conductivity cell, shown in Fig. 2-14, consists of a high pressure chamber, and a bias circuit with electrodes used to maintain both a constant voltage and a uniform field in the plasma region.

Fig. 2-14 Cross sectional view of the apparatus showing the conductivity cell and the bias circuit.

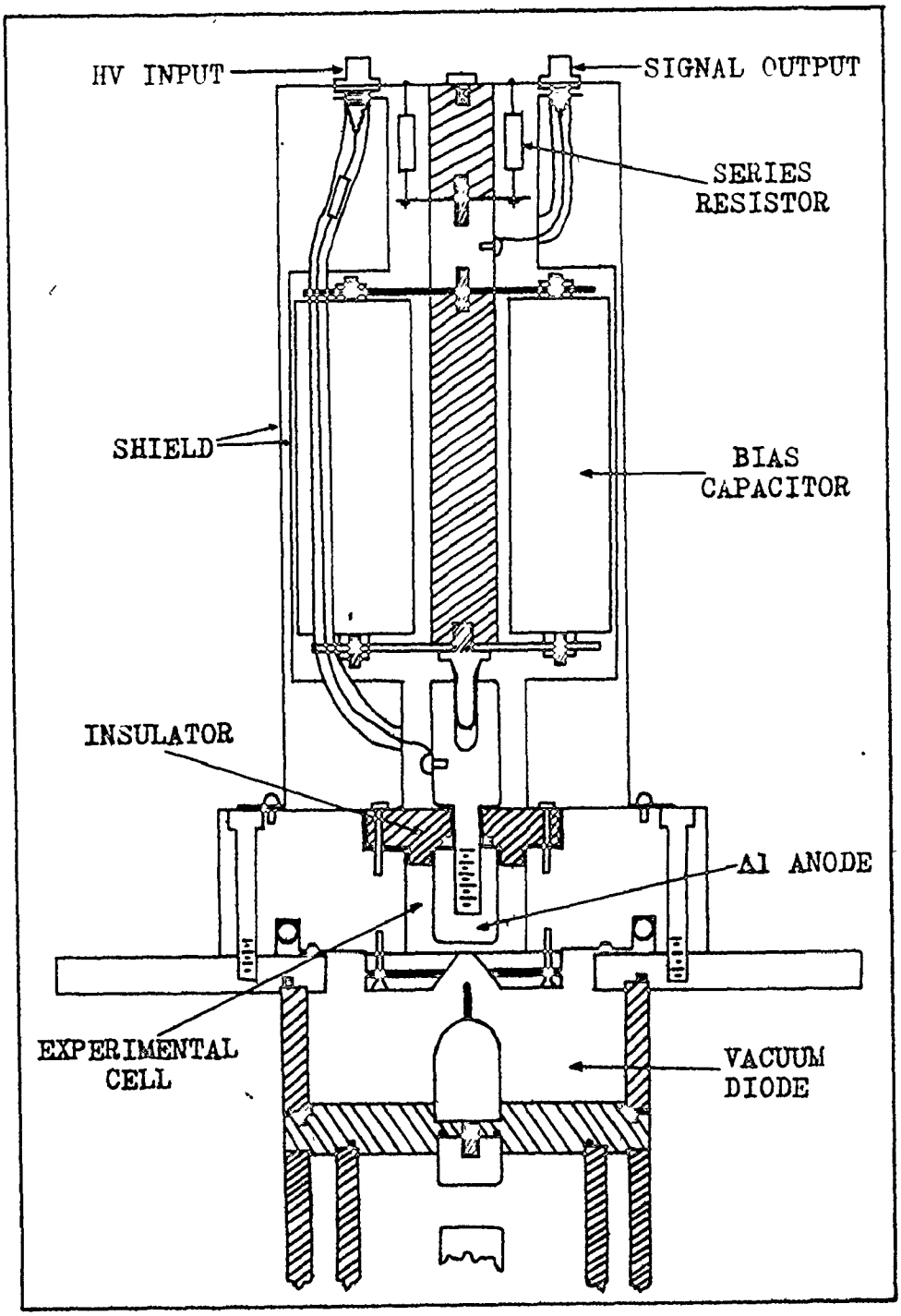
HV INPUT
SIGNAL OUTPUT
SERIES RESISTOR
SHIELD
BIAS CAPACITOR
INSULATOR
Al ANODE
EXPERIMENTAL CELL
VACUUM DIODE

2.2.1 The High Pressure Chamber

The high pressure chamber is a sealed enclosure with total volume of ~ 36 ml, an effective discharge volume of ~ 0.2 ml, a total wall surface area of ~ 110 cm^2, and is capable of withstanding a differential pressure of at least 600 KPa. The cell and electrodes are aluminum and the insulator is plexiglass. This material has been chosen as the insulator because of its low cost, because of its transparency (which allows inspection of the electrodes without exposing the cell to air), and also because of its slow reaction rate with HCl. The major problem with plexiglass is the high outgassing rate. Dayton [9] expresses the outgassing rate for plexiglass as

$$\text{Rate} = (1.33 \times 10^{-4}\ T^{-0.5})\ \text{Pa.l.s}^{-1}\text{.cm}^{-2}, \qquad (2.2\text{-}1)$$

where T is the pumping time in hours (> 1 hour). This expression has been derived from experimental data representing the best outgassing conditions for plexiglass. The principal gases evolved are water vapour, N_2 and O_2. However, H_2, CO and CO_2 may also be observed [29]. Since H_2O is released by the walls, the cell should be thoroughly outgasses before HCl is injected. This precautionary measure has been found to eliminate any visually-detectable corrosion damage to either the electrodes or the aluminum wall surfaces. The

normal thin layer of Al_2O_3 provides protection to the surface, and prevents adsorption of HCl to the walls. This has been verified by measurement of the dissociative attachment rate constant, as described later in the thesis, after leaving the Ar-HCl (2.8% HCl) mixture in the cell for periods of time varying from ~ 1 min to ~ 1 hour. No systematic change in the measured rate constant was observed in these measurements. However, as a precaution the cell was always vented and re-filled before each shot, which occurred within a few minutes of refilling.

The chamber was mechanically pumped to ~ 2 Pa. The mechanical pump was connected in series with a liquid nitrogen trap in order to prevent contamination of the chamber by vacuum pump oil, and to collect HCl during evacuation. The "leak rate", which was due mainly to plexiglass outgassing, was 1.5 Pa/min after > 48 hr of pumping. This can be compared with the 48 hr value of 0.78 Pa/min calculated using Eq. (2.2-1) and an exposed plexiglass surface area of 24.4 cm^2. The calculated rate is 0.38 Pa/min for T = 200 hr. The large outgassing rate of plexiglass can be eliminated, if necessary, by the use of a teflon insulator. However, this would result in the loss of the transparency required for viewing the electrodes.

Cell pressure measurements were made with a Matheson 0-400 KPa gauge, which was checked to be properly calibrated,

and for which the reading was found to be reproducible to within ± 5 KPa.

2.2.2 The Discharge Circuit

The discharge gap potential difference was maintained by means of four 0.25 μF capacitors, capable of holding off 7.5 KV dc. The capacitor bank was charged through a 1 MΩ resistor, in series with a high voltage power supply (up to 3.1 KV). The current pulse was measured from a low-inductance 1.25 - Ω resistor consisting of eight 10 - Ω resistors in parallel.

A schematic of the discharge circuit is shown in Fig. 2-15a. Figures 2-15b and c are simplified representations of Fig. 2-15a circuit for purposes of analysis.

Solution of the appropriate differential equations for circuit (b) gives the voltage drop across the series resistor R as

$$V_R(t) = \frac{e^{-\lambda t}}{C_g} \int_o^t \exp(\lambda z) I_g(z)\, dz, \qquad (2.2\text{-}2)$$

where $I_g(t)$ is the gap current, $\lambda = (RC_g)^{-1} + (RC_1)^{-1}$, C_1 is the bias capacitance, and C_g is the gap capacitance. The initial conditions are $V_{C_1}(o) = V_g(o) = V_o$. During a dissociative attachment run, the current pulse decays nearly exponentially in time (typical time constant τ = 50 ns).

Fig. 2-15 Schematic diagram of the discharge circuit.
a) entire circuit. b) simplified circuit.
c) simplified circuit.

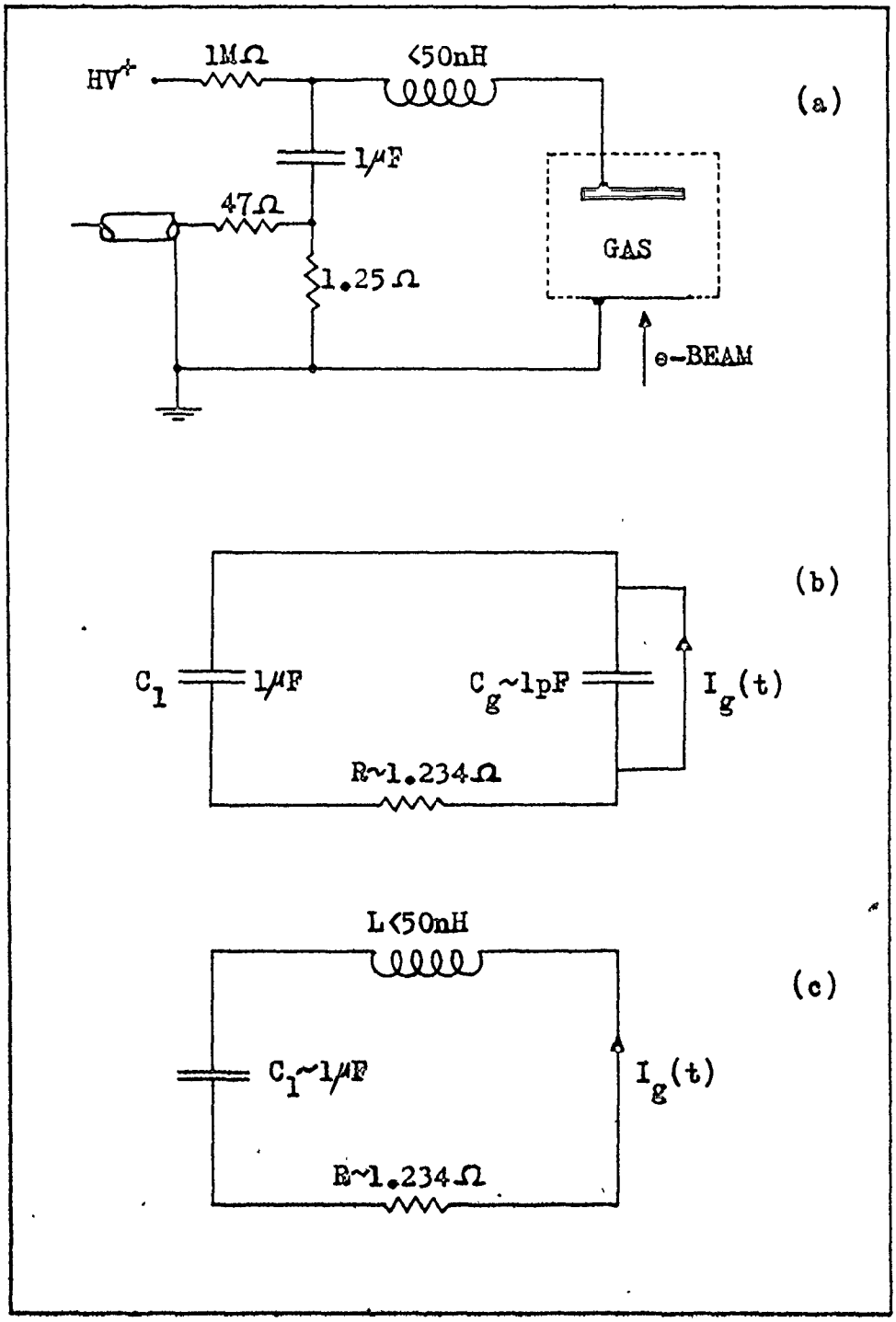
HV+
1MΩ
<50nH
(a)
1μF
47Ω
1.25Ω
GAS
e-BEAM
(b)
C1
1μF
Cg~1pF
Ig(t)
R~1.234Ω
L<50nH
(c)
C1~1μF
Ig(t)
R~1.234Ω

Writing

$$I_g(z) = I_o \exp - \frac{z}{\tau} \qquad (2.2\text{-}3)$$

we get

$$V_R(t) = I_o (\exp -\frac{t}{\tau} - \exp -\lambda t)/(C_g(\lambda - \tau^{-1})) \qquad (2.2\text{-}4)$$

since the actual experimental parameters were $C_1 \simeq 1\mu F$, $C_g \simeq 1pF$, $R = 1.25\ \Omega$, we get, for $\tau = 50$ ns,

$$\lambda^{-1} \simeq RC_g << \tau \qquad (2.2\text{-}5)$$

Clearly, only the first exponential term appearing in Eq. (2.2-4) is important. Therefore, Eq. (2.2-4) can be simplified to

$$V_R(t) \simeq RI_g(t), \quad \text{for } t > 20\lambda \simeq 25 \text{ ps}. \qquad (2.2\text{-}6)$$

It follows that equating the gap capacitance to zero, does not introduce any significant error in the calculated response of the circuit.

It is of interest to estimate the bias capacitor voltage drop ΔV_{C_1} for the experimental conditions.

$$\Delta V_{C_1} = \frac{1}{C} \int_o^\infty I_g(t)dt \qquad (2.2\text{-}7a)$$

When $I_g(t)$ has the exponential form given by Eq. (2.2-3),

ΔV_{C_1} is

$$\Delta V_{C_1} = I_o \tau / C_1 \qquad (2.2\text{-}7b)$$

In the worst case τ = 500 ns, I_o = 15 A and $V_{C_1}(0)$ = 1000V.

This gives ΔV_{C_1} = 7.5 volts and $\Delta V_{C_1}(0) \times 100$ = 0.75%.

Under typical conditions τ = 50 ns, $I_o = V_{C_1}(0)$ = 2000V.

We then get ΔV_{C_1} = 0.25V and $(\Delta V_{C_1}/V_{C_1}(0)) \times 100$ = 0.0125%.

These results clearly show that the measured current variations are due to changes in the plasma conductivity, rather than being caused by the discharge of the bias capacitor.

The previous results lead us to consider the circuit shown in Fig. 2-15c as being a more adequate simplified representation of the discharge circuit. In this case, we are interested only in the temporal evolution of the gap voltage $V_g(t)$, given by

$$V_g(t) = V_o - \frac{1}{C_1} \int_o^t I_g(t)dt - RI_g - \frac{LdI_g}{dt}, \qquad (2.2\text{-}8)$$

The circuit inductance L is $\leq$ 50 nH. The experimentally observed current pulse can be approximated by

$$I_g(t) = \begin{cases} I_o t/10 & 0 < t < 10 \text{ ns} \\ I_o & 10 \text{ ns} < t < 13.\text{ns} \\ I_o \exp - (\frac{t-13}{\tau}) & t > 14 \text{ ns} \end{cases} \qquad (2.2\text{-}9)$$

Figure 2-16 shows $(V_g(t)-V_o)/V_o$ calculated using Eqs. (2.2-8) and (2.2-9) for typical values of I_o, τ and V_o. We find that $|\Delta V_g|/V_o$ is always less than 0.4% for time $t > 15$ ns. Since no measurable changes in the dissociative attachment rate should be observed for such small fluctuations of the gap voltage, we have used $V_g \approx V_o$.

A reasonably uniform-field electrode configuration was employed. The anode electrode had a composite three dimensional Chang profile [30], and was made from of a 2.54 - cm aluminum rod. This was machined on a lathe, rough-polished with #600 emery paper, and finally polished with Brasso. The cathode was the thin aluminum foil (26 μm Reynold's wrap) separating the high pressure chamber from the vacuum diode. The cathode diameter was 4.5 cm and the gap spacing was 0.6 cm. The foil was supported by means of a nickel mesh of ~ 55% transparency from circular holes of 0.3 mm diameter. The use of such a support prevented the foil from breaking at high differential pressures (~ 400 KPa), and helped to maintain a flat cathode. Inside a central region of ~ 1.5 - cm diameter, the main source of field distortion was caused by the irregularity of the cathode. Outside this region the irregularity was caused by the edge effects due to the finite anode size.

The bias capacitors, the high voltage lead and the series resistor were carefully shielded, as shown in Fig. 2-17. This precaution reduced the peak-to-peak rf

Fig. 2-16 Fractional changes of the discharge gap voltage as a function of time. The peak current (I_o) was in each case 5 A and the applied voltage (V_o) $\sim$ 1500 V. The dashed curve corresponds to τ= 40 ns, and the full curve to τ = 200 ns.

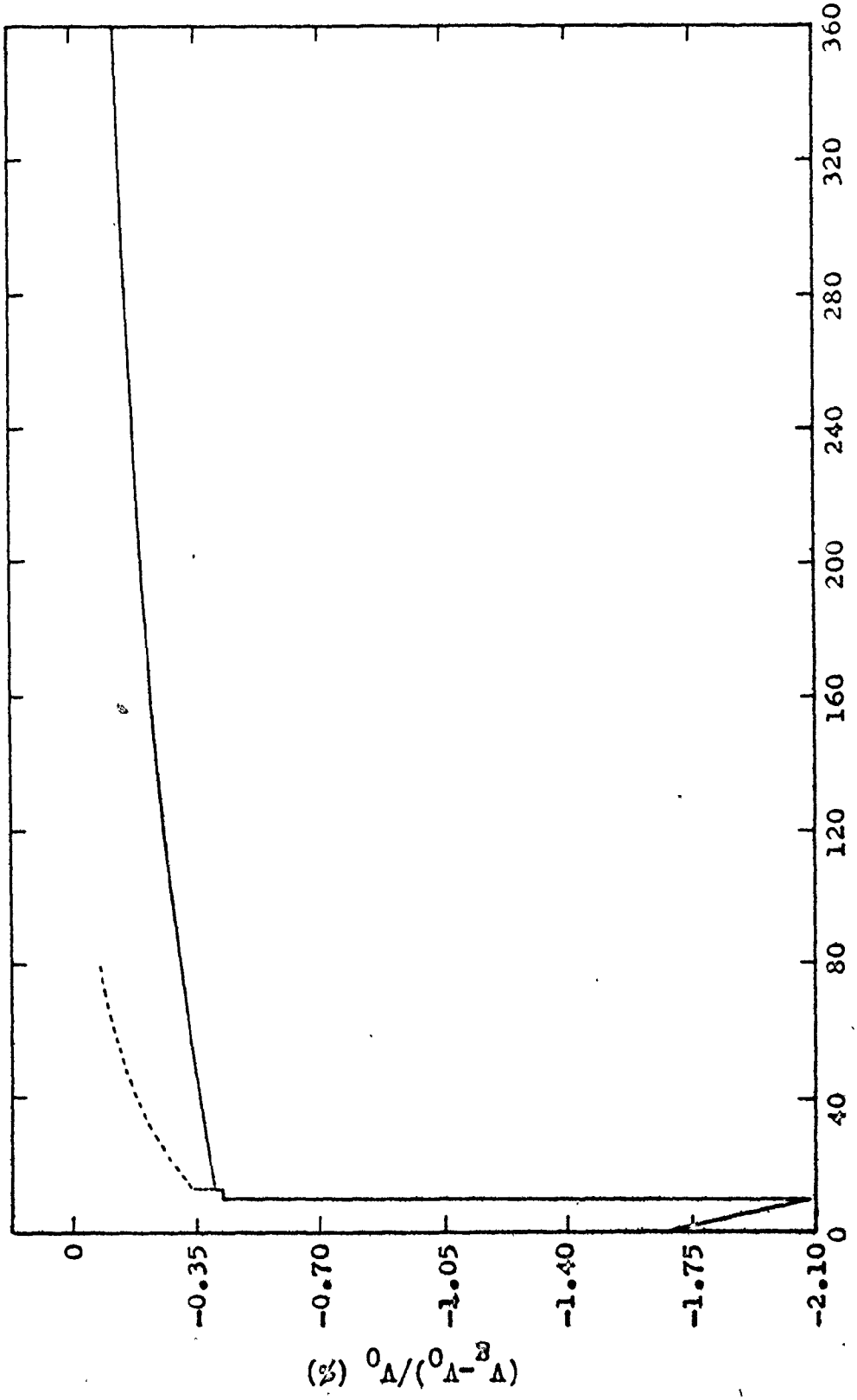
0
-0.35
-0.70
-1.05
-1.40
-1.75
-2.10
(%) $(V_E-V_0)/V_0$
0
40
80
120
160
200
240
280
320
360
TIME (ns)

noise amplitude by approximately a factor of 10, in comparison to the case where only the e-beam gun was shielded and a single braided return current conductor used. Figure 2-17 shows typical current pulses observed in nitrogen, both with and without the shield.

2.2.3 Gas Mixtures

Nitrogen (Matheson 99.99% pure), Argon (Matheson, 99.995% pure), and an Ar-HCl mixture (2.8 ± 0.06% HCl, analyzed by Matheson's) were used without further purification. The gas mixtures which consisted typically of 55 - 400 Kpa of Ar-HCl (2.8% HCl) plus 0-345 Kpa of Ar or N_2 were prepared in a previously passivated 250 ml pyrex bulb.

Fig. 2-17 Oscilloscope records showing typical current pulses observed in nitrogen. a) The bias circuit was shielded. b) The shield was replaced with a single braided wire (1 cm wide).

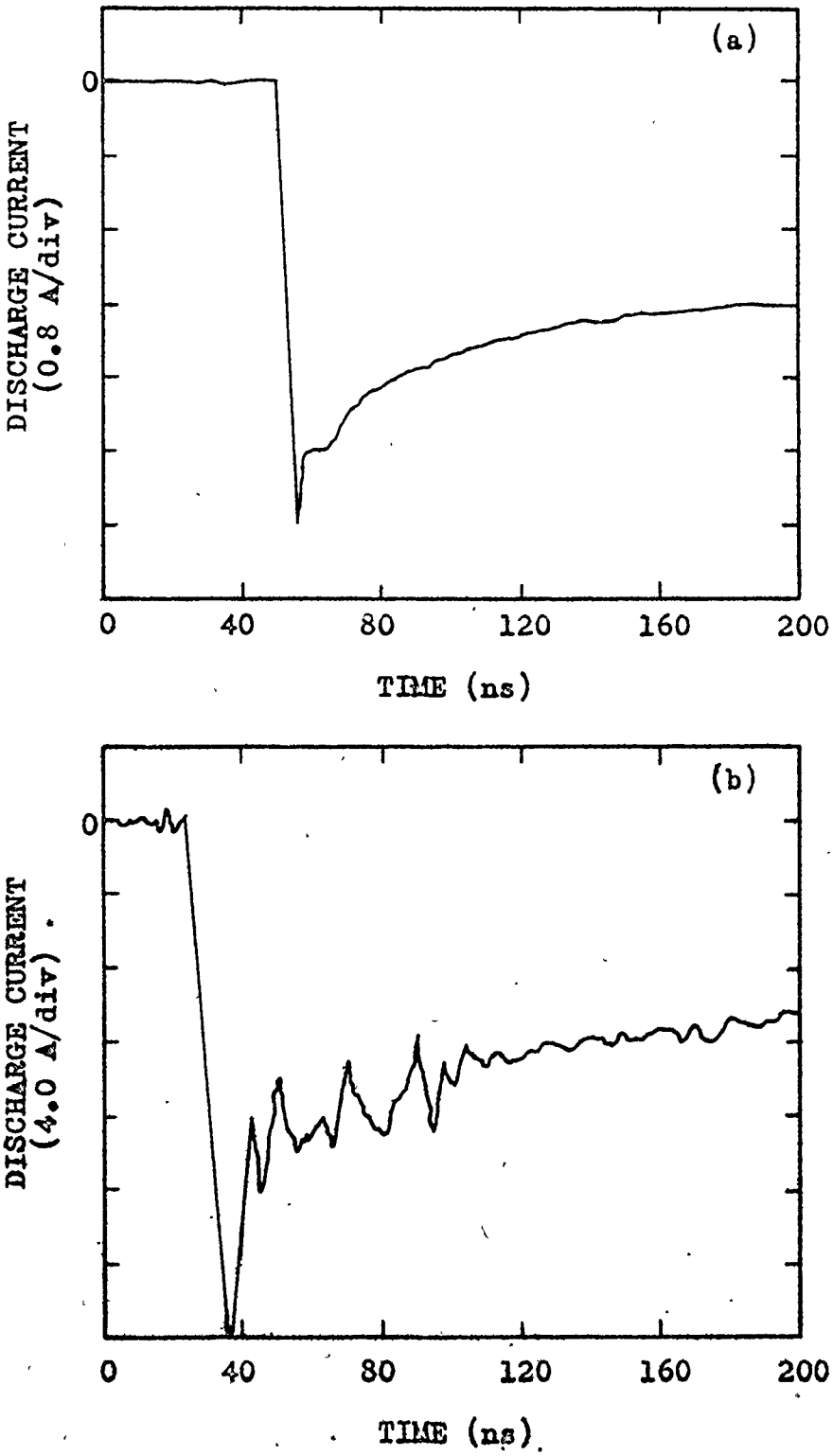
(a)
0
DISCHARGE CURRENT
(0.8 A/div)
0
40
80
120
160
200
TIME (ns)
(b)
0
DISCHARGE CURRENT
(4.0 A/div)
0
40
80
120
160
200
TIME (ns)

CHAPTER 3

THE DISCHARGE PLASMA

3.1.1 Creation of the Plasma

In the first section of this chapter we provide a rough estimate of the bulk characteristics (initial secondary electron number density, and diffusion characteristic time) of the discharge plasma column.

The secondary-electron production rate P_s (at the output of the aluminum foil window) is given by [19]

$$P_s \approx J_{eb}\rho S/((eE_i)(\cos\theta)_{avg}) \quad , \tag{3.1-1}$$

where S is the mean stopping-power of the gas ($eV\cdot cm^2/g$), J_{eb} is the primary electron-beam current density (A/cm^2), E_i is the effective ionization energy required for the formation of an electron-ion pair (eV), ρ is the mass density of the gas ($g\cdot cm^{-3}$), and

$$(\cos\theta)_{avg} = \int_0^{\pi/2} \cos\theta \sin\theta f_{GS}(\theta)d\theta \Big/ \int^{\pi/2} \sin\theta f_{GS}(\theta)\, d\theta \tag{3.1-2}$$

is a correction term allowing for the angular distribution of

the electron velocity (f_{GS} is the Goudsmit-Saunderson distribution [20]).

We have shown in Section (2.1.3) that, for small angles, $f_{GS}(\theta) \approx 2\exp-(\theta^2/\chi_c^2$ (B-1.2)). Using this approximative expression for the angular distribution function, numerical integration yields $(\cos\theta)_{avg} \approx 0.6004$ (using χ_c^2(B-1.2) ≈ 1.945, as found for typical conditions in Section (2.1.3)).

The stopping-power for 90 KeV electrons in Argon is $\sim 2.9 \times 10^6 \frac{eV \cdot cm^2}{g}$ and in Nitrogen is $\sim 3.7 \times 10^6 \frac{eV \cdot cm^2}{g}$ [31]. The effective ionization energies are 27 and 33 eV for Ar and N_2, respectively [31]. At a gas number density of $\sim 2.5 \times 10^{19}$ cm^{-3} and an electron beam current density of $\sim 2A/cm^2$, the secondary electron production rate (just beyind the aluminum foil window) is $\sim 3.7 \times 10^{21}$ $cm^{-3}.s^{-1}$ in Ar and $\sim 2.7 \times 10^{21}$ $cm^{-3}.s^{-1}$ in N2. If we assume that the current pulse is tringular (isoscele) with a FWHM of $\sim$ 10 ns, and that the electron energy is constant during the electron beam current pulse, then the "initial" secondary-electron number density is calculated to be $\sim 3.7 \times 10^{13}$ cm^{-3} in Ar and $\sim 2.7 \times 10^{13}$ cm^{-3} in N_2 (at 100 KPa).

Equation (3.1-1), together with the appropriate expressions for J_{eb} and $(\cos\theta)_{avg}$, can be used to determine the secondary-electron production rate anywhere in the plasma.

As they cross the discharge gap, the primary electrons

suffer collisions with the atoms (molecules) of the gas. The scattering produced results in a diffusive increase in the angular spread of the e-beam. The 1/e width of the angular distribution, starting from an initially parallel 65-KeV electron-beam passing through a 6 mm thick argon target at 100 KPa, is estimated to be ~ 0.58 rad ($\theta_{1/e} \simeq \chi_c (B-1.2)^{1/2}$, as given in Section 2.1.3). As the primary electrons travel through the gas they also suffer inelastic collisions with atoms (molecules), and lose a fraction of their kinetic energy. Each electron typically loses 3.5 KeV·cm^{-1} in N_2 and 4.5 KeV·cm^{-1} in Ar [31] (at a pressure of ~ 100 KPa). This energy loss is approximately balanced by the energy gain from the accelerating discharge field (typically 3.5 KeV·cm^{-1}). Both effects (scattering of electrons by the gas and electron energy loss) are less important for determining the expressions for J_{eb} and $(\cos\theta)_{avg}$), than the angular spread caused by the multiple scattering of the electrons in the foil. These effects have been completely neglected in the present calculations in order to keep the solution simple.

In the actual case we assume that the primary electron beam has cylindrical symmetry. Therefore, $J_{eb}(z)$ and $(\cos\theta)_{avg}(z)$, at a distance z from the foil and along the symmetry axis, are given by

$$J_{eb}(z) \propto \int_0^R 2\pi r \, dr \, f_{GS}(\theta(r,z)) z (r^2+z^2)^{-3/2} dr \qquad (3.1\text{-}3a)$$

and

$$(\cos\theta)_{avg}(z) = \int_0^{\theta max} f_{GS}(\theta)\ \sin\theta\ \cos\theta\ d\theta \Big/ \int_0^{\theta max} f_{GS}(\theta)\ \sin\theta\ d\theta, \qquad (3.1\text{-}4a)$$

where R is the radius of the aluminum foil window and $\theta_{max} = \tan^{-1}(z^{-1}R)$. These integrals must be solved numerically. However, for $z > R$ the use of the approximations $f_{GS}(\theta) \approx 2\ \exp-(\theta^2/\chi_c^2(B-1.2)))$ and $\sin^2\theta \approx \theta^2$ may be used, to yield the following approximative expressions:

$$J_{eb}(z) \alpha z(\exp-\sigma^{-1}(z^{-1}(z^{-1}-(z^2+R^2)^{-1/2}) + (z^{-1}\sum_{n=0}^{\infty}(\frac{2n+1}{n!})\ \sigma^{-n}) - (z^2+R^2)^{-1/2}$$

$$(\sum_{n=0}^{\infty}(\frac{2n+1}{n!})\ (z^2\sigma^{-1}/(z^2+R^2))^n)), \qquad (3.1\text{-}3b)$$

and

$$(\cos\theta)_{avg}(z) = \frac{\sigma}{2}\ (1-\exp-(R^2\sigma^{-1}/(R^2+Z^2)))/((1-\sigma^{-1})$$

$$(1-z/(R^2+z^2)^{1/2}) + (\sigma^{-1/3})(1-z^3/(R^2+z^2)^{3/2})). \qquad (3.1.4b)$$

In the case of a highly diffuse distribution function ($f_{GS}(\theta) = 1$, $\sigma \to \infty$ the solutions are

$$J_{eb}(z) \approx J_o(1-z/(z^2+R^2)^{1/2}) \tag{3.1-5}$$

and

$$\cos\theta_{avg} = J_o R^2/(2J_{eb}(z)(R^2+z^2)), \tag{3.1-6}$$

where J_o is the current density at the center of the foil. Therefore, the secondary-electron production rate is given by

$$P_s(z) = 2\rho S\, J_{eb}^2(z)\, \frac{(R^2+z^2)}{J_o R^2} \tag{3.1-7}$$

It is also of interest to know the radial dependence of P_s. For $z>>R$ an approximation of the functional dependence is given by

$$P_s(z,r) \alpha\ f(\theta_{cen})/R_{avg}^2, \tag{3.1-8}$$

An analytic solution for R_{avg}^{-2} has not been found. However, we have determined a lower and upper bound for its value, which is given by

$$(r^2+z^2+R^2)^{-1} < R_{avg}^{-2} < (\tan^{-1}(z-r) - \tan^{-1}(-z-r))/(2Rz) \tag{3.1-9}$$

Figure 3-1a shows a plot of the secondary-electron production rate $P_s(z)$ calculated by combining Eqs. (3.1-1), (3.1-3b) and (3.1-4b), together with the rate given by Eq. (3.1-7) (both results have been arbitrarily normalized to $P_s(0.6\ \text{cm})=1$). Figure 3-1b shows a plot of $P_s(0.6,r)_{max}$, $P_s(0.6,r)_{min}$, $P_s(0.3,r)_{max}$ and $P_s(0.3,r)_{min}$ obtained from Eqs. (3.1-8) and (3.1-9). We can now consider the diffusion problem. The spatial and temporal evolution of the electron number-density is determined, in the case of a simple diffusion process, by

$$\frac{\partial n}{\partial t} = D\nabla^2 n, \qquad (3.1\text{-}10)$$

where D is the diffusion coefficient and n is the electron number-density).

If the medium through which the electrons diffuse is infinite (no boundary conditions), then the electron number-density is given by [2]

$$n(x,y,z,t) = \frac{1}{8(\pi Dt)^{3/2}} \int [n(x',y',z',o) \times \exp - \frac{(x-x')^2+(y-y')^2+(z-z')^2}{4Dt} dV'] . \qquad (3.1\text{-}11)$$

We have shown in this section that n(x,y,z,o) is approximately known. Therefore n(x,y,z,t) can, in principle, be determined for all other times.

Fig. 3-1 a) Secondary-electron production rate as a function of the distance to the foil (2) along the symmetry axis of the plasma. The dashed curve was plotted using Eq. (3.1-7). The rate function determined using Eqs. (3.1-1), (3.1-3b) and (3.1-4b) as represented by the full curve. b) Secondary-electron production rate as a function of the radial distance. The rate function was plotted for z=0.3 cm (dashed curves) and z=0.6 cm (full curves). In both cases the lower curve corresponds to the values calculated with R_{min}^{-2} Eq. (3.1-9).

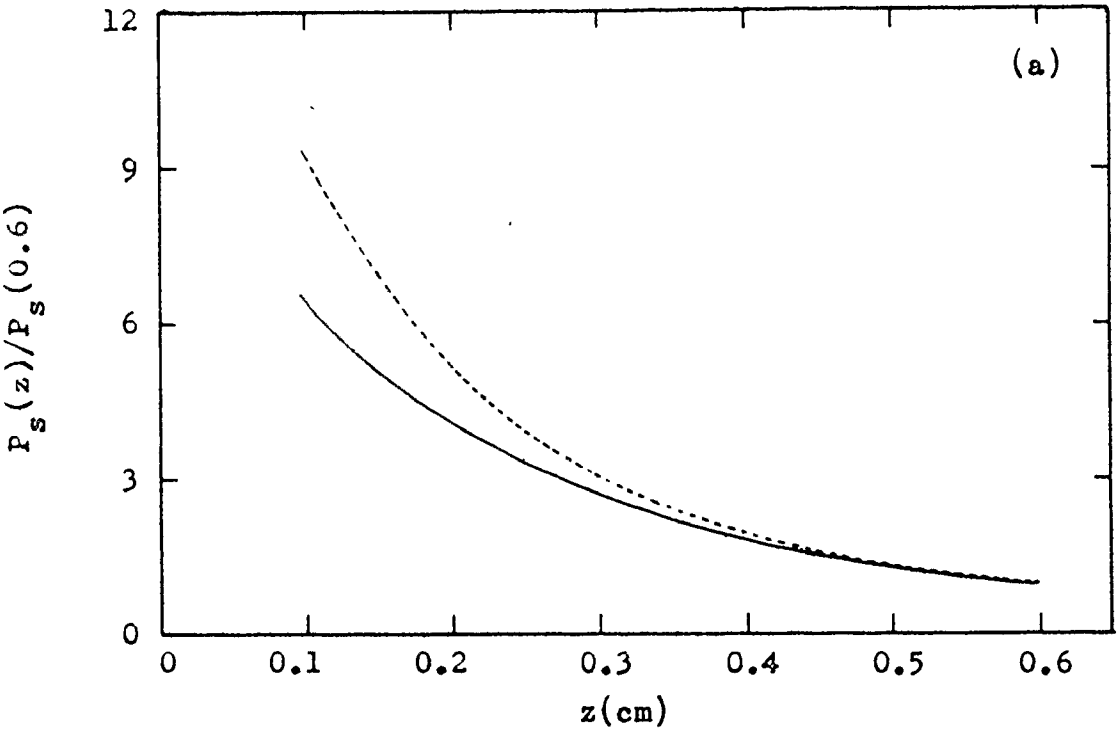
(a)
12
9
6
3
0
0
0.1
0.2
0.3
0.4
0.5
0.6
z(cm)
$P_s(z)/P_s(0.6)$

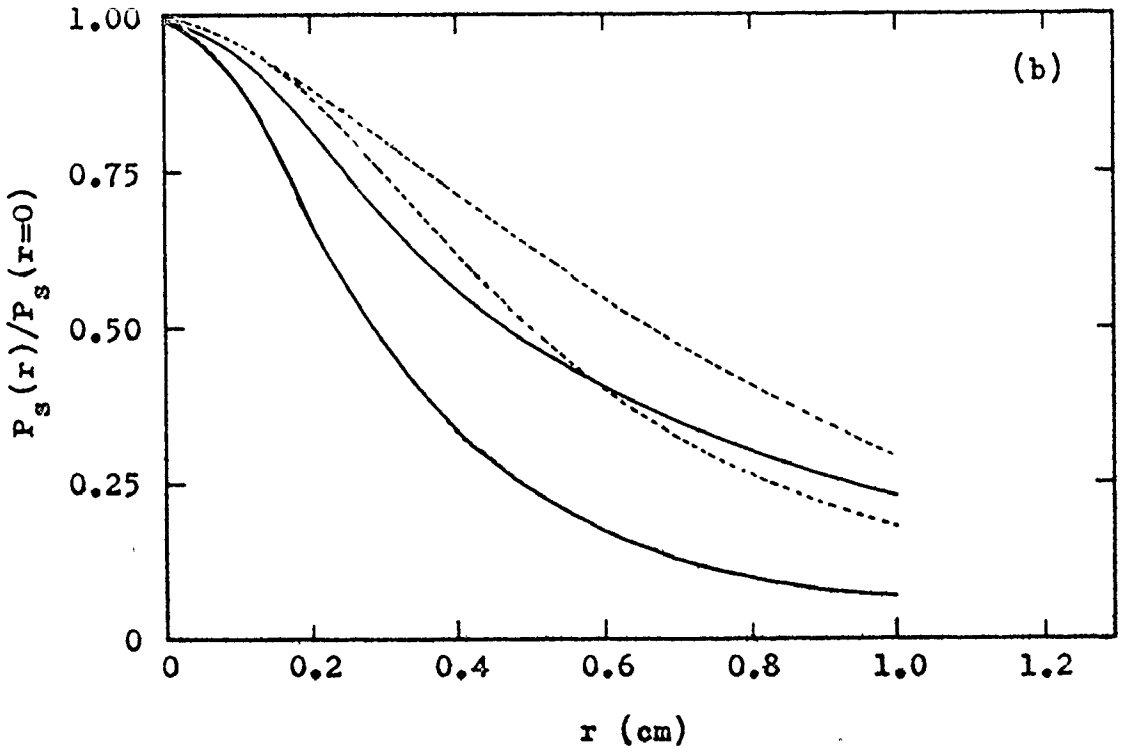
(b)
1.00
0.75
0.50
0.25
0
0
0.2
0.4
0.6
0.8
1.0
1.2
r (cm)
$P_s(r)/P_s(r=0)$

However, it is not essential to solve this problem explicitly in order to obtain useful information about the evolution of the electron density. We consider instead the initial electron density

$$n_o(z,y,z,o) = n_o\delta(x)\delta(y) \tag{3.1-12}$$

Substitution of Eq. (3.1-12) in Eq. (3.1-11) yields

$$n(x,y,z,t) = \frac{n_o}{4\pi Dt} \exp-\frac{r^2}{4Dt} . \tag{3.1-13}$$

The 1/e width of this distribution is given by

$$r_{1/e} = (4Dt)^{1/2} \tag{3.1-14}$$

In the present case the coefficient of diffusion D is typically ~ 6 x 10^{-6} $cm^2 ns^{-1}$. Therefore, the expansion velocity is

$$V_{1/e} = \frac{dr_{1/e}}{dt} \approx \frac{1.2 \times 10^{-5}}{r_{1/e}} \text{ cm}\cdot\text{ns}^{-1}, \tag{3.1-15}$$

with $r_{1/e}$ in cm.

At a 1/e radius ~ 0.3 cm, $v_{1/e}$ is ~ 4 x 10^{-5} cm/ns. This clearly shows that over the time scale of interest

3.1.2 Electron Energy Distribution

A general model of the gas discharge can, in principle, be built by solving the Boltzmann equation for the distribution function $f_s(\underset{\sim}{v},\underset{\sim}{x},t)$ using the appropriate boundary conditions for each species S (neutral and excited atoms, and molecules, ions, and electrons). The pertinent set of equations have the form

$$\frac{\partial f_s}{\partial t} + \nabla_{\underset{\sim}{v}} \cdot f_s + \nabla_v \cdot \frac{f_s}{M_s} \underset{\sim}{F}_s = \sum_r \mathbf{C}_{sr}, \qquad (3.1\text{-}1b)$$

where $\mathbf{C}_{sr}$ represents the net rate of increase of the class in question as a result of collisions between particles of species s with those of species r, $\underset{\sim}{F}_s/M_s$ is the acceleration of particles of species s of a given class resulting from external forces $\underset{\sim}{F}_s$, and $f_s(\underset{\sim}{v}, \underset{\sim}{x}, t)\,d^3v\,d^3x$ is the number of particle of species s in a volume element d^3v at v in velocity space, and in a volume element d^3x at x in space. This approach was found to be far too complicated. The chosen alternative consisted in considering the homogeneous steady-state Boltzmann equation for electrons alone. Several authors have given methods for solving this problem in some special cases [33-38].

A Boltzmann code has been written based on Sherman's [36] method of solution. In this case the Boltzmann equation is reduced to

$$\nabla_v \cdot \frac{E}{M_e} \underset{\sim}{f}_e = \sum_r C_{er}^{(elastic)} + C_{er}^{(inelastic)} \qquad (3.1\text{-}17)$$

where $C_{er}^{elastic}$ and $C_{er}^{inelastic}$ stand for the elastic and inelastic collision of particles of type e with those of type r, respectively.

Holstein [35] has shown that, provided the electron mean-free-path for elastic collisions is short compared to the linear dimension of the volume occupied by the gas, the large deflections resulting from elastic collisions with atoms (or molecules) lead to a nearly isotropic electron-velocity distribution function. The linear dimensions of the present plasma column are ~ 0.6 cm, and the mean-free-path for electrons, at 100 KPa in Ar, is ~ 5×10^{-5} cm. Since the conditions were appropriate, we employed Holstein's [35] two term cartesian tensor expansion of the electron-velocity distribution

$$f_e(v) = f_o(v) + \underset{\sim}{f}_1(v) \cdot \underset{\sim}{v}/v, \qquad (3.1\text{-}18)$$

where $|\underset{\sim}{f}_1| << f_o$.

Detailed development of the Boltzmann equation for f_o and $\underset{\sim}{f}_1$, with explicit expressions for the collisional terms, is found in standard text books [39, 40]. Therefore, only the final results are given here. The time-independent Boltzmann equation for the isotropic part, $f_o(v)$, of the

nearly isotropic electron-energy distribution for a mixture of gases (in the case where only the elastic and inelastic collisional processes are considered) is given by [40]

$$f_o(u) = \exp\left(\left(-\int_o^u 2A^{-1}(u) M_e u^2 \sum_K \frac{\delta_K Q_m^K(u)}{M_K}\right) - \frac{A^{-1}(u)}{f_o(u)} \times\right.$$

$$\left.\left(\sum_j \sum_k \int_o^{u_{jK}} du((u+u')\delta_K Q_j^K(u+u') f_o(u+u'))\right)\right), \qquad (3.1\text{-}19)$$

$$\text{where } A(u) = \frac{1}{3}(E/N)^2 \, u\left(\sum_K \delta_K \, Q_m^K\right)^{-1}$$

and where the arbitrary normalization factor $f_o(o) = 1$ has been used. Here $u = mv^2/2e$ is the electron energy in volts, $Q_m^K(u)$ is the momentum transfer cross section for the K^{th} species, Q_j^K is the inelastic cross-section for the K^{th} species in the j^{th} excited state, N is the total (atoms plus molecules) number density, E is the applied electric field, M_K is the mass of a particle of species K, a_{jK} is the excitation energy of the j^{th} level for the K^{th} species, and δ_K is the mole fraction of particle of species K.

Sherman [36] has proven that Eq. (3.1-19) can be solved by iteration. A Boltzmann code employing is iterative method of solution was written. However in the present case the iteration was started by setting $f_o^{(o)}(u) = 0$, $0 < u < u_{max}$, rather than by using $f_o^{(o)}(u) = 1$ as done

by Sherman [36] (note that the subscript (n) in $f_o^{(n)}(u)$ represents the $(n+1)^{th}$ iteration, and that u_{max} was chosen so that $f_o(o)/f_o(u_{max}) > 10^8$). In the range of E/N (reduced electric field) employed, starting the iteration with $f_o^{(o)}(u)=1$ invariably lead to $f_o^{(1)}(u)$ = "floating zero". However, starting with $f_o^{(o)}=0$ give a solution and also provided the useful relationship

$$f_o^{(o)}(u) < f_o^{(2)}(u) < f_o^{(4)}(u) \ldots < f_o^{(2n)}(u)$$

$$< f_o^{(2n+1)}(u) < f_o^{(2n-1)}(u) \ldots < f_o^{(1)}(u) \quad (3.1\text{-}20)$$

We used the above "two-sided" convergence property to reduce the number of iterations and consequently to shorten the computation time. For this, $f_o^{(n+1)}(u)$ in the $(n+2)^{th}$ iteration was replaced by $f_o^{(n+1)}(u) = (f_o^{(n+1)}(u)\, f_o^{(n)}(u))^{1/2}$ (the geometric average of $f_o^{(n)}(u)$ and $f_o^{(n+1)}(u)$). This method was found to be very efficient in reducing the total number of iterations required for a good convergence of the electron-energy distribution-function.

The distribution-function was then used to calculate the electron drift velocity v_d, the electrons characteristic energy ε_k, the average electron energy ε_{avg}, and the rate constant (R) of reactions involving electrons as primary particles. The relations used to calculate these parameters are [40]:

$$v_d = \frac{-E}{3N}\left(\frac{2e}{M_e}\right)^{1/2} \int_0^\infty \frac{u}{\left(\sum_K \delta_K Q_m^K\right)} \frac{\partial f_o}{\partial u}\, du \Big/ \int_0^\infty u^{1/2} f_o(u)\, du \qquad (3.1\text{-}21a)$$

$$\varepsilon_K = -\int_0^\infty \frac{u f_o(u)}{\sum_K \delta_K Q_m^K(u)}\, du \Big/ \int_0^\infty \frac{u}{\left(\sum_K \delta_K Q_m^K(u)\right)} \frac{\partial f_o}{\partial u}\, du \qquad (3.1\text{-}21b)$$

$$\varepsilon_{avg} = \int_0^\infty u^{3/2} f_o(u)\, du \Big/ \int_0^\infty u^{1/2} f_o(u)\, du, \qquad (3.1\text{-}21c)$$

and $$R = \left(\frac{2e}{M_e}\right)^{1/2} \int_0^\infty Q_R(u) u f_o(u)\, du \Big/ \int_0^\infty u^{1/2} f_o(u)\, du, \qquad (3.1\text{-}21d)$$

where $Q_R(u)$ is the cross section for the reaction R.

The Boltzmann equation employed did not account for super elastic collisions or for electron-electron (e-e) interaction terms. The error introduced by neglecting the superelastic term is not important because the ratio of the number of atoms in any excited state to the number in the ground state is expected to be small during the discharge. Postma [37] has given a simple expression for the electron concentration at which the influence of e-e collisions becomes important. This is

$$\frac{N_e}{N} = \frac{4\pi\varepsilon_o^2}{e^2 \ln\Lambda} \left(\sum_K \delta_K Q_m^K\right)^{-1} (E/N)^2, \qquad (3.1\text{-}22a)$$

where ε_o is the permittivity of free space,

$\ln\Lambda = 12\pi N_e^{-1/2} \left(\frac{\varepsilon_o KT_e}{N_2^2}\right)^{3/2}$, T_e the electron temperature, and K the Boltzmann constant. All the other symbols have been previously defined in this section.

For Argon the numerical value of Eq. (3.1-22a) is

$$\frac{N_e}{N} = 4.7 \times 10^{34} \left(\frac{E}{N}\right)^2, \qquad (3.1\text{-}22b)$$

where E/N is $V.m^2$. The range of E/N employed experimentally extended from $0.2 \times 10^{-20} V.m^2$ to $10^{-20}\ V.m^2$. The lowest E/N values were obtained by setting the buffer gas pressure to approximately 400 KPa ($N \sim 10^{26} m^{-3}$), so that the critical electron number density is $\sim 2 \times 10^{13} cm^{-3}$. At large values of the reduced field, $E/N > 0.5 \times 10^{-20} V.m^2$, the critical electron number-density is $> 5 \times 10^{13} cm^{-3}$. In order to avoid any theoretical complication the electron beam current density was attenuated to $\sim$ 1-2 A/cm^2. Even though, at low $E/N \sim 0.2 \times 10^{-20} V.m^2$ (large pressure) the electron density at the foil can be initially as large as $(5\text{-}10) \times 10^{13} cm^{-3}$ and the computer code fail to give accurate result. However, for $E/N > 0.4 \times 10^{-20}\ V.m^2$ the electron density is low enough that the e-e interaction can be neglected.

The secondary electrons produced by the incident electron beam are distributed in energy (u) according to [41]

$$S(E,u) \quad \frac{A(E)\,\Gamma^2}{(u-T_o)^2+\Gamma^2}\,U\,(E-E_i-2u), \qquad (3.1\text{-}23)$$

where U is the Heavyside step function, $A(E)=\sigma_o K E^{-1}\ln(EJ^{-1})$,

$$T_o = T_s - 1.0 \times 10^3/(E+2E_i), \qquad \Gamma = \Gamma_s E/(E+\Gamma_b),$$

E_i is the ionization energy, $\sigma_o = 10^{-16}\,cm^2$, E is the primary electron energy, and K, J, T_s, Γ_s and Γ_b are 9.30, 3.75, 6.87, 6.92 and -7.85, respectively. From Eq. (3.1-23) the secondary-electron average energy have been calculated to be ~ 17.5 eV for an incident electron energy of ~ 80 KeV. After the electron-beam is turned off, this high-average electron energy distribution function relaxes toward the quasi-steady-state distribution function. An estimate of the relaxation time is obtained by calculating the elapsed time required for the electrons to lose their energy through collisions with the atoms (molecules) of the gas. In the case of an 99.5% Ar/0.5% HCl plasma and electron energies in the range 6-12 eV, the dominant cooling processes are elastic collisions with the atoms (molecules) and electron-electron interactions. The characteristic time (τ_a) for an electron to cool by collisions with atoms is

$$\tau_a = \frac{M_{Ar}}{2M_e}\,(N_{Ar} v_e Q_m^{Ar})^{-1}, \qquad (3.1\text{-}24)$$

and to cool by electron-electron collisions is [39]

$$\tau_e = (N_e \frac{8\sqrt{\pi}}{3} (\frac{M_e}{KT_e})^{3/2} (\frac{e^2}{4\pi\varepsilon_o M_e}) \ln \Lambda^{-1}. \qquad (3.1\text{-}25)$$

All symbols have been defined previously. Under typical conditions $N_{Ar} \sim 5 \times 10^{19} cm^{-3}$, $Q_m^{Ar} \sim 10^{-15} cm^2$, and $N_e \sim 10^{13} cm^{-3}$. Consequently, τ_a is ~3.0-5.5ns (for electron energies in the range 6-12 eV) and τ_e is ~ 65 ns (for 10 eV electrons). Above the excitation threshold, the electrons will lose energy by inelastic collisions, with a characteristic time

$$\tau_{ex} \sim (u/u_j^{Ar}) (N_{ar} v_e Q_j^{Ar})^{-1} , \qquad (3.1\text{-}26)$$

where u_j^{Ar} is the excitation energy of the j^{th} electronic level of argon, and Q_j^{Ar} the cross-section. Typically, $u_j^{Ar} \sim 13$ eV and $Q_j^{Ar} \sim 10^{-17} cm^2$, so that $\tau_{ex} \sim 8.5$ ps for $u \sim 15$ eV. For electron energies below ~6 eV, electrons lose energy by exciting vibrational levels of HCl with a characteristic time given by Eq. (3.1-26) (with $Q_j^{Ar} \rightarrow Q_i^{HCl}$ and $u_j^{Ar} \rightarrow u_i^{HCl}$). Typically, $N_{HCl} \sim 5 \times 10^{17} cm^{-3}$, $Q^{HCl} \sim 4 \times 10^{-16} cm^2$ and $u_j^{HCl} \sim 0.4$ eV, so that $\tau_{ex} \sim 0.5$ns (for 5eV electrons).

The electron energy distribution reaches its quasi-steady-state within ~10 ns (for an Ar-HCl plasma). At any later time the distribution function calculated by our Boltzmann code is a good approximation of the actual distribution. The relaxation time of an Ar-N_2-HCl plasma

is much shorter because of the large vibrational excitation cross-section in the energy range of ~6-12 eV.

Figures 3-2 to 3-8 show the calculated transport coefficients and rate constants obtained for typical Ar-HCl and Ar-N_2-HCl plasmas, the cross-sections and the numerical methods used for these calculations are given in Appendix 1.

The accuracy of the program was verified by comparing calculated values of drift velocity (v_d) and characteristics energy (ε_k) with experimental results for pure Ar and N_2. For E/N in the range 0.2×10^{-20} - 10^{-20} V·m^2, the calculated parameters for Ar are found to lie within the error limits of the experimental data. For N_2 the values differ by approximately 6% and 3% for ε_K and v_d, respectively. These errors may be due to the neglect of rotational excitations even at these E/N values.

Figures 3-6 and 3-8b show $k_{HCl;Cl^-}$ (the dissociative attachment rate constant) plotted against ε_{avg}. The result is rather insensitive to the exact shape of the electron energy distribution function. For purposes of comparison the figures show the same data calculated using ε_{avg} in the Maxwellian distribution function

$$f_{Maxwell}(U) = \left(\frac{3M_e}{4\pi\varepsilon_{avg}}\right)^{3/2} \exp-\left(\frac{3U}{2\varepsilon_{avg}}\right) \cdot \qquad (3.1\text{-}27)$$

Fig. 3-2 Drift velocity for electrons in Ar and Ar-HCl mixtures as a function of E/N. Experimental data for the drift velocity in pure Ar (o) [79] are shown.

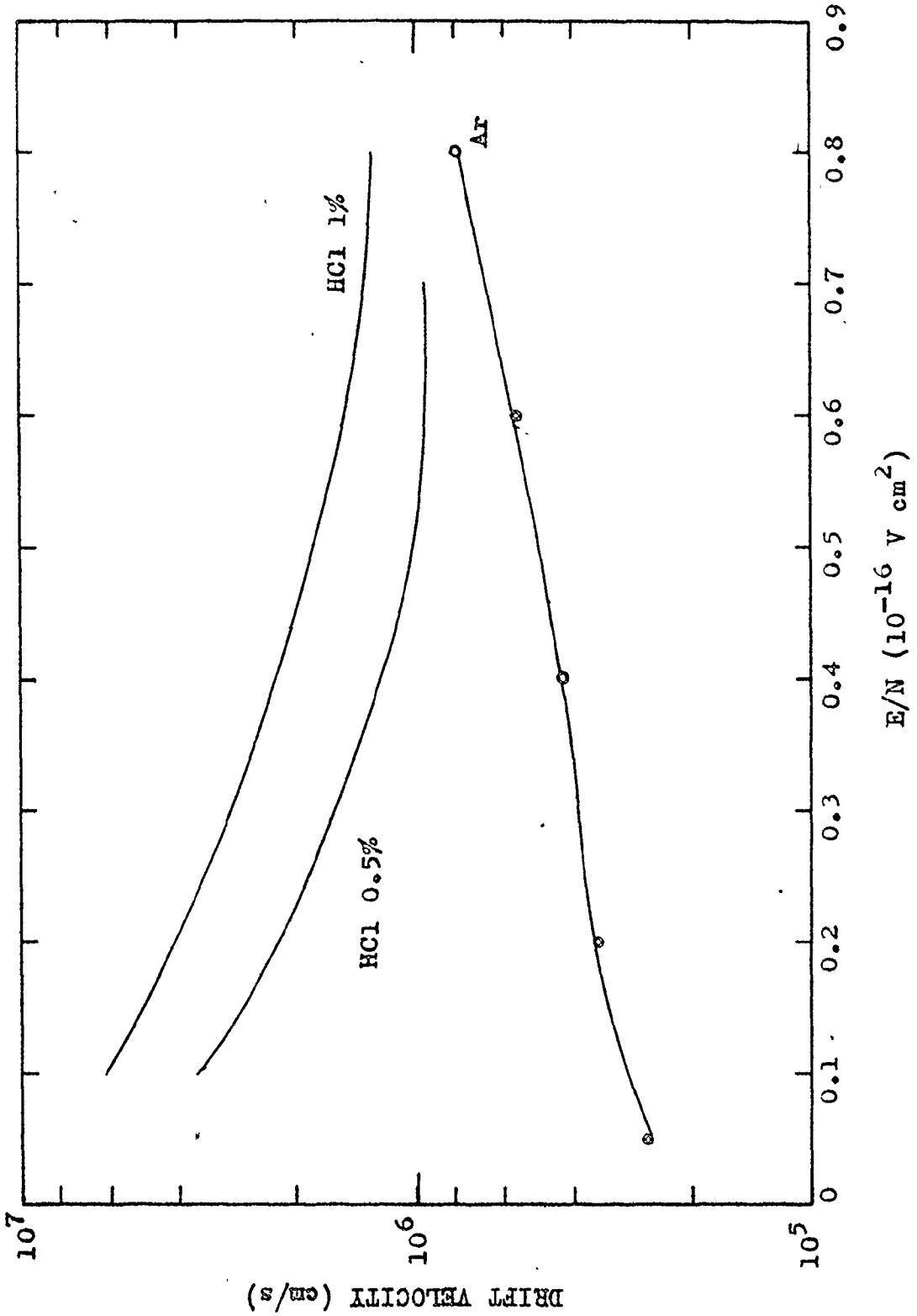
DRIFT VELOCITY (cm/s)
10^7
10^6
10^5
HCl 1%
HCl 0.5%
Ar
0
0.1
0.2
0.3
0.4
0.5
0.6
0.7
0.8
0.9
E/N (10^{-16} V cm^2)

Fig. 3-3 Characteristic energy for electrons in Ar and Ar-HCl mixtures as a function of E/N. Experimental data for the characteristic energy in pure Ar (△) [79] are shown.

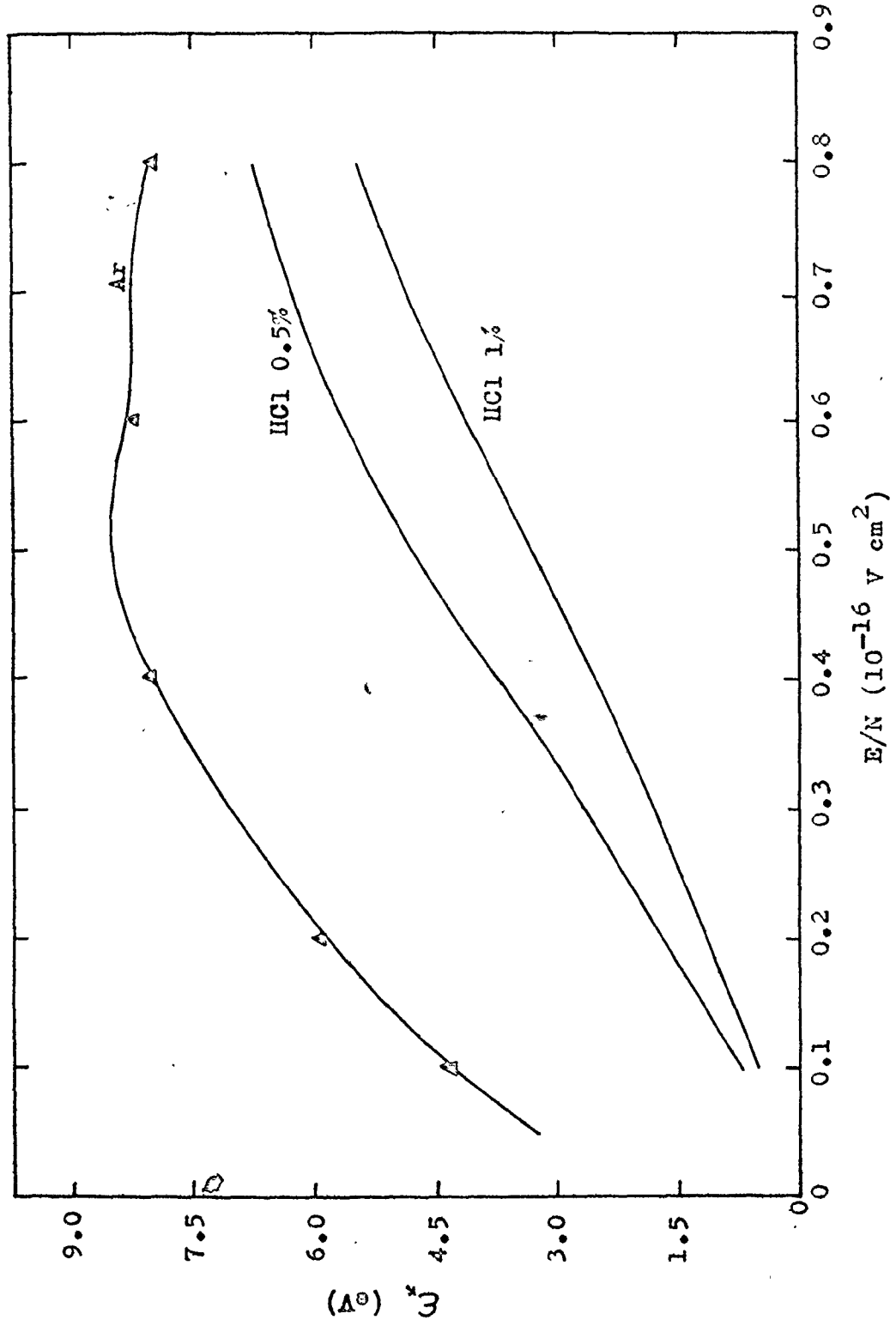
Ar
HCl 0.5%
HCl 1%
ε_x (eV)
E/N (10^{-16} V cm^2)
0
0.1
0.2
0.3
0.4
0.5
0.6
0.7
0.8
0.9
1.5
3.0
4.5
6.0
7.5
9.0

Fig. 3-4 Average energy for electrons in Ar and Ar-HCl mixtures as a function of E/N

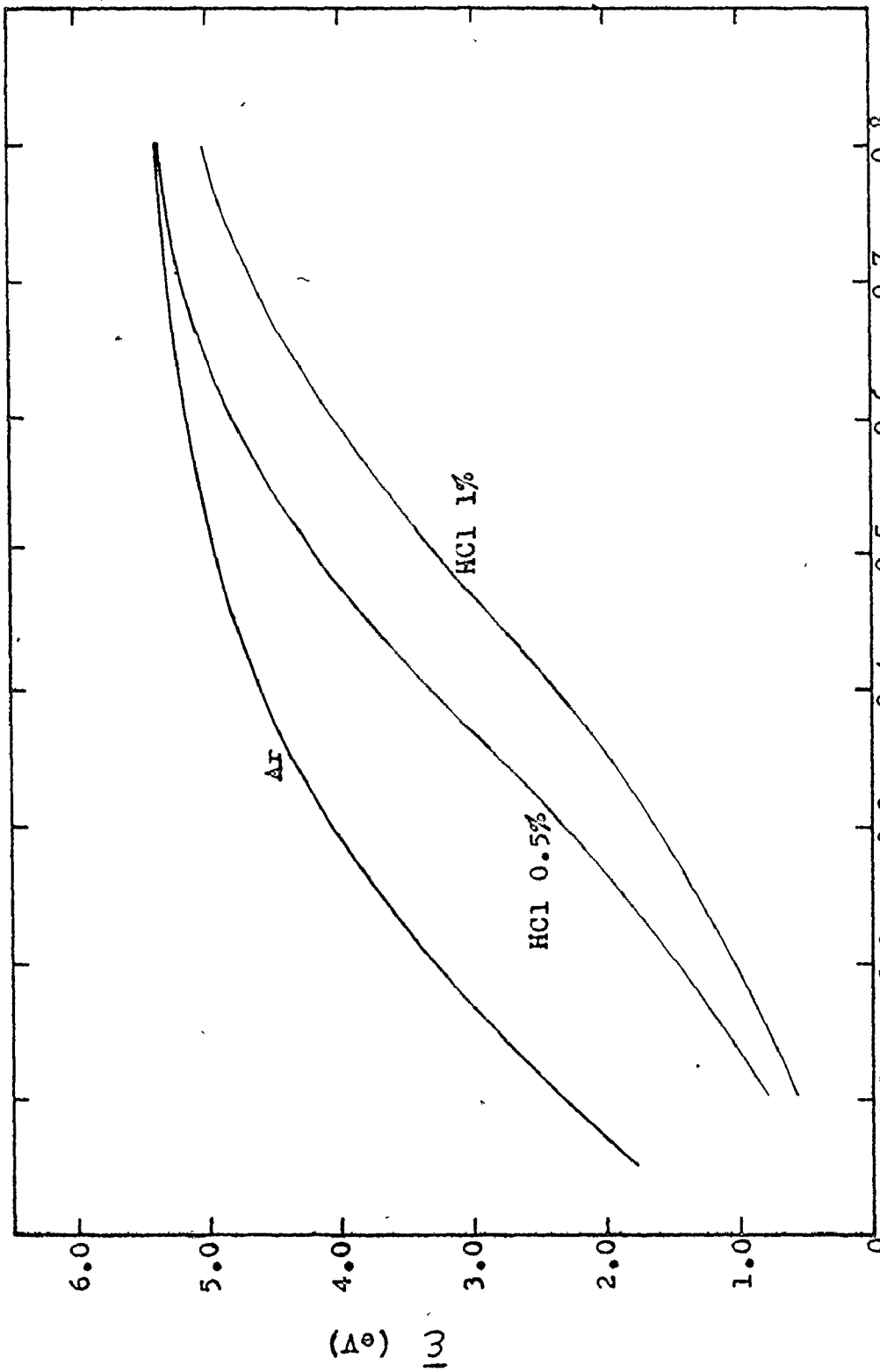
Ar
HCl 0.5%
HCl 1%
E/N (10^{-16} V cm^2)
0
0.1
0.2
0.3
0.4
0.5
0.6
0.7
0.8
1.0
2.0
3.0
4.0
5.0
6.0
ε (eV)

Fig. 13

Fig. 3-5 Rate coefficient for vibrational excitation (0→1) of HCl by electron impact. The rate coefficient were calculated using a Maxwellian electron energy distribution and using the electron energy distribution determined by our Boltzmann code for pure Ar.

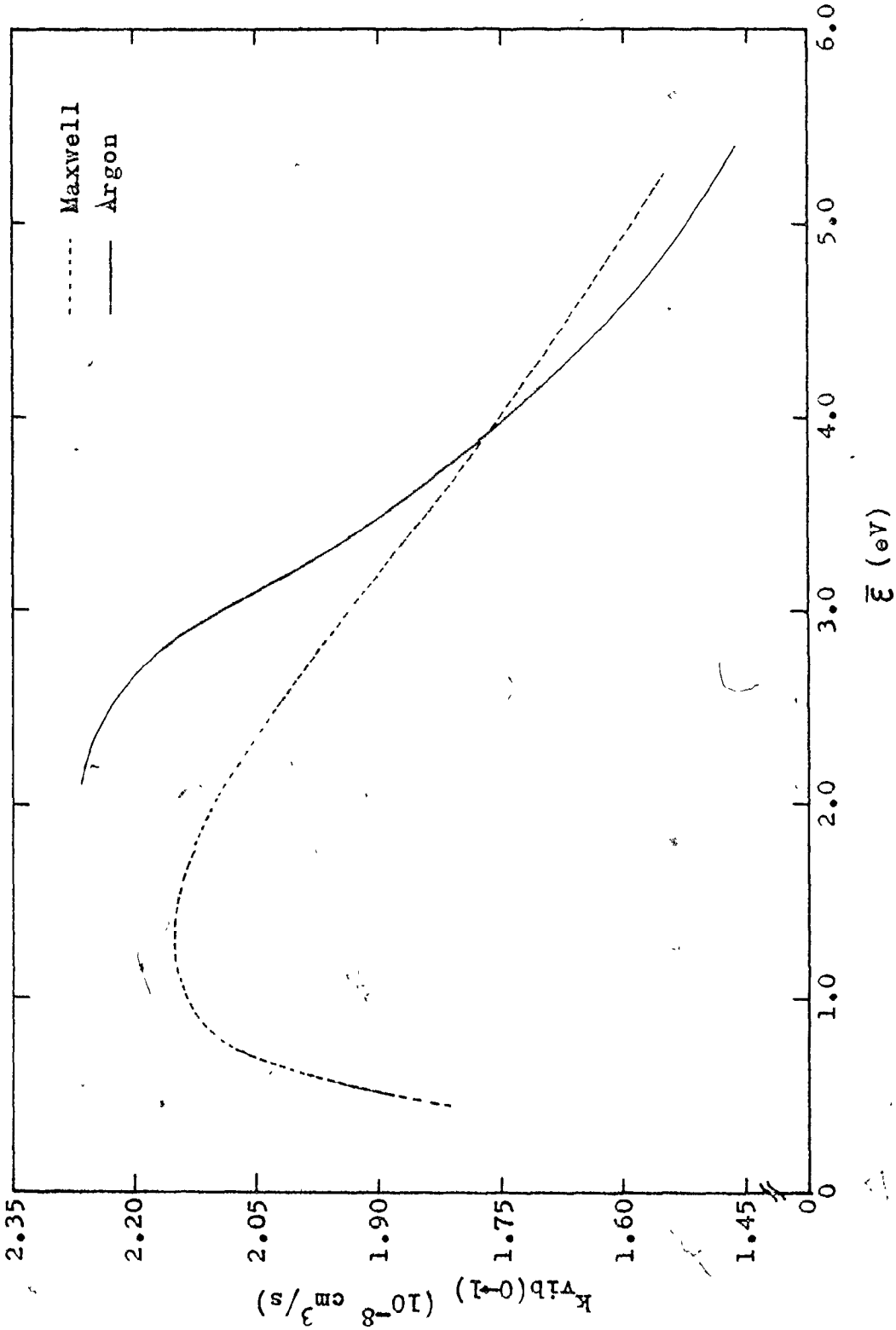
Maxwell
Argon
$k_{vib}(0\rightarrow1)$ (10^{-8} cm^3/s)
$\bar{\varepsilon}$ (eV)
2.35
2.20
2.05
1.90
1.75
1.60
1.45
0
1.0
2.0
3.0
4.0
5.0
6.0

Fig. 3-6 Rate coefficient for dissociative attachment of electron to HCl as a function of the average electron energy. The rate coefficient functions are calculated for different electron energy distribution, which are those for; pure Ar (□); Ar-HCl (99.5:0.5) (———); Ar-HCl (99:1) (-----); and Maxwell (+).

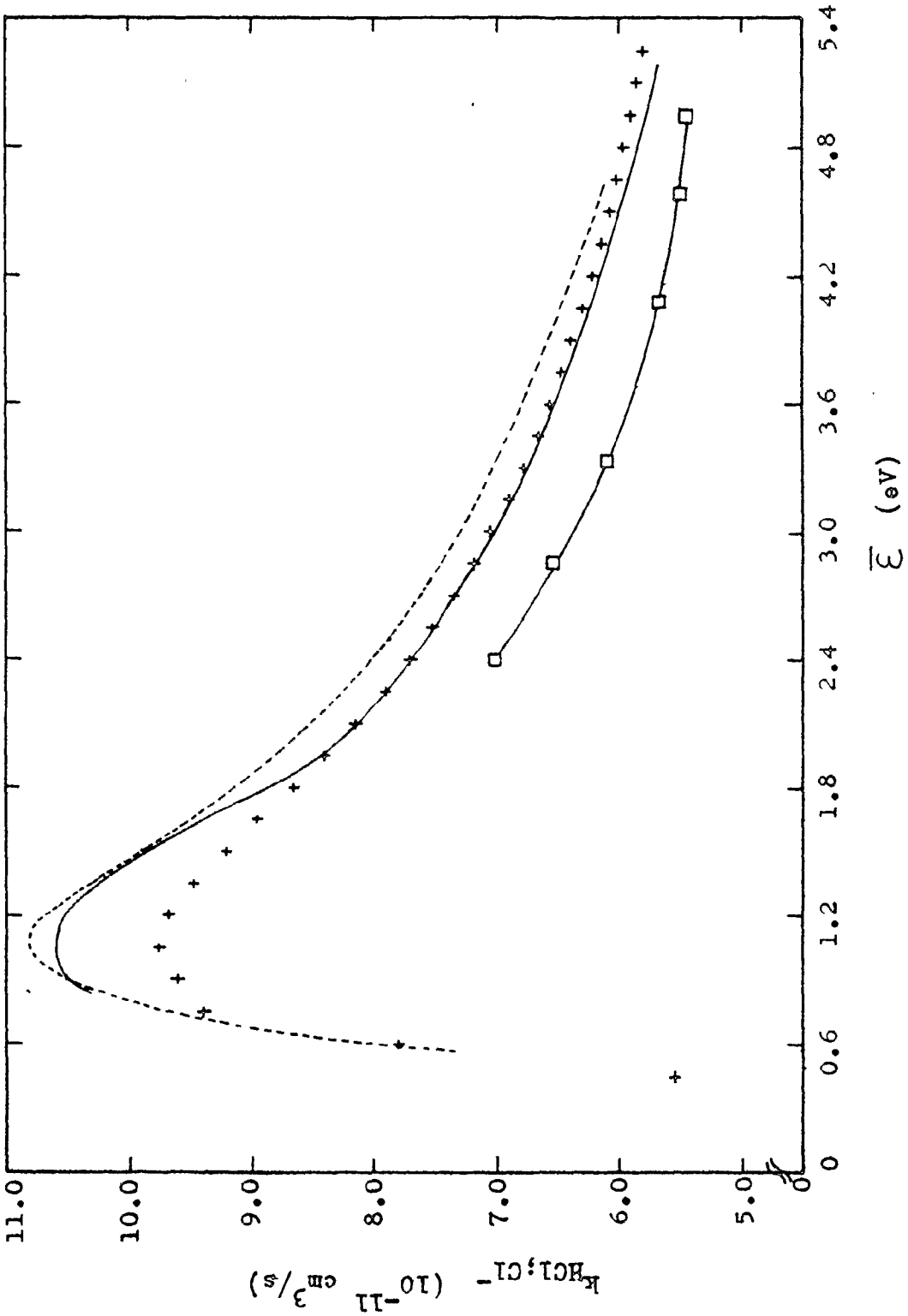
11.0
10.0
9.0
8.0
7.0
6.0
5.0
0
0.6
1.2
1.8
2.4
3.0
3.6
4.2
4.8
5.4
$\bar{\varepsilon}$ (eV)
$k_{HCl;Cl^-}$ (10^{-11} cm^3/s)

Fig. 3-7 a) Drift velocity for electrons in N_2, Ar-N_2 and Ar-N_2-HCl mixtures as a function of E/N. The full curve is Ar-N_2 (36:64) and the dashed curve is Ar-N_2-HCl (35:64:1). b) Characteristic energy for electrons in N_2 and Ar-N_2-HCl (35:64:1) (dashed curve) as a function of E/N. Experimental data for the drift velocity and characteristic energy in pure N_2 (□) [80] are shown.

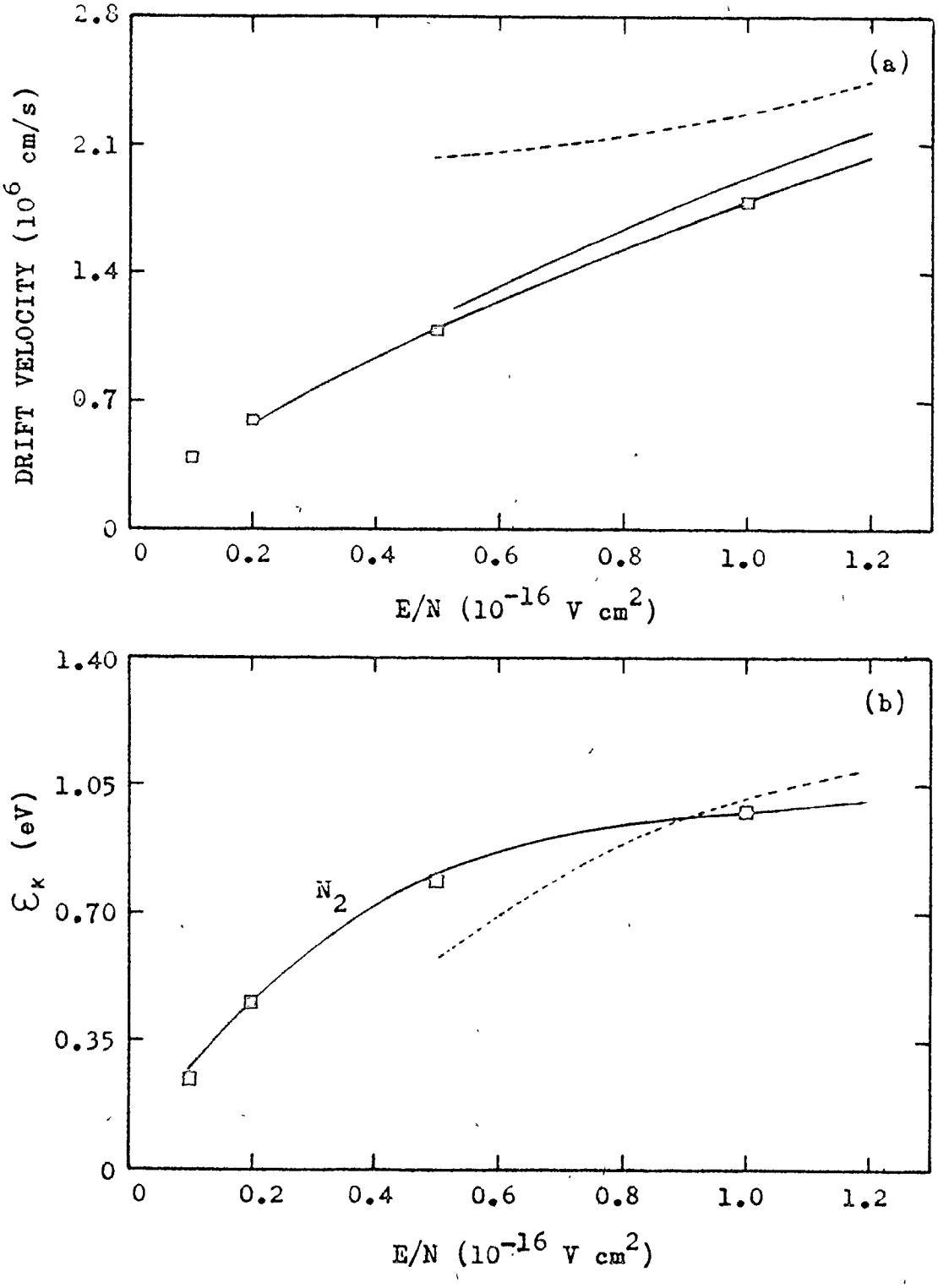
(a)
DRIFT VELOCITY (10^6 cm/s)
2.8
2.1
1.4
0.7
0
0
0.2
0.4
0.6
0.8
1.0
1.2
E/N (10^{-16} V cm^2)
(b)
$\mathcal{E}_k$ (eV)
1.40
1.05
0.70
0.35
0
N_2
0
0.2
0.4
0.6
0.8
1.0
1.2
E/N (10^{-16} V cm^2)

Fig. 3-8 a) Average energy for electrons in N_2 and Ar-N_2-HCl (35:64:1) (dashed curve) as a function of E/N. b) Rate coefficient for dissociative attachment of electron to HCl as a function of the average electron energy. These rate coefficient functions were calculated using a Maxwellian electron energy distribution (——) and also using the electron energy distribution determined by our Boltzmann code for an Ar-N_2-HCl (35:64:1) mixture (-----).

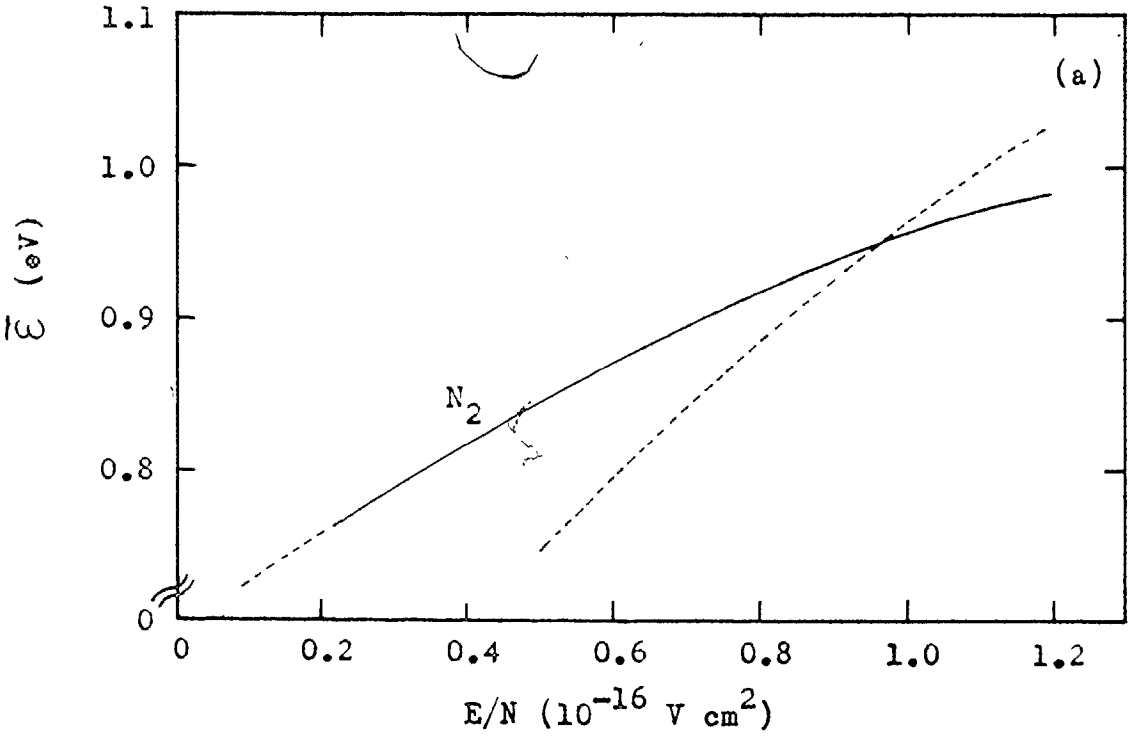
(a)
$\bar{\varepsilon}$ (eV)
1.1
1.0
0.9
0.8
0
N_2
0
0.2
0.4
0.6
0.8
1.0
1.2
E/N (10^{-16} V cm^2)

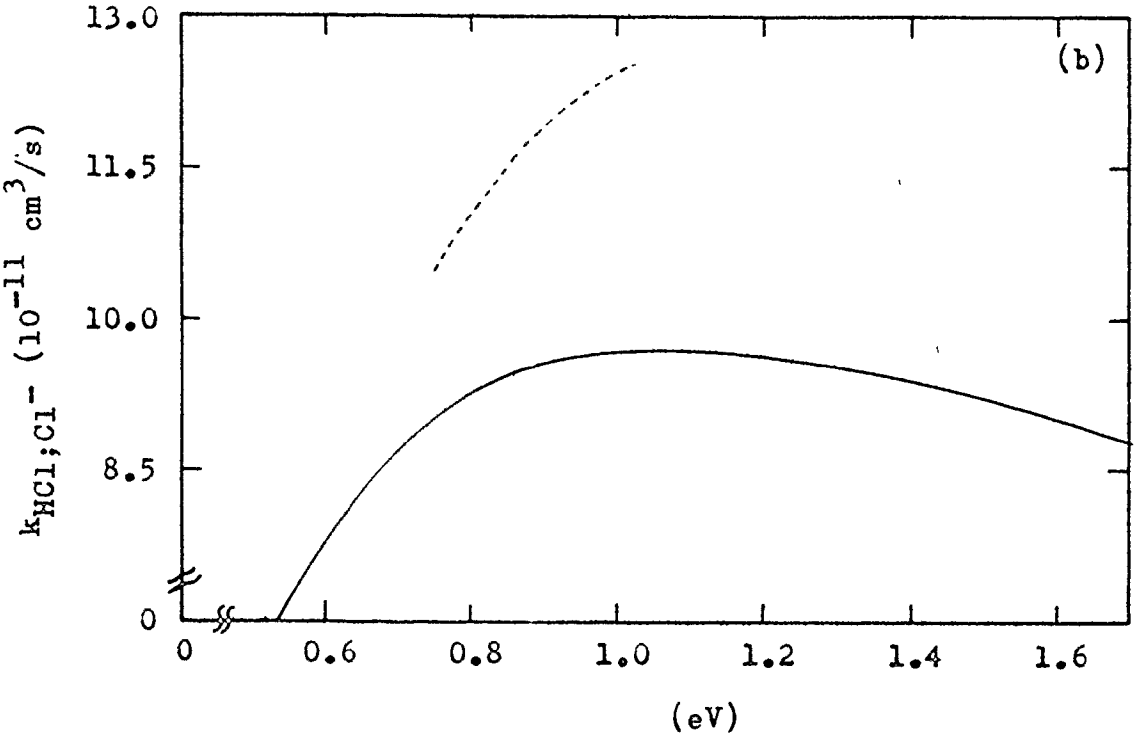
(b)
$k_{HCl;Cl^-}$ (10^{-11} cm^3/s)
13.0
11.5
10.0
8.5
0
0
0.6
0.8
1.0
1.2
1.4
1.6
(eV)

3.1.3 Reaction kinetics of the discharge plasma

The reaction kinetics of the Ar-Hcl or Ar-N_2-HCl plasmas are rather complex, involving several ionic species and a large number of excited atomic and molecular species. Since our interest was directed toward the determination of the temporal evolution of the plasma conductivity, it was possible to build an adequate description of phenomenon by considering the electrons and ionic species alone.

We have listed in table 3-1 the important electron-ion reactions relevant to the present case together with the kinetics of the precursor species.

TABLE 3-1

Reaction	Rate ($cm^3 s^{-1}$)*	Reference
$Ar^+ + 2Ar \rightarrow Ar_2^+ + Ar$	4.4×10^{-31}	[42]
	2.5×10^{-31}	[43]
	1.46×10^{-31}	[44]
	5×10^{-32}	[45]
	1.9×10^{-31}	[46]
	2.07×10^{-31}	[47]
	2.3×10^{-31}	[48]
	3.0×10^{-31}	[49]
		(3.1-28)
$e + Ar_2 \rightarrow Ar^* + Ar$	$7.5 \times 10^{-7} \left(\frac{T_e}{300^\circ K}\right)^{-0.67}$	[50]

$N_2^+ + 2N_2 \rightarrow N_4^+ + N_2$	7.2×10^{-29}	[51]	(3.1-30)
$N_2^+ + e \rightarrow N + N$	2.8×10^{-7}	[52]	(3.1-31)
$N_4^+ + e \rightarrow N_2 + N_2$	$**8.0 \times 10^{-8}(\varepsilon_K)^{-1.8}$	[53]	(3.1-32)
$HCl + e \rightarrow H + Cl$	$\sim (5\text{-}10)\ 10^{-11}$		
$\rightarrow H^- + Cl$			
$O_2 + e \rightarrow O^- + O$	3.0×10^{-12}	[54]	(3.1-34)

---

* the rate is expressed in $cm^6 s^{-1}$ for three-initial-article reactions.

** ε_K is the characteristic energy in ev.

3.1.4 Modeling of the Discharge Current Pulse (attachment dominated plasma)

A simple model of the discharge current pulse, for the case of an attachment dominated plasma, is developed in this section.

3.1.4 a) General approach

Computation of the evolution of a current pulse, when the electric field is distorted by electrons and ions, requires solution of the appropriate rate equations for the

different species (including the boundary conditions) together with the simultaneous solution of Poisson's equation. The rate equations are [55]

$$\frac{\partial N_i}{\partial t} = \nabla\cdot\underset{\sim}{J}_i + S_i - \nu_i N_i + \sum_{jl} N_j N_l k_{jl;iv} - \sum_{l} N_i N_l k_{il;\nu}$$

$$+ \sum_{abc} N_a N_b N_c k_{abc;iv} - \sum_{c,d} N_c N_d N_i k_{cdi;i\nu} , \qquad (3.1\text{-}35)$$

and Poisson's equation is

$$\nabla\cdot\underset{\sim}{E} = -e(N_e - \sum_j N_j^{(+)} + \sum_j N_j^{(-)}) , \qquad (3.1\text{-}36)$$

where S_i is a source term for the specie i, $k_{ab;}$ and $k_{abc;}$ are the rate coefficients for two- and three-initial-particles, respectively. The final particles are represented collectively by ν (or $i\nu$). $N_j^{(+)}$ and $N_j^{(-)}$ are the number densities of positive and negative ions, respectively.

The above approach has been followed by Davies et al [56, 57], who have developed a method for computing the evolution of ionization currents between plane parallel electrodes when the field is distorted by electrons and ions. Davidson [58] has given a formal solution to the problem, for the case where the space charge can be neglected.

The gap current $I_g(t)$ for the case of plane parallel

electrodes is given by

$$I_g(t) = \frac{1}{d}\int_0^d \int_S (\underset{\sim}{J}_e + \sum_i \underset{\sim}{J}^{(-)} + \sum_j \underset{\sim}{J}^{(+)}) \cdot \hat{z}\, dS dz, \qquad (3.1\text{-}37)$$

where $\hat{z}$ is a unit vector perpendicular to the surface of the electrodes, $\underset{\sim}{J}^{(+)}$ and $\underset{\sim}{J}^{(-)}$ are the positive-ion and negative-ion current-densities, respectively, and d is the inter-electrode distance.

3.14 b) Simplified approach

It is clear that the solution of Eqs. (3.1-35) and (3.1-36) should give accurate results. However, it is also clear that such a method would hardly be suitable for experimental data analysis. Instead we decided to adjust the experimental conditions so that the observed current pulse could be related in a simple manner to the parameters of interest.

We first describe qualitatively the temporal evolution of a typical discharge current pulse. The current pulse starts when the electron-beam turns on. The primary electrons ionize the gas mixture, creating a high average-electron-energy ($\sim$17 ev), low density ($\sim 10^{13} cm^{-3}$), non-uniform plasma. After the electron-beam turns off the electron energy distribution relaxes rapidly to its quasi-steady-state value (within $\sim$5ns). At the same time the cathode-fall region builds up, and the plasma conductivity

starts to decrease, because of the electron-positive ion recombination process and because of dissociative attachment of electrons to HCl. The electron density finally becomes negligible in comparison to that of the positive and negative ions, which determine the plasma conductivity at later times.

The cathode is connected to the positive column of the high-pressure glow discharge by the cathode-fall zone. This is a region of large positive ions density over which the electric field varies from a very large value ($\sim 10^7$ V·m^{-1}) down to $\sim 10^5$ Vm^{-1}, according to $E \sim -2V_c/d_c\,[1-z/d_c]$ (where d_c is the cathode-fall region "thickness" and V_c is the cathode-fall potential drop). The solution of the problem is very complex since we are dealing with the behavior of electron swarms in electric fields having rapid spatial variation [59, 60]. Consequently equilibrium between the electrons and the electric field cannot be reached and therefore the electron energy distribution can be very different from that found in the uniform field case [59, 60]. However, it is sufficient for us to know the bulk characteristics of the cathode-fall zone. These are that the voltage drop V_c (with an aluminum cathode) is $\sim$ 100 V for argon and $\sim$ 200 V for nitrogen [28], the thickness d_c of the zone is $\sim$ 5 μm for both argon and nitrogen at atmospheric pressure [61], and that the cathode-fall region is an efficient source of electrons.

The positive column of the glow discharge is a zone of major importance. We expect the field to remain reasonably uniform during the whole current pulse because the electron number-density is relatively low and the non-uniformity of the plasma is not very large. Thus Poisson's equation (3.1-36) doesn't need to be considered in the present calculation. Furthermore, the spatially dependant term appearing in the rate equations can be neglected if the following conditions hold:

$$\frac{D}{P_s}\left[\frac{1}{r}\frac{\partial}{\partial r}\left(r\frac{\partial P_s}{\partial r}\right)+\frac{\partial^2 P_s}{\partial z^2}\right] << k_{HCl;Cl^-} N_{HCl}, \qquad (3.1\text{-}38a)$$

and

$$\frac{v_d}{P_s}\frac{\partial P_s}{\partial z} << k_{HCl;Cl^-} N_{HCl} \qquad (3.1\text{-}38b)$$

where P_s is the secondary-electron production rate, v_d is the drift velocity of the electrons, and D their diffusion coefficient.

We assume that conditions (3.1-38a) and (3.1-38b) are satisfied in the present case (the validity of this assumption is discussed in more detail in Chapter 4). The problem is, therefore reduced to the solution of a system of stiff non-linear differential equations. A computer code, using a fourth order Runge-Kutta explicit integration scheme, was written to solve this type of problem. One of the cases

studied concerned the evolution of the species Ar^+, Ar_2^+, Cl^- and electrons in an Ar-HCl plasma. The code was used to numerically solve the following set of equations:

$$\frac{\partial N_e}{\partial t} = S_e(t) - k_{HCl;Cl^-} N_e N_{HCl} - k_{Ar_2^+;Ar} N_{Ar_2^+} N_e, \quad (3.1\text{-}39a)$$

$$\frac{\partial N_{Ar_2^+}}{\partial t} = k_{Ar;Ar_2^+} N_{Ar^+} N_{Ar}^2 - k_{Ar_2^+;Ar} N_{Ar_2^+} N_e, \quad (3.1\text{-}39b)$$

$$\frac{\partial N_{Ar^+}}{\partial t} = S_e(t) - k_{Ar^+;Ar_2^+} N_{Ar^+} N_{Ar}^2, \text{ and} \quad (3.1\text{-}39c)$$

$$\frac{\partial Cl}{\partial t} = k_{HCl;Cl^-} N_{HCl} N_e \quad . \quad (3\text{-}1.39d)$$

The rate coefficients used in the numerical calculations are those given in Section 3.1.3, except for $k_{HCl;Cl^-}$. The value of $k_{HCl;Cl}$ used for the case described in Fig. 3-9 is a factor of ~ 3 times less than that calculated with the Boltzmann code.

Figure 3-9 shows the temporal evolution of the number-density for different species (Ar_2^+...) using typical concentrations of the primary species. It can be seen that the Ar_2^+ density rapidly increases with a time constant $\sim[k_{Ar;Ar_2^+} N_{Ar}^2]^{-1}$, which is typically ~ 4.8 ns (at an electron

Fig. 3-9 Temporal evolution of the number density of Ar_2^+, Ar^+, Cl^-, and electrons. The gas mixture was Ar-HCl (99:1) with $N_{Ar} \simeq 3 \times 10^{19} cm^{-3}$. The rate coefficient for dissociative attachment of electron to HCl used was $3.5 \times 10^{-11} cm^3 s^{-1}$ and the average electron energy was fixed to 1.5 eV.

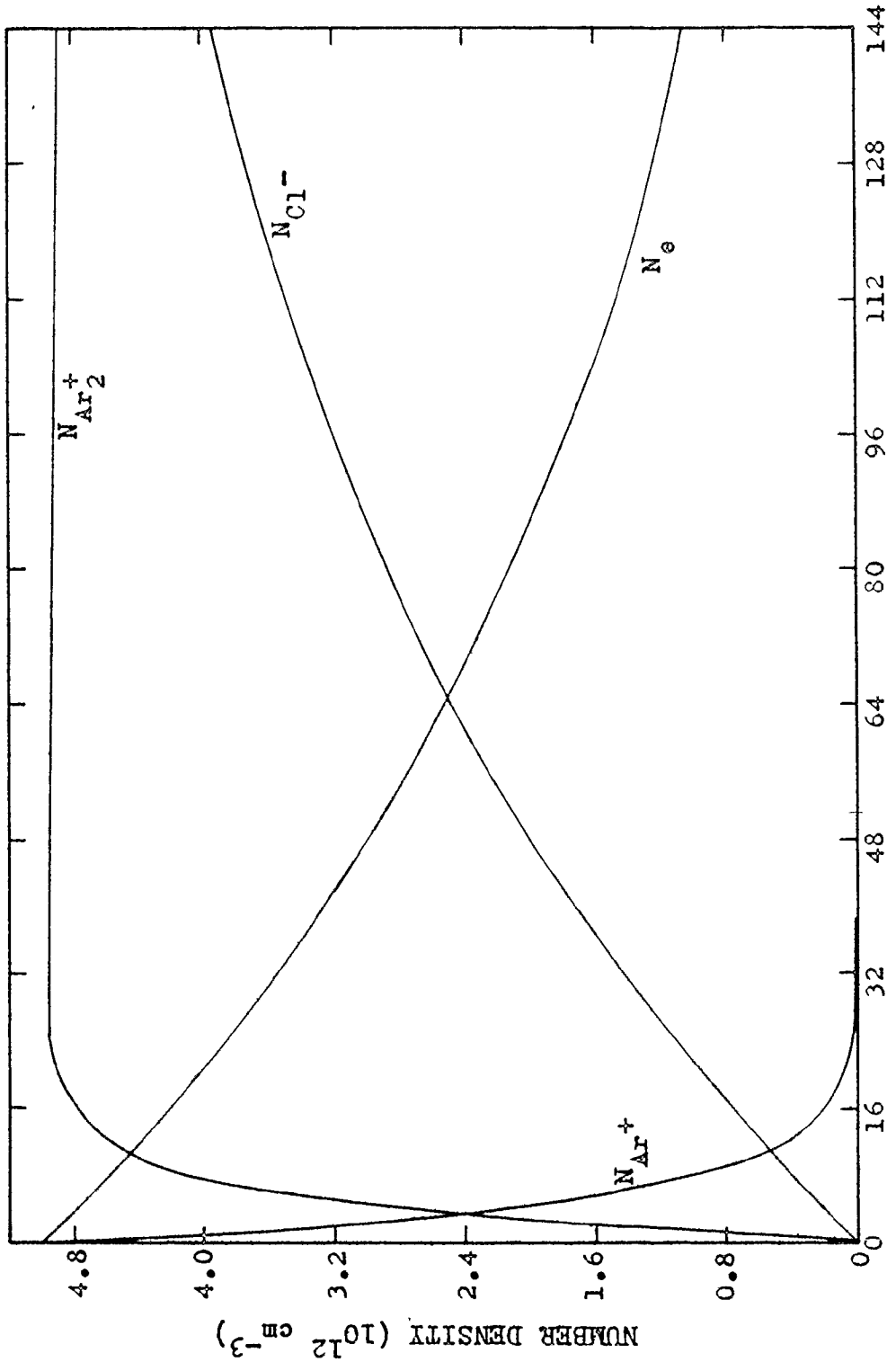
NUMBER DENSITY (10^{12} cm^{-3})
TIME (ns)
$N_{Ar_2^+}$
N_{Cl^-}
N_e
N_{Ar^+}
0
0.8
1.6
2.4
3.2
4.0
4.8
16
32
48
64
80
96
112
128
144

temperature of 1eV and a pressure of ~ 124 KPa). After the Ar_2^+ specie has reached its peak, it then starts to decrease with a characteristic time much larger than that for electrons. The electron number-density varies nearly exponentially with a characteristic time constant $\tau = [k_{HCl;Cl^-} N_{HCl} + k_{Ar_2^+;Ar} N_e(t=0)]^{-1}$ (since $N_{Ar_2^+}(t > t_{peak}) \approx N_e(t=0)$ over a time scale large compared to τ). The total current (J_{tot}) density is therefore approximately given by

$$J_{tot} = eN_{e_o}(|v_{Ar_2^+}| + |v_{Cl^-}| + \exp -\frac{t}{\tau}(|v_e| - |v_{Cl^-}|)), \qquad (3.1\text{-}40)$$

where v_i is the drift velocity for particles of species i.

An approximative expression for the ratio of the mobility for ions of mass M_1 moving through a gas of particles of mass M_2 to that of electrons moving in the same gas (M_2) is given by [61]

$$\frac{\mu_{ion}}{\mu_e} \sim 0.815 \left(\frac{\sqrt{2}}{6\pi} e \frac{M_e E L_g}{M_1 KT} \frac{M_2}{(M_1+M_2)}\right)^{1/2} \qquad (3.1\text{-}41a)$$

where $4\sqrt{2} L_g$ is the mean-free-path of the electrons. For $T \sim 300^{\circ}K$ (gas temperature) Eq. (3.1-41a) can be written as

$$\frac{\mu_{ion}}{\mu_e} \sim 1.38 \left(\left(\frac{M_e M_2}{M_1(M_1+M_2)}\right) E L_g\right)^{1/2} . \qquad (3.1\text{-}41b)$$

For argon, $M_I \sim 6.6 \times 10^{-26}$ kg, and $L_g \sim 10^{-7}$ m at atmospheric pressure. At a typical field strength of $\sim 3 \times 10^5$ V m^{-1} we obtain for the Cl^- ion $\mu_{ion}/\mu_e \sim 7 \times 10^{-4}$ and for Ar_2^+ $\mu_{ion}/\mu_e \sim 5.5 \times 10^{-4}$. The ion contribution to the total current then becomes $> 10^{-1}$ J_e for $t > 5\tau$. Therefore, we expect to observe a quasi exponential current pulse over a time scale of $\sim 5\tau$. A reasonably good approximation for the total current density is given by (for $t < 5\tau$)

$$J_{tot} \simeq eN_e(t=0)\exp-(t/\tau)|v_e|. \qquad (3.1\text{-}42)$$

The gap current $I_g(t)$ (which is the experimentally measured parameter) is given (for $t < 5\tau$) by

$$I_g(t) \simeq \frac{ev_e}{d}\int_0^d\int_s N_e(x,t=0)\exp-(t(k_{HCl;Cl^-}N_{HCl} + k_{Ar_2^+;Ar}N_e(x,t=0))^{-1}dx\,dy\,dz. \qquad (3.1\text{-}43)$$

Any complication resulting from the fact that $N_e(x,t=0)$ is non-homogeneous are removed by keeping the electron density at the foil ($N_e(x=0, t=0)$) low enough for $k_{Ar_2^+;Ar}N_e(0,0) \ll k_{HCl;Cl^-}N_{HCl}$. The rate coefficient for the dissociative attachment of electrons to HCl is therefore given by the simple expression

$$k_{HCl;Cl^-} \simeq (\tau N_{HCl})^{-1}. \qquad (3.1\text{-}44)$$

The trade-off between the various experimental parameters in order to work under the best conditions is discussed in detail in Chapter 4.

3.1.5 Modeling of the Discharge Current Pulse (recombination dominated plasma)

The purpose of this section is to discuss problems in the measurement of the electron-ion recombination rate coefficients, and to propose a solution. In the first part we present a simple model for the temporal evolution of the current pulse. In the second part, we describe how the e-beam gun system could be modified so as to allow measurement of the rate coefficient for the above reaction.

3.1.5 (a) Temporal evolution of the current pulse

The electron number density (N_e) in the plasma is given by

$$\frac{\partial N_e}{\partial t} = S_e - k_{rec}N_{rec}N_e - k_A N_A N_e - \tilde{\nabla}\cdot\underset{\sim}{J}_e, \qquad (3.1\text{-}45)$$

where k_{rec} and k_A are the recombination and attachment rate coefficients, respectively, and N_{rec} and N_A are the corresponding species number-density.

When $k_{rec}N_{rec} >> k_A N_A$, $N_e = N_c$ (recombination dominated

plasma). Moreover, when the term $\nabla \cdot J_e$ is negligible compared to $k_{rec} N_{rec} N_e$, Eq. (3.1-45) may be integrated from t=0 at cutoff (i.e., when S_e=0) to give

$$N_{eo}/N_e = ((k_{rec}N_{eo}/k_A N_A) + 1) \exp (k_A N_A t)$$

$$-(k_{rec}N_{eo}/k_A N_A), \qquad (3.1\text{-}46)$$

where $N_{eo} = N_e(t=0)$. In the absence of attachment Eq. (3.1-46) reduces to

$$\frac{N_{eo}}{N_e} = 1 + k_{rec} N_{eo} t \quad . \qquad (3.1\text{-}47)$$

The gap current $I_g(t)$ is therefore given by

$$I_g(t) = \frac{ev_d}{d} \int_v \frac{N_{eo}}{1 + k_{rec} N_{eo} t} \, dV \quad . \qquad (3.148)$$

The inhomogeneity in the initial secondary-electron plasma produced with the present arrangement prevented us from measuring k_{rec} in any simple way. However, if $N_{eo}(x,y,z) \approx$ constant, then the solution of the problem becomes straightforward, provided that the volume of the discharge is known. In this case, the measurement of $I_g(t=0) = \frac{V}{d} N_{eo} v_d$, together with the slope of $I_g(t=0)/I_g(t)$, permits determination of N_{eo} and finally k_{rec}.

b) Proposed modified electron-beam gun system

The creation of a quasi-homogeneous plasma column appears to be feasible if the vacuum-diode anode and aluminum foil window arrangement is modified as illustrated in Fig. 3-10. The present stainless-steel mesh anode is replaced by an 18-μm thick aluminum foil, and the present aluminum-foil window is replaced by a 6-μm aluminized mylar film. The diameter of the "output window" is 0.15 cm, its distance from the anode is ~ 1.5 cm, and the "primary window" (at the aluminum-foil anode) diameter is ~ 0.6 cm.

The electron-beam current density incident on the anode is ~ 175 A/cm^2 over the primary window area (estimated from the electron-beam gun data given in Chapter 2). The transmission coefficient of a 18-μm thick aluminum foil is estimated to be ~ 75% for 90-Kev incident electrons [16]. Therefore, the output current density (J_o) at the primary window is estimated to be ~ 130 A/cm^2. If we assume that the angular spread of the electron beam emerging from the primary window is that of a totally diffuse distribution function, then we can use Eq. (3.1-5) to estimate the on-axis current density incident on the output window. With the present configuration the calculated value is ~ 2.5 A/cm^2.

Because of the low density and small thickness of the aluminized mylar film, all the incident electrons should be

Fig. 3-10 Proposed modification to the electron-beam gun. The stainless steel mesh anode and aluminum foil electron beam window shown in Fig. 2-2 are replaced by a 18-μm thick aluminum foil and an aluminized mylar film, respectively.

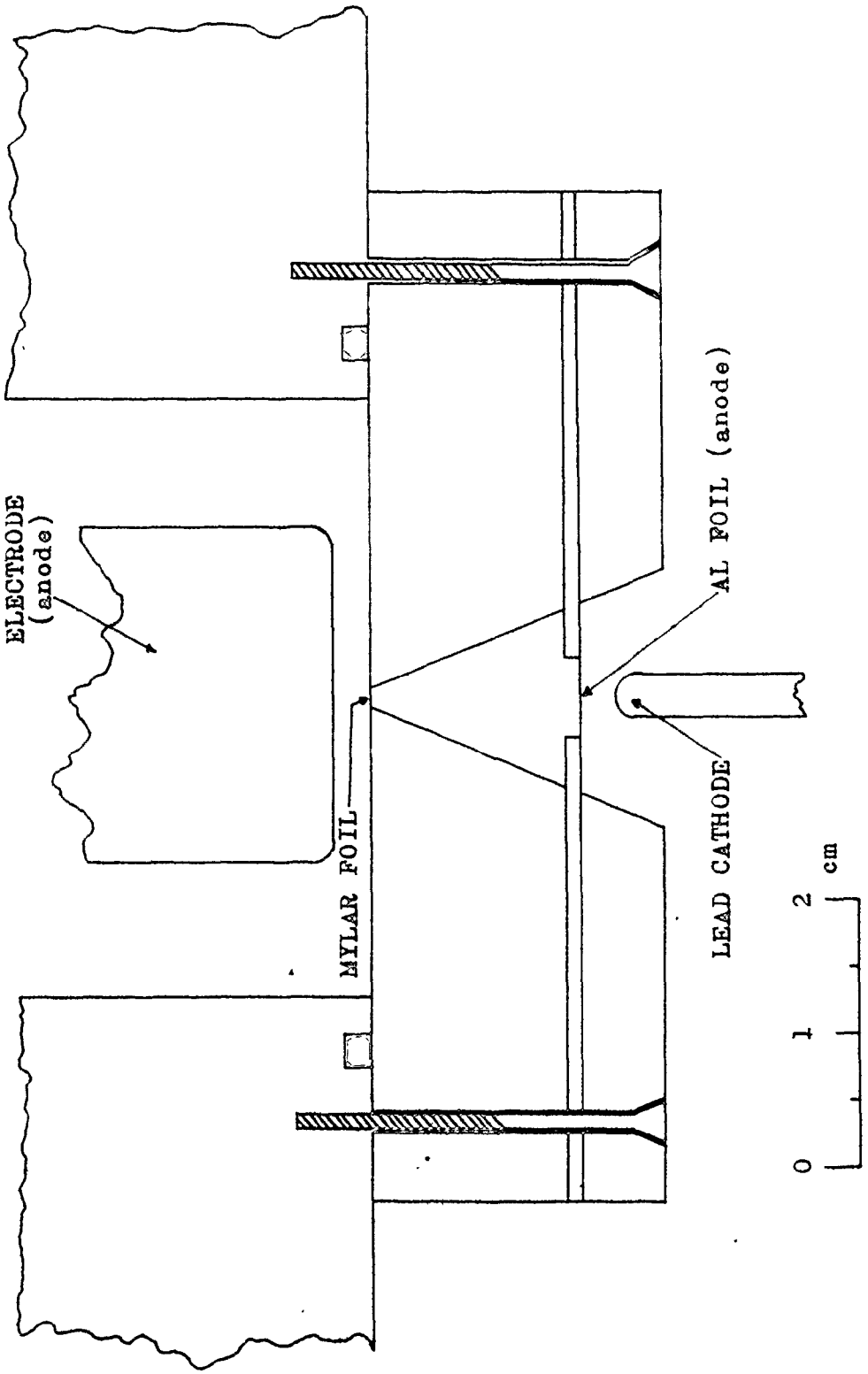
ELECTRODE
(anode)
MYLAR FOIL
AL FOIL (anode)
LEAD CATHODE
0
1
2
cm

transmitted (~100%) without any significant increase in the beam angular spread. Then the main contribution to the electron-beam angular spread comes from passage through the anode foil and from the scattering in the gas. The geometry of the configuration shown in Fig. 3-10 makes the angular spread at the center of the output window ≈ 0.06 π rad (with a sharp cutoff at larger angles). The contribution coming from the scattering in the gas would typically be ~ 0.05 π at 0.3 cm from the cathode and at a pressure ~ 100 KPa.

The primary window and output window are chosen such diameters and their large separation (1.5 cm) that the emerging electron-beam current density will be quasi-uniform over the surface of the output window. Furthermore $\langle\cos\theta\rangle_{avg}$ should be ≈ 1 over the whole discharge volume. Therefore $P_s(r,z)$ should be proportional to the current density $J(r,z)$. The ratio of the on-axis (r=0) current density at the anode to that at the cathode (mylar film) is estimated to be ~0.7 using Eq. (3.1-5) (lower bound). If we assume that the current density is uniform at the anode, then the plasma column diameter is estimated to be $\sim(0.7)^{-1/2}$ times that at the cathode (an increase of ~ 20%). This is not exactly an homogeneous plasma. However, we point out that it can be easily characterized with a reasonably good accuracy. We also point out that the plasma will tend to equilibrate its inhomogeneity through recombination. The

ratio of the electron density at the anode (N_{ea}) to that at the cathode (N_{ec}) is given by

$$\frac{N_{ea}}{N_{ec}} = \lambda \frac{(1 + k_{rec}N_{eoc}t)}{(1 + \lambda k_{rec}N_{eoc}t)} , \qquad (3.1\text{-}49)$$

where $\lambda = 0.7$ in the proposed arrangement. The time at which the ratio $N_{ea}/N_{ec} = x$ is given by

$$t_x = \frac{(x/\lambda - 1)}{1-x} (k_{rec}N_{eoc})^{-1} . \qquad (3.1\text{-}50)$$

Therefore, in the present example $t_{0.8} = 0.7 (k_{rec}N_{eoc})^{-1}$ and $t_{0.9} = 2.8 (k_{rec}N_{eoc})^{-1}$ (in 100 KPa of nitrogen, $N_{eoc} = 1.75 \times 10^{13}$ cm^{-3}, and $(k_{rec}N_{eoc})^{-1} = 500$ ns for $E/N > 0.4\times10^{-20}$ V·m^2 [53]).

The above illustrates that recombination rate measurements can be carried out with a properly modified electron-beam-gun system.

CHAPTER 4

ELECTRON-CAPTURE RATE-COEFFICIENT MEASUREMENT

Electron-capture processes are commonly studied using two experimental methods, the electron-swarm and the electron-beam technique. Electron-swarm experiments measure quantities which are averaged over the electron energy distribution. In beam experiments, efforts are made to produce nearly mono-energetic electrons. Consequently the data obtained by the latter method may be regarded as a first approximation to the shape of the curve representing the capture cross-section as a function of electron energy. One of the major deficiencies in beam experiments is that it is very difficult to obtain knowledge of absolute cross-sections for electron capture. Christophorou et al [62] have shown that the swarm and beam experiments can be combined to obtain much more information on electron-capture processes than can be obtained with either method alone.

For this thesis, the main objective was to construct a system that could be used for measuring the rate coefficient of electron-capture reactions (swarm experiment). The system was used to determine the rate coefficient of the dissociative attachment of electrons to HCl, and to use the results to calibrate the cross-sections measured during beam experiments.

The last two sections of this chapter present results

obtained from the dissociative attachment experiment.

4.1.1 Literature review

Various swarm methods have been used in order to determine the rate coefficient for electron-capture processes. Among those the method of Botzner and Hurst [63] has been applied by Christophorou et al [62]. In this method, electrons are produced in a plane normal to the applied electric field. They are then allowed to drift through a gas mixture composed of a non-attaching carrier gas (which determines the electron energy distribution) and a small fraction of the attaching gas. The attachment coefficient is calculated from measurements of the current pulse produced in the parallel-plate chamber, and the free-electron drift velocity, v_d. Measurement of the current pulse permits determination of $\alpha(E/N)$ (the probability of capture per centimeter traveled in the field direction divided by the number density of the attaching gas). The attachment coefficient is then given by $\alpha(E/N) \times v_d$.

Nygaard et al [64] have designed simple self-calibrating method to determine $\alpha(E/N)$. The method consists of producing a short burst of electrons at the cathode (of a parallel-electrode discharge-chamber), and then integrate the circuit current produced by the flow of fast electrons and slow negative ions. The resulting voltage transient

is observed with an oscilloscope. As before, the free-electron drift velocity has to be determined in an independent experiment.

Another method (which requires a large and expensive electron-beam gun system) has been used by Chen et al [65]. In their experiment the rate coefficient of the observed reaction was calibrated by using the electron-ion (N_4^+) recombination rate coefficient together with the electron drift velocity in pure N_2.

The last method considered here is the one that has been chosen by us, and which has been used by several other workers [53, 66, 28]. Its simplicity and low cost justify our choice. Furthermore the coefficient is obtained directly without either having to calibrate the measured value to any other reaction rate coefficient or having to know the drift velocity of the free electrons.

Dissociative attachment of electrons to HCl has been studied by several workers, employing various methods: electron-impact mass-spectrometer [67-73], total ionization [74,75], and "swarm-beam" method [62]. The shape of the curves of the cross-sections as a function of the electron energy are in reasonably good agreement in all cases. However the absolute value for the cross-section differs by a factor as large as ~ 5.

The research reported here was carried out on HCl because accurate data on electron attachment in HCl are

pivotal in understanding the excitation mechanisms of XeCl excimer lasers.

4.1.2 The Experimental Parameters

The reasons for the choice of the external circuit parameters and for the choice of the materials used in the construction of the conductivity cell have been discussed extensively in Section 2.2. The object of the present section is to give the reasons for the compromises made between the experimental parameters, absolute HCl concentration, HCl fraction, carrier gas, electron number density, characteristic time ($[k_{HCl;Cl^-} N_{HCl}]^{-1}$), and electrodes gap spacing.

Because the cross-section for the excitation of the vibrational levels of HCl are not well known, we had to keep the HCl mole fraction small in order to know accurately the electron-energy distribution of the swarm. An Ar-N_2-HCl plasma was suitable for this purpose. Even with an HCl mole fraction as high as 1%, only a small correction has to be made in order to account for the presence of HCl. This can be seen by reference to Fig. 3.7, and also by considering the cross-sections for both HCl and N_2. In the case of an Ar-HCl plasma, a 1% mole fraction of HCl has a significant effect on the electron-energy distribution (see e.g., Fig. 3-4). This results in an increase in the uncertainty

of the average electron energy at a given value of E/N.

The HCl mole fraction must also be kept small enough so that the cathode-fall voltage drop is not changed by the presence of the molecule. The typical HCl mole fractions (~0.5-1.0%) used in our experiments were a compromise between the previous requirements and those described below.

The reduced field (E/N) was varied over the range $0.2\text{-}1.0 \times 10^{-20}$ V·m^2. The interelectrode gap was adjusted to ~0.6 cm. This prevented the plasma-column diameter from exceeding the dimension of the uniform-field region. At the same time this allowed us to use large gap voltages even at low values of E/N and total pressures < 350-400 kPa. In the evaluation of E/N the correction for the cathode-fall voltage drop never exceeded 15% of the gap voltage.

The Boltzmann code has to be applicable to the present problem under the condition that the electron-electron interaction term is neglected. For $E/N > 0.4 \times 10^{-20}$ V·m^2, we have previously shown in Section 3.1.3 that this condition can be written as $N_{ep} < 5 \times 10^{13}$ cm^{-3} in argon and $N_{ep} < 10^{14}$ cm^{-3} in nitrogen (both at 200 kPa). The condition $\tau_{recombination} >> \tau$ must also hold because we want to observe an exponentially decaying current pulse. On the other hand, the conductivity of the plasma must be kept large enough for the S/N ratio to be >>1. This establishes a lower limit on the electron density in order to achieve sufficient signal. However, this was not a serious problem because the shield

was quite effective (see Figs. 2-17 a and b).

The relaxation time τ_R must be kept small in comparison to the current pulse decay time $\tau \approx (k_{HCL;Cl} \cdot N_{HCL})^{-1}$. This condition imposes an upper limit on the HCl concentration (N_{HCL}). However the Ar-N_2-HCl plasma is generally within this limit since the relaxation time $\tau_R \sim 100$ ps.

The above conditions were simultaneously satisfied when the electron-beam current density was adjusted to $\sim$ 1-2 A/cm^2 and the total pressure was in the range $\sim$50-350 KPa (with an HCl mole fraction $\sim$1%). The peak electron number-density, at 200KPa, was $\sim 4 \times 10^{13}$ cm^{-3} in N_2 and $\sim 5 \times 10^{13}$ cm^{-3} in Ar. The characteristic decay time τ, measured in Ar-HCl (99:1) at 200KPa, was $\tau \sim 40$ns $>> \tau_R \sim$3-5ns (at 200KPa). Therefore, the Boltzmann code is applicable to the present case when $E/N > 0.4 \times 10^{-20}$ V·m^2 (the same is true with the Ar-N_2-HCl mixture).

The electron-ion recombination rates are $\sim 8.0 \times 10^{-8}$ cm^{3}s^{-1} and 2.5×10^{-8} cm^{3}s^{-1} for nitrogen [53] and argon [50], respectively. Hence, at a pressure of 200KPa, $k_{N_4^+;N_2} N_{ep} \sim 3.2 \times 10^6$ s^{-1} and $k_{Ar_2^+;Ar} N_{ep} \sim 1.25 \times 10^6$ s^{-1}. Therefore, the correction factor for τ^{-1}, due to the electron-ion recombination process, is less than 11% in N_2 and less than 5% in Ar (the HCl mole fraction was $\sim$1%).

The last item considered in this section is that expressed by Eq. (3.1-38). If we approximate the radial

dependance of the electron number-density by the Gaussian curve of Eq. (3.1-14) (with $r_{1/e}^2 = 4Dt$), then Eq. (3.1-38a) can be written as

$$\left| \frac{2D}{r_{1/e}^2} \left(1 - \frac{r^2}{r_{1/e}^2}\right) \right| << k_{HCl;Cl} N_{HCl}, \qquad (4.1\text{-}1a)$$

where the longitudinal term $\frac{\partial^2 N_e}{\partial z^2}$ has been neglected. For $D = 6 \times 10^3 cm^3 s^{-1}$, $r = 0$ and $r_{1/e} \sim 0.4$ cm Eq. (4.1-1) reduces to

$$7.5 \times 10^4 s^{-1} << 2 \times 10^6 s^{-1} \quad . \qquad (4.1\text{-}1b)$$

The left hand term of Eq. (3.1-38b) can be estimated from the $P_s(0,z)$ curve shown in fig. 3-1. The condition reduces to (with $v_d \sim 10^6 cm \cdot s^{-1}$)

$$(3\text{-}4) \times 10^6 s^{-1} << 2 \times 10^7 s^{-1} \qquad (4.1\text{-}2)$$

Therefore, the approximation which neglects the spatially dependant term in the rate equation for electrons is not very good. However, as we shall see, this does not present any serious problems.

Let us write the rate equation for the electrons as

$$\frac{\partial N_e}{\partial t} = -v_d \frac{\partial N_e}{\partial z} - k_{HCl;Cl} N_{HCl} N_e, \text{ or} \qquad (4.1\text{-}3a)$$

$$\frac{DN_e}{Dt} = -k_{HCl;Cl}N_{HCl}N_e \qquad (4.1\text{-}3b)$$

where recombination processes have been neglected and where $\frac{D}{DT}$ represents the derivative evaluated in a frame of reference moving with the electrons, i.e., along the characteristic curve $z-v_dt = z_o$. Equation (4.1-3b) may now be integrated to give

$$N_e(z_o+vt,t) = N_e(z_o)\exp -t/(k_{HCl;Cl}N_{HCl}) \; . \qquad (4.1\text{-}4)$$

Therefore, if the cathode-fall region is effective in producing electrons,then the discharge current pulse will decay exponentially with the characteristic time τ. Note that the homogeneous rate equation model is applicable if the plasma is created in the way described in Section 3.1.5.

4.2.1 Experimental

A typical current pulse is shown in Fig. 4-1. The current decays exponentially over more than an order of magnitude ($\sim 2.3\tau$). This shows that the electron-ion recombination process is small compared to the attachment rate under these conditions (as expected). At later times the current pulse is distorted, in part, by noise. More significantly, the current is carried by positive and negative ions (this region is not shown in Fig. 4-1), which

Fig. 4-1 Discharge current pulse observed in $Ar-N_2-HCl$ (35:64:1). The total pressure is $\approx$ 77 KPa, and the reduced field (E/N) is $\sim 10^{-20} V \cdot m^2$.

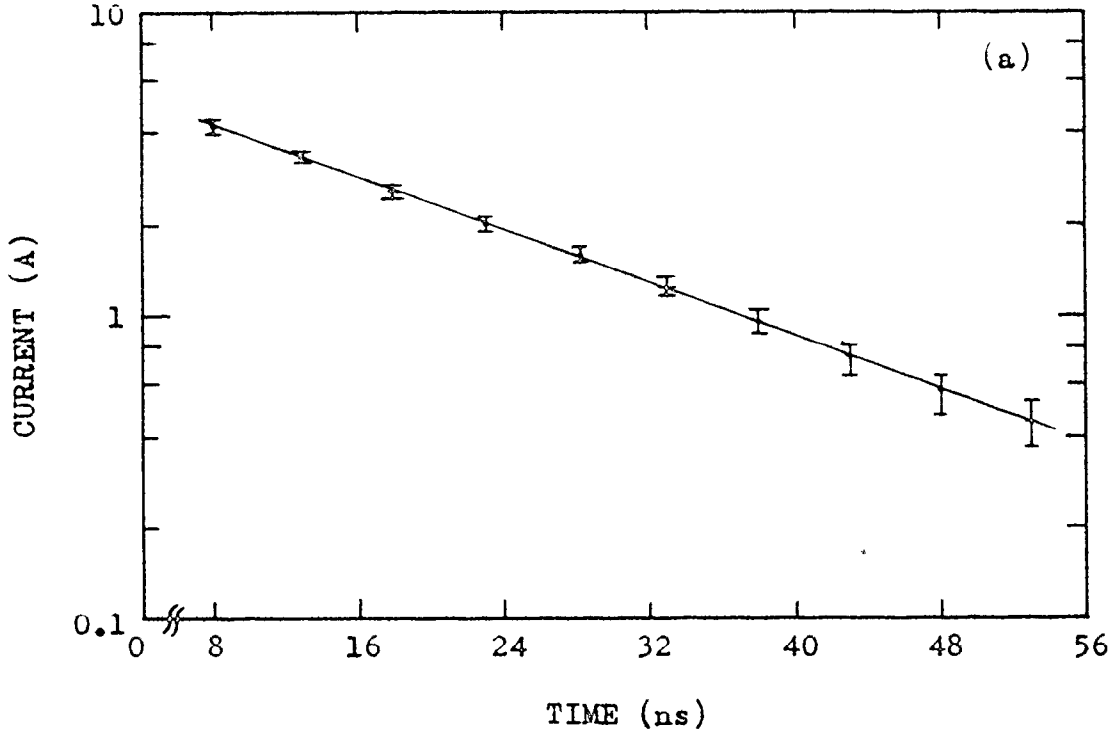
10
1
0.1
CURRENT (A)
(a)
0
8
16
24
32
40
48
56
TIME (ns)

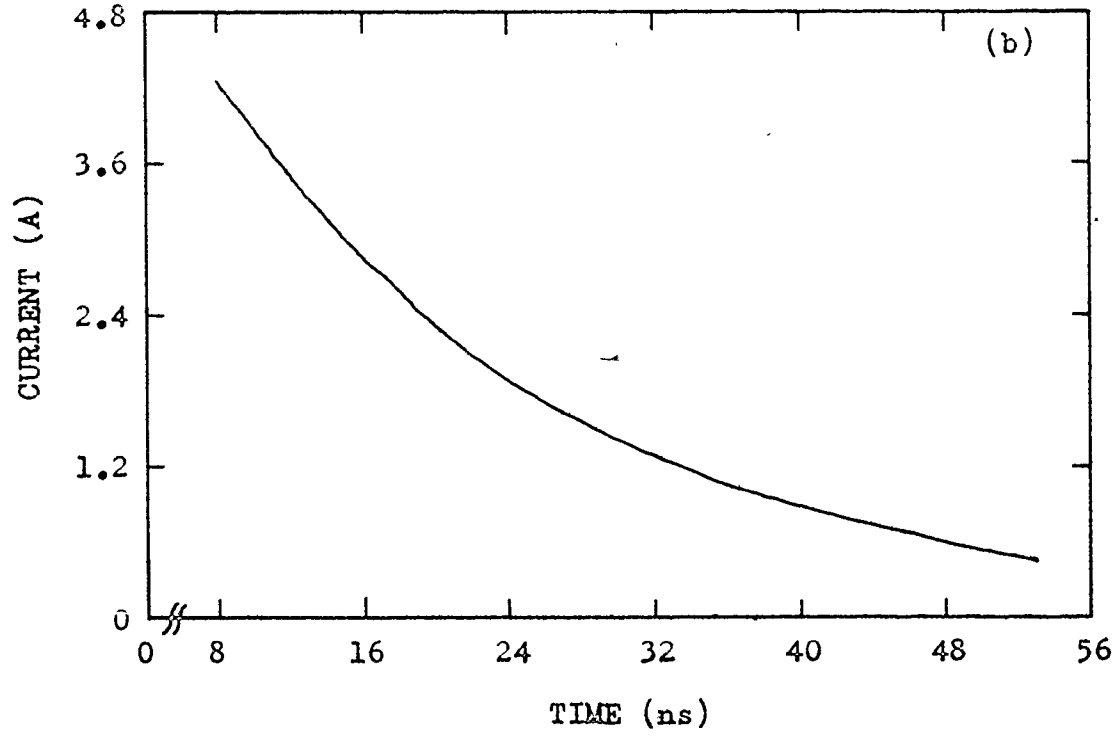
4.8
3.6
2.4
1.2
0
CURRENT (A)
(b)
0
8
16
24
32
40
48
56
TIME (ns)

causes a departure from exponential decay.

The dissociative attachment rate (τ^{-1}) is found to be a linear function of the total pressure (for a constant HCL mole fraction), as shown in Fig. 4-2. The rate coefficient $k_{HCl;Cl^-}$ is given by the simple expression $k_{HCl;Cl^-}$ = slope/[HCl mole fraction], where the slope is that of τ^{-1} versus the total pressure.

The measured dissociative attachment rate coefficient, as a function of E/N, is plotted in Figs. 4-3 and 4-4 for Ar-HCl and Ar-N_2-HCl gas mixtures, respectively. The rate coefficients calculated using the Boltzmann code (Section 3.1.2), and the dissociative attachment cross-sections. Abouaf et al [76], normalized to those of Azria et al [74], are also shown in the two figures. Additional measurements of the rate coefficient were performed at an HCl mole fraction of 0.4% and 2.8% in Ar-HCl mixtures and at a 0.4% mole fraction in an Ar-N_2-HCl mixture. For Ar-HCl, these measurements were done at large enough E/N ($>0.5\times10^{-20}$ V·m^2) that the average electron energy ($\bar{\varepsilon}$) does not depend significantly upon the HCl mole fraction. No systematic variations in $k_{HCl;Cl^-}$ were observed when the HCl mole fraction was changed.

Figure 4-5 shows the measured rate coefficient $k_{HCl;Cl^-}$ plotted as a function of the average electron energy $\bar{\varepsilon}$ (where $\bar{\varepsilon}$ is calculated from the Boltzmann code). The

Fig. 4-2 Dissociative attachment rate as a function of the total pressure. a) The mixtures are Ar-N_2-HCl (35:64:1), and the reduced field is 10^{-20} V·m^2. b) The mixtures are Ar-HCl (99:1) and the reduced field is 1.2 x 10^{-20} V·m^2.

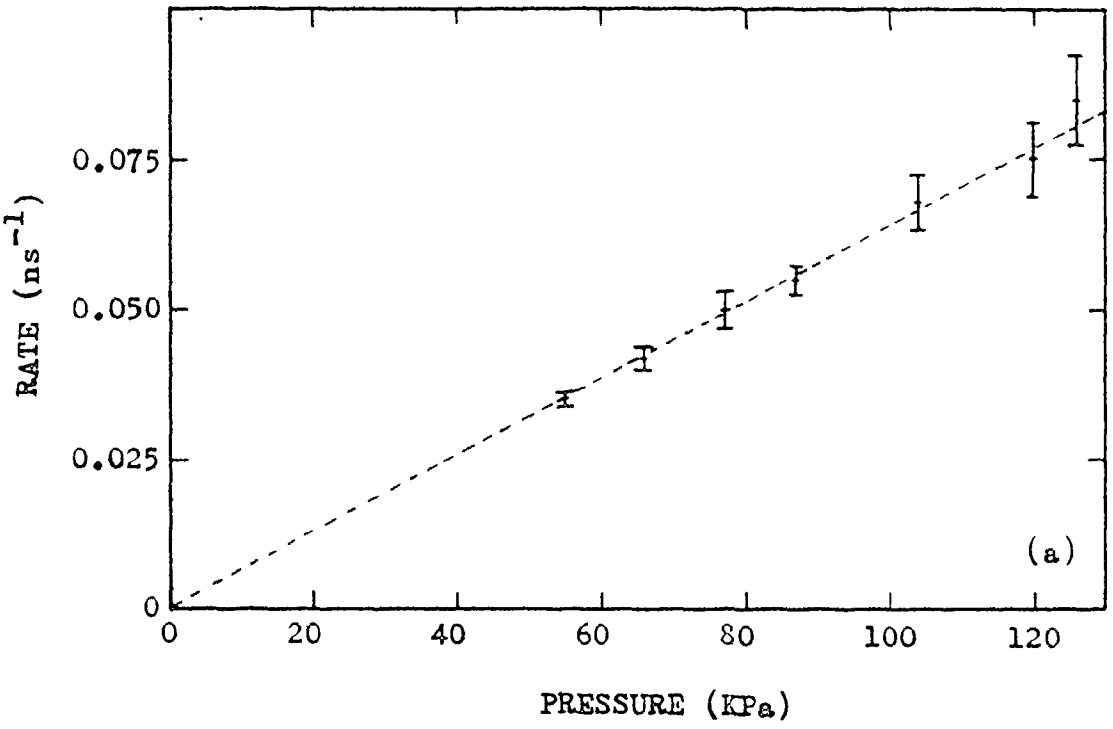
0.075
0.050
0.025
0
RATE (ns^{-1})
0
20
40
60
80
100
120
PRESSURE (KPa)
(a)

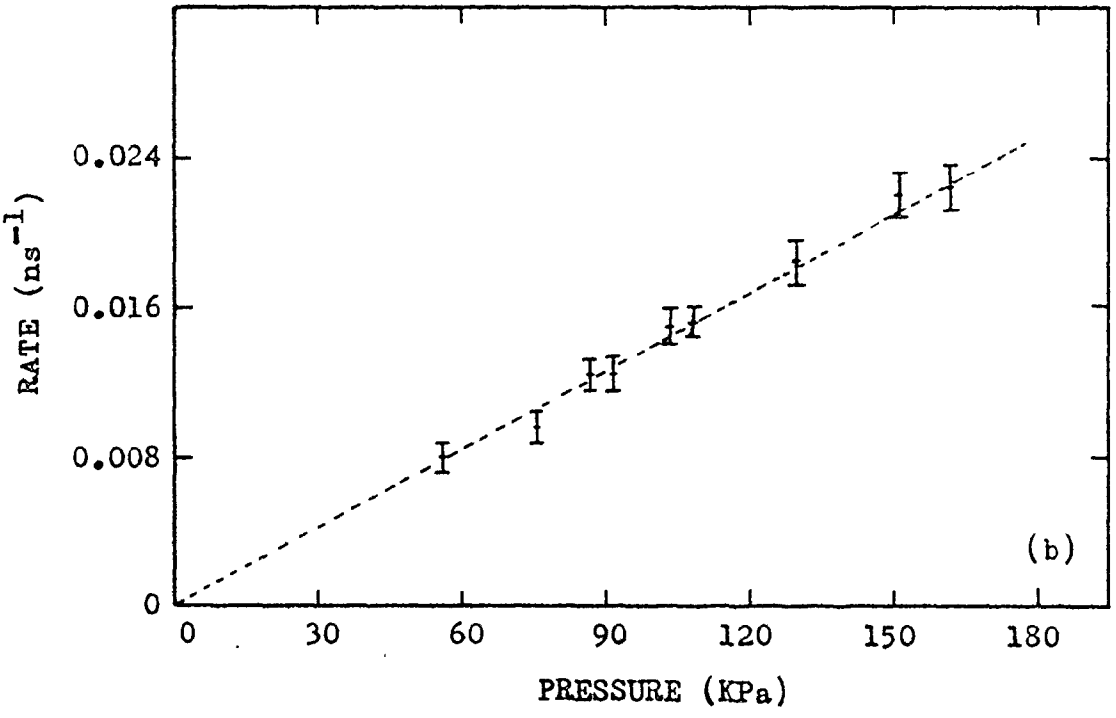
0.024
0.016
0.008
0
RATE (ns^{-1})
0
30
60
90
120
150
180
PRESSURE (KPa)
(b)

Fig. 4-3 Dissociative attachment rate coefficient measured in Ar-HCl mixtures. The mixtures were (99:1) (I), (97.2:2.8) (▲), (99.6:0.4) (•). The rate coefficients calculated by our Boltzmann code are shown for the cases where the electron energy distributions are those for electrons in pure Ar and in Ar-HCl (99:1) mixtures, and the cross-section used is that of Abouaf et al [76] normalized to the peak value of Azria et al [74].

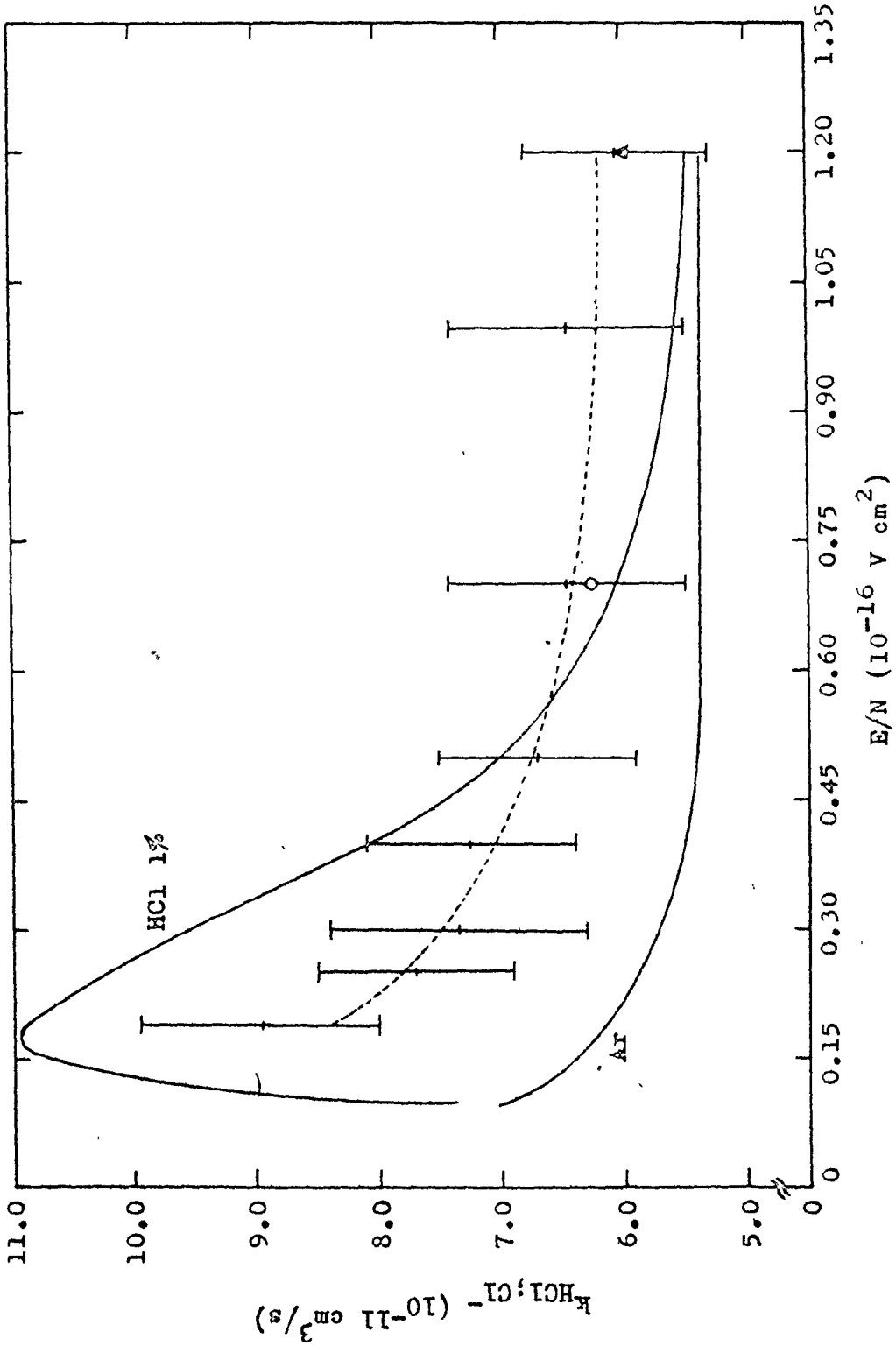
HCl 1%
Ar
$k_{HCl;Cl^-}$ (10^{-11} cm^3/s)
E/N (10^{-16} V cm^2)
11.0
10.0
9.0
8.0
7.0
6.0
5.0
0
0.15
0.30
0.45
0.60
0.75
0.90
1.05
1.20
1.35

Fig. 4-4 Dissociative attachment rate coefficient measured in Ar-N_2-HCl mixtures. The mixtures are (35:64:1) (I) and (85:6:14:0.4) (▲). The results of Christophorou et al [62] (o) (N_2-HCl mixtures) are shown. The rate coefficients calculated by our Boltzmann code are shown for an Ar-N_2-HCl (35:64:1) mixture. The peak values for the dissociative attachment cross section used are those of Azria et al [74] (σ=8.9 x $10^{-19}cm^2$) (•) and the best fit value (σ=18 x $10^{-19}cm^2$) (◘).

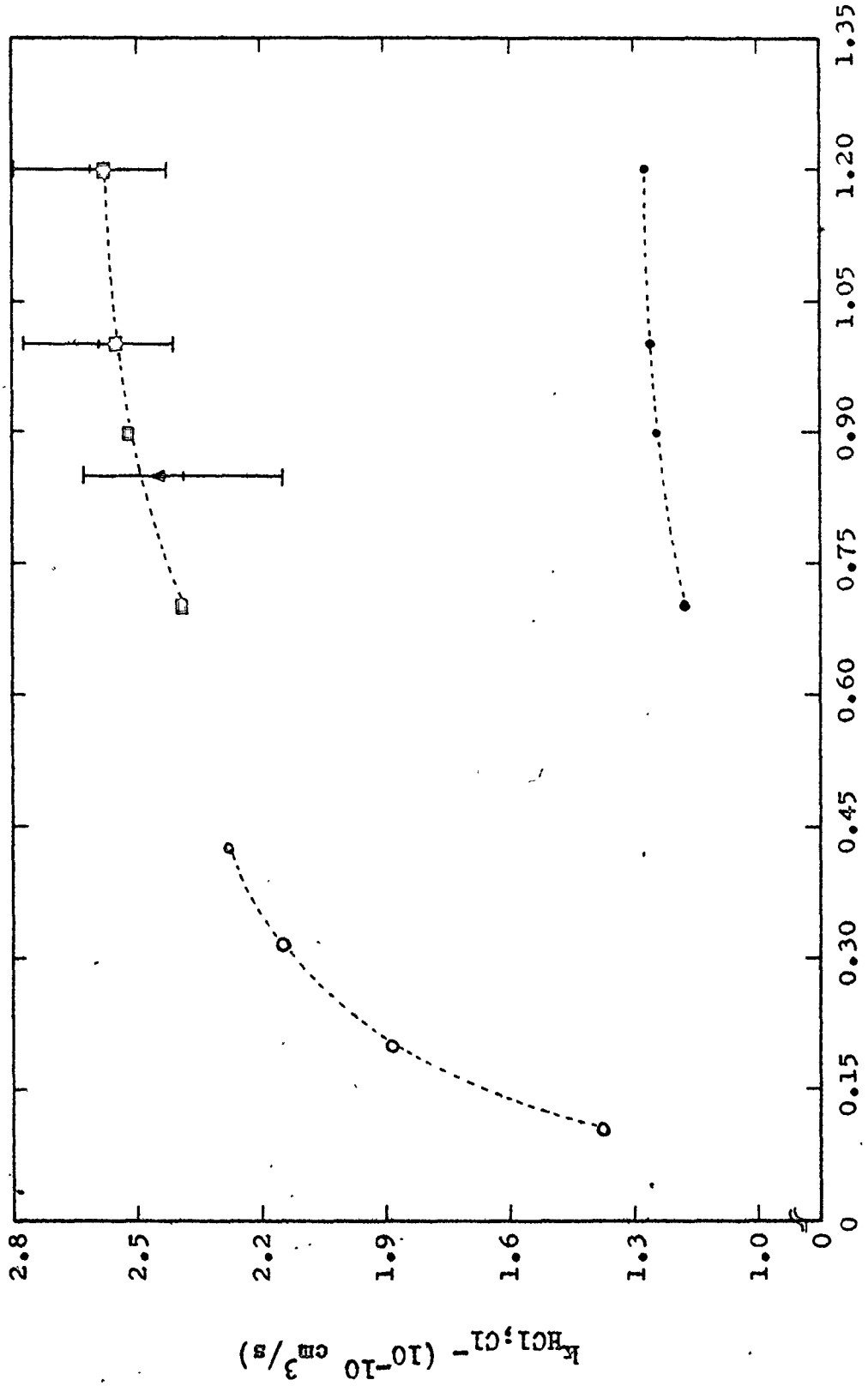
$k_{HCl;Cl^-}$ (10^{-10} cm^3/s)
2.8
2.5
2.2
1.9
1.6
1.3
1.0
0
0.15
0.30
0.45
0.60
0.75
0.90
1.05
1.20
1.35
E/N (10^{-16} V cm^2)

Fig. 4-5 Summary of the dissociative attachment rate for HCl as a function of the electron average energy, showing results from the present experiment (▲ (Ar-HCl), ◘ (Ar-N_2-HCl)) and from the experiment of Christophorou et al [62] (o). The calculated rate coefficient for Ar-N_2-HCl (35:64:1) (σ_{peak} ~ 18 x 10^{-19} cm^2) (——) and Ar-HCl (99:1) (σ_{peak} ~ 9.4 x 10^{-19} cm^2) (----) are also shown.

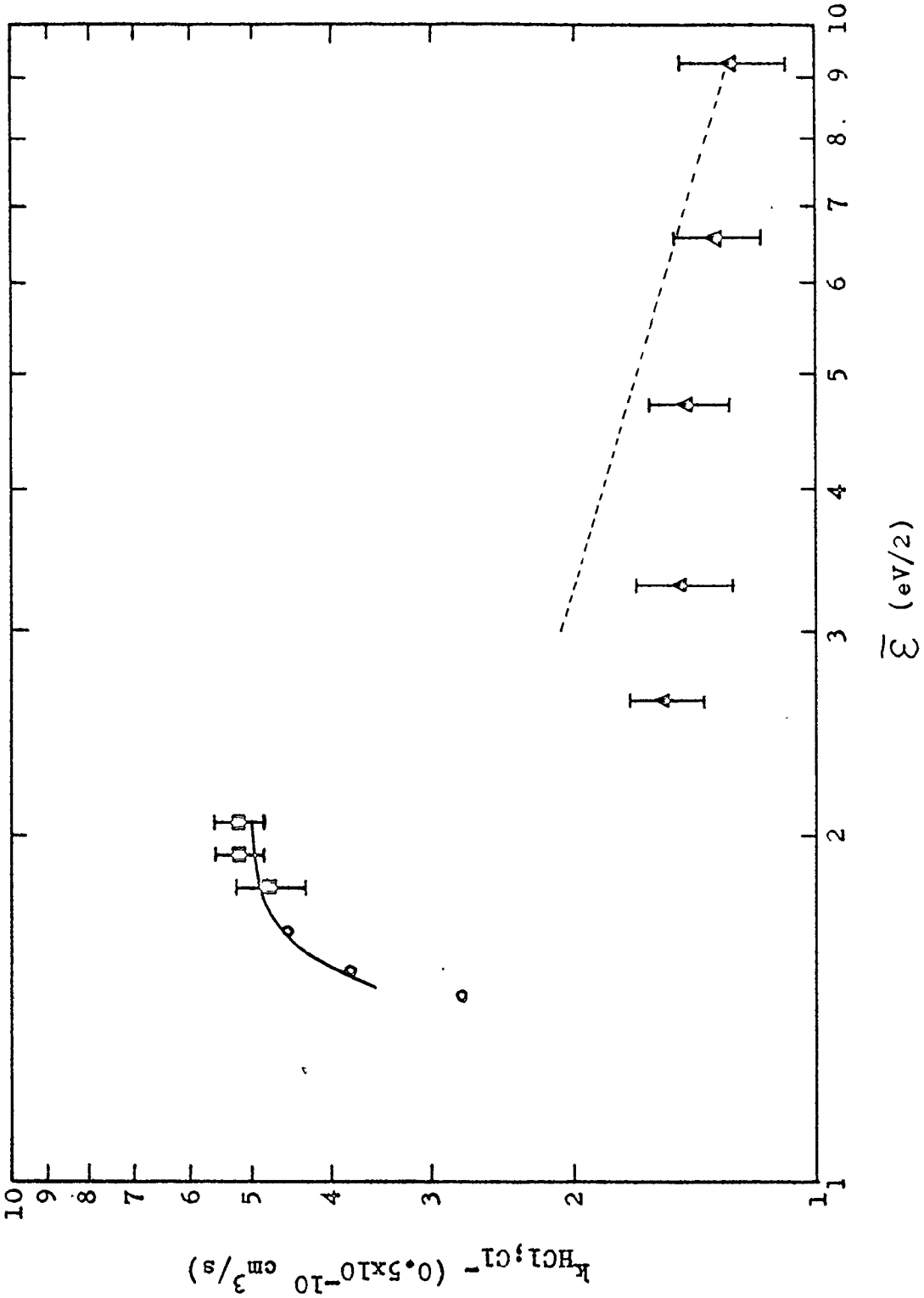
$k_{HCl;Cl^-}$ (0.5×10^{-10} cm^3/s)
$\bar{\varepsilon}$ (eV/2)
1
2
3
4
5
6
7
8
9
10

calculated rate coefficient (best-fit cross-section peak value) agrees with the measured value in the case of the Ar-N_2-HCl gas mixtures. The experimental values obtained in the latter case compare very well to those measured by Christophorou et al [62] in N_2-HCl mixtures. However the agreement between the calculated and measured rate coefficient at low energy is not very good when the gas mixture is Ar-HCl.

4.2.2 Discussion and Conclusion

The differences observed between the dissociative attachment rate coefficients measured in Ar-N_2-HCl and those obtained in Ar-HCl puts some doubt on the accuracy of the method used. Part of the problem comes from the fact that swarm experiments generally do not permit identification of the particular processes involved. For example in the present case the various types of ions formed are not distinguishable.

Although several attempts have been made to remove the discrepancy, none has been fruitful. However, it is useful to discuss in detail some of the hypothesis relating to the causes of the discrepancies. We first consider various processes that might make the rate coefficient appears larger in Ar-N_2-HCl than in Ar-HCl.

The electron-ion recombination rate in N_2 is approximately three times that in pure Ar. This cannot explain the

discrepancy because recombination barely increases the apparent rate coefficient (as pointed out in Section 4.1.3). The latter is further confirmed by the fact that the current pulse decays exponentially over more than one order of magnitude, as illustrated in Fig. 4-1, and also by the fact that the rate coefficients measured in Ar-N_2-HCl, with HCl mole fractions of 0.4% and 1.0%, remained constant (within experimental error).

The small amount of impurities which amy have been present in the gases cannot account for the observed discrepancy. For example, an O_2 mole fraction of 10-20% would have been required to double the apparent rate coefficient (for HCL~1%). The effect would have been even less with CO as an impurity. Furthermore, the rate coefficient measured with ~0.4% HCl should have been, in that case, approximately 1.5 times that obtained with ~1.0% HCl (assuming that the rate coefficient measured in Ar-HCL was exact).

Another explanation is the possibility of forming a stable HCl negative ion through a three-body process of the type

$$e + HCl + A \rightarrow HCl^- + A(\text{kinetic energy}), \qquad (4.2\text{-}1)$$

where the third body A is Ar, N_2 or HCl. The rate-coefficient for this process clearly depends on the type of buffer gas used. Even though this hypothesis looks appealing, it does

not resolve the discrepancy because, for a given HCl mole fraction, the rate (τ^{-1}) should increase as P^2 (P is the total pressure). However, it has been found to vary linearly with P over a wide range of pressure (Fig. 4-2).

The differences may come from a failure of the calculated electron-energy distribution to represent accurately the real situation. The conditions of applicability of the Boltzmann code have been extensively discussed in Section 3.1.2. In order for the low rate-coefficient measured in Ar-HCl to match the value obtained in Ar-N_2-HCl, the actual average-electron energy would have to be > 10 eV, which is a value significantly larger than ~5eV estimated for the Boltzmann code (very unlikely to occur).

The difference cannot be explained by assuming that the actual relaxation time (τ_{Ra}) for the electron-energy distribution is larger than that estimated in Section 3.1.2 (τ_R ~ 5ns). If this was the reason, then τ_{Ra} would have to be large enough to prevent significant variation (< 1ev) of the average electron-energy ($\bar{\varepsilon}$) over time scales > 100ns so that the current pulse could decay exponentially over more than one order of magnitude, as experimentally observed. The actual value for the relaxation time would therefore have to be >> 100 ns.

Furthermore, the discrepancies cannot be explained by the fact that the cross-sections for the high-energy processes in HCl have been neglected in the calculations.

Their effect would have been to make the computed average electron-energy even smaller.

In summary, we are not able to explain adequately the differences in the rate coefficients measured in different mixtures. However it should be mentioned that the same type of phenomenon (different rate coefficients in Ar-X and N_2-X) has been reported by other workers, e.g. in the measurement of dissociative-attachment to Cl_2 [66, 78], and to HCl and DCl [62, 77]. Reasons for the differences have not been given. We believe that the results could be explained if the plasma was analysed with, e.g., a mass spectrometer, in order to determine which ions are formed during the current pulse. However this would require an extensive research effort.

CHAPTER 5

CONCLUSION

A simple, pulsed, electron-beam gun has been built based on the original work of Brau et al [1]. The vacuum diode of the electron-beam gun is operated on the second voltage peak produced by the spiral generator, initially charged at ~10 KV. We have been able to obtain an ~175 A/cm^2 (at the anode) electron-beam of ~90 KeV energy electrons, with a pulse duration ~12 ns FWHM. These characteristics are similar to those of Brau et al [1], except that in our case they were obtained by initially charging the generator to 10 KV, rather than 12 KV. Therefore, the possibility of generator insulation breakdown (estimated at ~15 KV) was considerably reduced. It was observed that the emerging electron-beam was quite uniform over the whole surface of the 6 mm diameter output window. Moreover, scattering in the foil was found to produce a diffusive increase in the electron-beam angular spread, leading to a nearly Gaussian distribution of velocity with a 1/e width ~0.45π.

The electron-beam was used to ionize gas mixtures of Ar-HCl and Ar-N_2-HCl with typical HCl mole fractions ~1%. An electric field of 1500-5000 $V \cdot cm^{-1}$ was then applied across the plasma by means of two uniform field electrodes.

After the electron-beam cutoff, the conductivity of the high-pressure glow discharge decayed quasi-exponentially with a typical characteristic time ~50 ns. An extensive study of the electrical properties of the discharge circuit has shown that, under normal operation conditions, the bias circuit provided a constant gap voltage (within 0.2%) during the decaying portion of the current pulse.

The plasma-electron energy distribution was determined by a Boltzmann code. The distribution function was used to calculate the average electron energy ($\bar{\varepsilon}$), the rate coefficient for the dissociative-attachment of electrons to HCl ($k_{HCl;Cl^-}$), and other parameters such as the drift velocity (v_d) and the characteristic energy (ε_k). The code was found to be applicable to the present problem when $E/N > 0.4 \times 10^{-20}$ V·m^2.

A simple model describing the temporal evolution of the discharge current pulse has been developed. For the case of a dissociative-attachment dominated plasma, the model predicts an exponentially decaying current pulse having a characteristic time $\tau = (k_{DA}N_{DA})^{-1}$ (k_{DA} is the dissociative attachment rate coefficient and N_{DA} is the corresponding specie number density).

Suggestions are presented for a proposed simple modification to the electron-beam gun. The modification consists of replacing the stainless-steel-mesh anode with a thin aluminum foil (~18 μm) and the aluminum foil window with a low mass density film such as mylar. It is shown that a quasi-

homogeneous plasma can, in principle, be generated, and consequently the system could be used to measure electron-ion recombination rates.

We have used the system to measure the rate coefficient of the dissociative-attachment of electrons to HCl. The cross-section obtained by Abouaf et al [76] was normalized to $\tau = 18 \times 10^{-19} cm^2$ using the data obtained from our Ar-N_2-HCl experiments. This value agrees reasonably well with that determined by Christophorou et al [62] in N_2-HCl mixtures ($\sigma \sim 19.8 \times 10^{-19} cm^2$). However, the rate coefficient measured in Ar-HCl mixtures leads to a normalized cross-section peak value $\sigma \sim 9.4 \times 10^{-19} cm^2$, which does not agree with Christophorou et al [62] but which is in good agreement with the value determined by Azria et al [74] $\sigma = 8.9 \times 10^{-19}\ cm^2$. We have tried to explain the difference by considering first the possibility that some unknown ions might be created during the discharge, and then by looking at the possibility that the electron-energy distribution determined by our Boltzmann code was not applicable to this problem. Both hypothesis have failed to explain the discrepancy.

The individual experiments performed in Ar-HCl and Ar-N_2-HCl suggests that the rate coefficients measured are those for the dissociative-attachment of electron to HCl. However, the discrepancy between the results introduces questions concerning the validity of these results. We

believe that these questions can be answered only by extensive analysis of the time-dependant reaction in the plasma. This will require considerable additional research effort.

APPENDIX 1

NITROGEN, ARGON and HCl CROSS-SECTIONS

Figure A-1 shows the momentum transfer cross-section for N_2 and Ar as a function of the electron energy. The data of Engelhardet et al [80] were used for N_2. For Ar, we have used the data cited by Itikawa [83] (< 10 eV) and those calculated from the experimental differential elastic cross-sections of Williams et al [86] and Dubois et al [87] (extrapolated values were obtained at small and large angles using the method described by de Heer et al [84]).

The inelastic collision cross-section cited by Erggarter [81] has been used for Ar. Those of Englander-Golden [85] were used for N_2. For HCl, the vibrational excitation cross-sections $(0 \rightarrow 1)$ and $(0 \rightarrow 2)$ measured by Rohr and Linder [82] were used.

Fig. A-1 Momentum-transfer cross section for N_2 and Ar.

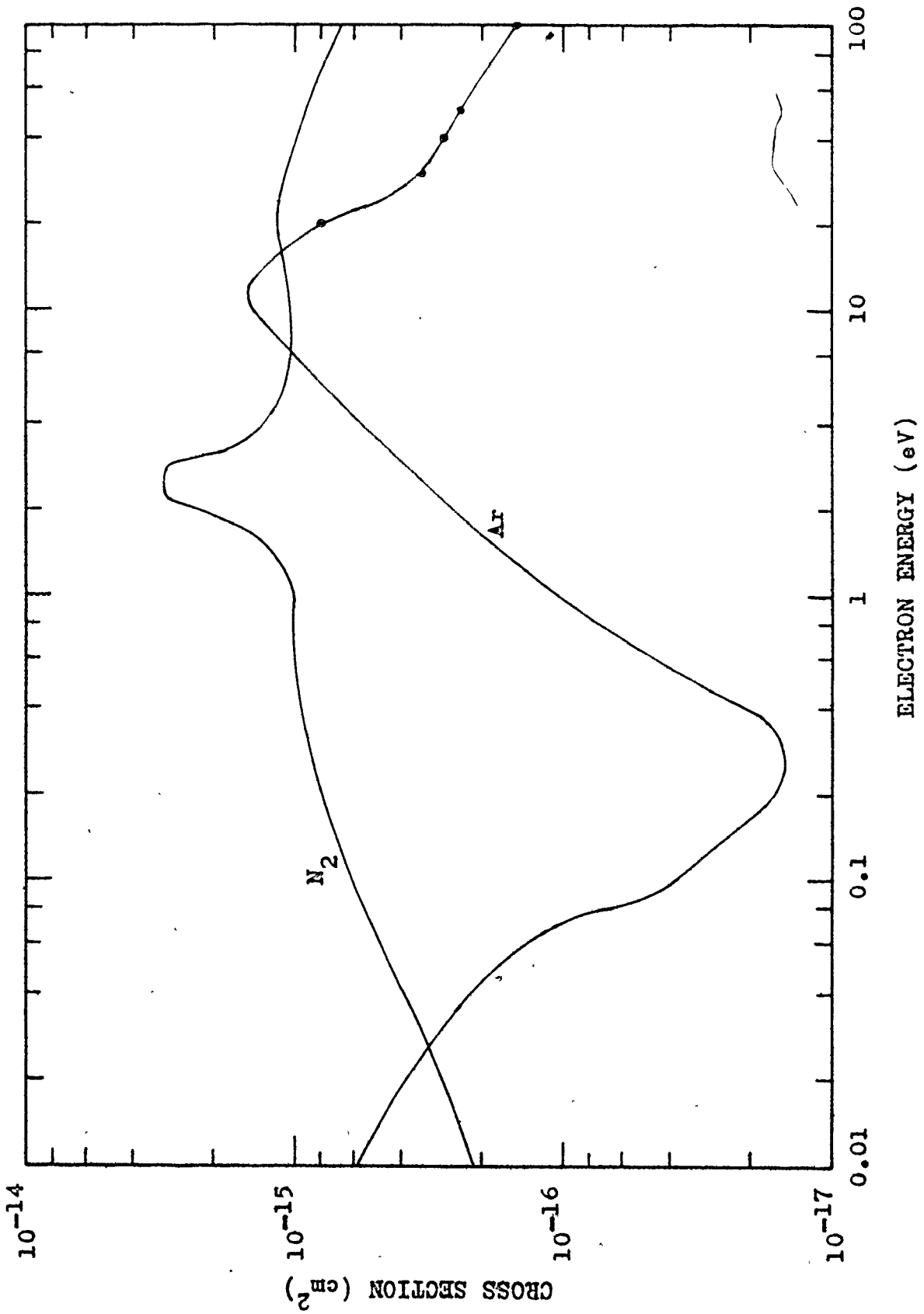
CROSS SECTION (cm^2)
10^{-14}
10^{-15}
10^{-16}
10^{-17}
0.01
0.1
1
10
100
ELECTRON ENERGY (eV)
N_2
Ar

REFERENCES

1- C.A. Brau, J.L. Raybun, J.B. Dodge, F.M. Gilman, Rev. Sci. Instrum., 48, No. 9, 1154-60 (1977)

2- R.A. Fitch, V.T.S. Howell, Proc. IEE, 111, No. 4, 849-55 (1964)

3- R.H. Fowler, Nordheim, Proc. Roy. Soc. A119, 173 (1928)

4- H.E. Tomashke, D. Alpert, J. Vac. Sci. Technol, 4, 192 (1967)

5- G.N. Fursei, Vorontsov-Vel'yaminov, Sov. Phys.-Tech. Phys., 12, 1370-77 (1968)

6- Parker, Duncan, Anderson, J. Appl. Phys., 45, 2463 (1974)

7- S.P. Bugaev, G.A. Mesyats, D.I. Proskvrovskii, Sov. Phys.-Doklady, 14, No. 6, 605 (1969)

8- J.G. Kelly, S.A. Goldstein, D.W. Swain, J. Appl. Phys., 46, 4726 (1965)

9- B.B. Dayton, Proc. 6th A.V.S. Natl. Symp., p 101, Pergamon Press, Oxford (1959).

10- Y. Ohki, K. Yahagi, J. Appl. Phys, 46, No. 8, 3695 (1975)

11- K.D. Bergeron, J. Appl. Phys, 48, No. 7, 3073 (1977)

12- A.S. Pokorovskaia-Soboleva, B.N. Klarfel'd, Sov. Phys. JETP, 5, No. 5, 812 (1957)

13- V. Nassisi, A. Luches, Rev. Sci. Instrum., 50, No. 7, 900 (1979)

14- A.G. Klein, Am. J. Phys., 43, No. 4, 368 (1975)

15- J.N. Turner, G.G. Hausner Jr., D.F. Parsons, J. Phys. E, 8, 954 (1975)

16- B.N.C. Agu, T. Burdett, E. Matsukawa, Proc. Phys. Soc., 71, 201-6 (1958)

17- C.D. Child, Phys. Rev., 32, 492 (1911)

18- J.H. Jacob, Phys. Rev. A, 8, 226 (1972)

19- J.H. Jacob, J. Appl. Phys., 45, No. 1, 467 (1974).

20- S. Goudsmit, J.L. Saunderson, Phys. Rev., 57, 24 (1940)

21- G. Molière, Z. Naturforsh, 3a, 78 (1948)

22- H.A. Bethe, Phys. Rev., 89, 1256 (1953)

23- Wang Ming. Chen., E. Guth, Phys. Rev., 84, 1092 (1951)

24- E. Breitenberger, Proc. R. Soc. Lond., 250, 514 (1959)

25- B.P. Nigam, M.K. Sundarsen, Ta-You Wu, Phys. Rev., 115, 491 (1959)

26- Hanson, Lanzl, Lyman, Scott, Phys. Rev., 84, 634 (1951).

27- L.V. Spencer, Phys. Rev., 78, 526 (1955)

28- B.J. Schneider, C.A. Brau, Appl. Phys. Lett., 33, 569 (1978)

29- J.R. Bailey (in Handbook of Vacuum Physics) edited by A.H. Beck, The MacMillan Company, New York 1964, p. 229.

30- T.Y. Chang, Rev. Sci. Inst., 44, No. 4, 405 (1973)

31- M.J. Berger, S.M. Seltzer, Tables of Energy-losses and Ranges of Electrons and Positrons, NAS-NRC publication 1133, p. 205.

32- L. Landau, E. Lifchitz, Mecanique des Fluides, Editions Mir Moscou 1971, p. 242

33- M.H. Hughes, J. Phys. B., 3, 1544 (1970)

34- K. Kitamori, H. Tagashira, Y. Sakai, J. Phys. D., 11, 283-92 (1978)

35- T. Holstein, Phys. Rev., 70, 367 (1946)

36- B. Sherman, J. Math. Analy. Appl., 1, 342 (1960)

37- A.J. Postma, Physica, 43, 581 (1969)

38- S.D. Rockwood, Phys. Rev., A8, 2348 (1973)

39- M. Mitchner, Charles H. Kruger Jr., Partially Ionized Gases, John Wiley and Sons Inc. (1973)

40- K. Smith, R.M. Thomson, Computer Modeling of Gas Lasers Plenum Press, New York (1978)

41- A.E.S. Green, T. Sawada, J. Atmos. Terr. Phys., 34, 1719 (1972)

42- P.F. Kneustubb In Advances in Mass Spectrometry, ed. by Kendrich, 4 (Elsevier Publishing, New York 1968) p. 391.

43- D. Smith, P.R. Cromey, J. Phys. B1, 638 (1968)

44- C.B. Krisschmer, H.L. Peterson, J. Appl. Phys., 34, 3209 (1963)

45- P. Keberle et al, J. Chem. Phys., 47, 1684 (1966)

46- A.K. Bhattacharga, J. Appl. Phys., 41, 1707 (1970)

47- W.C.F. Liu, D.C. Conway, J. Chem. Phys., 60, 784 (1974)

48- W.C.F. Liu, D.C. Conway, J. Chem. Phys., 62, 3070 (1975)

49- J.C. Cronin, M.C. Sexton, J. Phys. D, 1, 889 (1968)

50- J.N. Bardsley, M.A. Biondi, Adv. at Mol. Phys., 6 2 (1970)

51- E.W. McDaniel, V. Cermak, A. Dalgarno, E.C. Ferguson, L. Friedman, Ion-Molecule Reactions, John Wiley, New York (1970)

52- F.E. Niles, J. Chem. Phys., 58, 4820 (1973)

53- D.H. Douglas-Hamilton, J. Chem. Phys., 58, 4820 (1973)

54- Smith A.L.S. et al., sealed CO_2 Lasers, School of Physical Sciences, University of St. Andrews, CVD Research Project R/ 16/3, Annual Report 1975.

55- W.J. Wiegand, W.L. Nigham, Phys. Rev., A10, 922 (1974)

56- A.J. Davies, C.J. Evans, P.M. Woodison, Comp. Phys. Comm., 14, 287 (1978)

57- A.J. Davies, C.J. Evans, F. Llewellyn Jones, Proc. R. Soc., A281, 164 (1965)

58- P.M. Davidson, Brit. J. Appl. Phys., 4, 170 (1953)

59- W.P. Allis, G. Fournier, D. Pigache, J. Phys. (Paris), 38, 915 (1977)

60- Tran Nogc An, E. Marode, P.C. Johnson, J. Phys. D., 10, 2317 (1977)

61- J.D. Cobine, Gaseous Conductors, McGraw-Hill Inc. (1941)

62- L.G. Christophorou, R.N. Compton, H.W. Dickson, J. Chem. Phys., 48, 1949 (1968).

63- T.E. Bortner, G.S. Hurst, Healt Phys., 1, 39 (1958)

64- K.J. Nygaard, R.S. Hunter, J. Fletcher, R.F. Stephen, Appl. Phys. Lett., 32, 351 (1978).

65- Hao-Lin Chen, R.E. Center, D.W. Trainor, W.I. Fyfe, J. Appl. Phys., 48, 2297 (1977)

66- M. Rockni, J.H. Jacob, J.A. Mangano, Appl. Phys. Lett., 34, 187 (1979)

67- M.A. Barton, Phys. Rev., 30, 614 (1927)

68- A.D. Nier, E.E. Hanson, Phys. Rev., 50, 722 (1936)

69- R.M. Reese, V.H. Dibeler, F.L. Mohler, J. Res. Nat. Bur. Stand., 57, 367 (1956)

70- H. Von Gutbier, H. Neurt, Z. Naturforsh, 9a, 335 (1954)

71- R.E. Fox, J. Chem. Phys., 26, 1281 (1957)

72- D.C. Frost, C.A. McDowell, J. Chem. Phys., 29, 503 (1958)

73- M. Allan, S.F. Wong, Thirty-Second Annual Gaseous Electronics Conference, (1979)

74- R. Azria, Roussier L., R. Paineau, M. Tronc, Rev. Phys. Appl., 9, 469 (1974)

75- I.S. Buchel'Nivoka, Sov. Phys. JETP, 35, 783 (1959)

76- R. Abouaf, D. Teillet-Billy, J. Phys. B., 10, 2261 (1977)

77- H.W. Dickson, L.G. Christophorou, R.N. Compton, ORNL-T.M. report 1724

78- R.C. Sze, A.E. Greene, C.A. Brau, Thirty-Second Annual Gaseous Electronics Conference (1979)

79- A.G. Engelhardt, A.V. Phelps, Phys. Rev., 133, A377 (1964)

80- A.G. Engelhardt, A.V. Phelps, C.G. Risk, Phys. Rev., 135, A1569 (1964)

81- E. Eggarter, J. Chem. Phys., 62, 837 (1975)

82- K. Rohr, F. Linder, J. Phys. B, 9, 2521 (1976)

83- Yukikazu Itikawa, Atomic Data & Nucl. Data tables, 14, 1 (1975)

84- F.J. de Heer, R.H.J. Jansen, W. van der Kaay, J. Phys. B, 12, 979 (1979)

85- D. Rapp, P. Englander-Golden, J. Chem. Phys., 43, 1464 (1965)

86- J.F. Williams, B.A. Willis, J. Phys. B, 8, 1670 (1975)

87- R.D. Dubois, M.E. Rudd, J. Phys. B, 9, 2657 (1976)